UNIVERSITY OF OKLAHOMA

GRADUATE COLLEGE

QUANTIFYING AND MITIGATING DEBRIS-INDUCED BIAS IN RADAR MEASUREMENTS OF TORNADIC WINDS

A THESIS

SUBMITTED TO THE GRADUATE FACULTY

in partial fulfillment of the requirements for the

Degree of

MASTER OF SCIENCE IN METEOROLOGY

By

MORGAN ELIZABETH SCHNEIDER
Norman, Oklahoma
2021

QUANTIFYING AND MITIGATING DEBRIS-INDUCED BIAS IN RADAR MEASUREMENTS OF TORNADIC WINDS

A THESIS APPROVED FOR THE
SCHOOL OF METEOROLOGY

BY THE COMMITTEE CONSISTING OF

Dr. Robert D. Palmer (Chair)

Dr. David J. Bodine

Dr. Howard B. Bluestein

Acknowledgments

I would like to thank my advisors, Dr. David Bodine and Dr. Robert Palmer, for all of the guidance and support they have provided me over the past two years. You have both taught me so much about radar and research in general, and this knowledge will serve me well during my Ph.D. and the rest of my career. Perhaps most importantly, you saw my potential and trusted me—probably more than I trusted myself—to take on a complex, technical project because you believed I would succeed. The amount of confidence I have gained in my own capability and value as a scientist over the course of two years is immeasurable. I sincerely look forward to working and collaborating with you throughout my career.

I would also like to thank my Master's committee member, Dr. Howard Bluestein, for taking the time to serve on my committee and for offering me the unique, exciting opportunity to take part in storm season field deployments with RaXPol, despite the challenges beyond our control that we've had to adapt to. Field work is by far one of my favorite aspects of meteorology research, and I am thankful to have been able to participate and learn the ropes as a member of the RaXPol crew. Through this opportunity, I have learned valuable lessons about mobile radar operation and data collection.

I am grateful to the rest of the NSF Debris research group, Dr. Sebastián Torres, Dr. Boon Leng Cheong, Dr. Caleb Fulton, and Dr. Casey Griffin, for all of their help, suggestions, and feedback at our research group meetings throughout the last two years. I would especially like to thank Dr. Torres for helping me understand and implement the spectral signal processing techniques that are fundamental to a very large part of this work. Without your incredibly helpful explanations and suggestions, my progress in this work would have been much slower. Many thanks also to Dr. Cheong for answering all of my questions about SimRadar and iRadar, to Dr. Fulton for adding unique engineering perspectives to my work and for bringing so much life

into the RIL, and to Dr. Griffin for teaching us how to make the best of our time as grad students in SoM and the ARRC.

The first year of my work was supported by the National Science Foundation Grant No. 1823478, while my second year has been supported by the National Science Foundation Graduate Research Fellowship Program. To that end, I owe Dr. David Bodine, Dr. Cameron Homeyer, and Dr. Liz Pillar-Little so much gratitude for writing the recommendation letters that made my NSF GRFP application successful. The three of you have been my biggest supporters in the School of Meteorology through my time as a student at OU (six years total!). I also want to thank Dr. Erik Rasmussen for taking the time to discuss ideas for the research proposal portion of the application—every time we talk, I learn something new, for which I consider myself very lucky.

Finally, I owe a great deal of thanks to all of the friends and family who have supported me not only over the last two years, but across my life. To my friends: thank you for all the game nights, TV nights, long conversations about anything and everything, and constant encouragement. Your friendship has truly kept me going, through the pandemic and through grad school. To my cats: thank you for being the cutest roommates ever and for never judging my midnight Taco Bell dinners. And to Mom, Dad, and Nick: thank you for being endlessly, unconditionally supportive of everything I do. I am where I am because you have always fostered my curiosity and my love for weather. If I could choose my family, I would choose you every time.

Table of Contents

List Of Tables

List Of Figures

Abstract

The centrifuging of lofted tornadic debris is known to cause bias in Doppler radar measurements of tornado wind speeds. Debris presence in a radar volume is associated with anomalous radial divergence, underestimation of azimuthal wind speeds, and negative bias in vertical velocities, potentially resulting in erroneous interpretations of tornado structure. Using a simulation-based framework to study these errors, a variety of polarimetric radar time-series simulations from SimRadar are analyzed and compared in order to establish the relationships between debris field characteristics—such as debris size and number concentration—and the magnitude of bias in Doppler velocity and retrieved wind fields. Since debris characteristics also influence polarimetric measurements, we additionally seek to assess the relationships between velocity bias magnitude and relevant polarimetric variables. Establishing such relationships could support the development of a new moment-based approach to Doppler velocity bias correction for mobile research radars.

The latter half of this work introduces an alternative method for Doppler velocity bias mitigation utilizing novel spectral filtering techniques. Since debris is associated with unique polarimetric signatures as well as substantial velocity bias, this method incorporates dual-polarization spectral density (DPSD) estimation and fuzzy logic scatterer classification to identify debris-dominated signal contributions in a Doppler spectrum based on the velocity distribution of polarimetric characteristics. Outputs from the scatterer classification algorithm are used to suppress and filter the identified debris contributions within the original Doppler spectrum. New Doppler velocity estimates are calculated from the filtered signals, and comparisons are made against both the original velocity estimate and the true Doppler velocity to evaluate the effectiveness of these spectral filtering methods at reducing debris-related bias. In the future, these algorithms will be applied to observational data sets from mobile research radars.

Chapter 1

Introduction

Tornadoes produce intense damage over concentrated swaths of land, making them one of the deadliest, most destructive forms of severe weather on the planet. With over 1,200 tornadoes occurring each year on average (NCEI, 2021), the United States is consistently the most tornado-prone nation on Earth in terms of total numbers. From a comprehensive study of insurance catastrophe data, Changnon (2009) found that between 1949 and 2006, the average annual tornado-related economic loss was approximately $982 million per year, with nearly 800 distinct tornado events causing over $1 million each in damage during that time period. Though the economic losses of tornadoes are significant, the traumatic impacts are immeasurable to people living in a tornado's path. On average, tornadoes are the third largest contributor to weather-related fatalities in the nation behind flooding and extreme heat, causing between 60 and 70 deaths per year on average (NWS, 2019) and approximately 1,500 non-fatal injuries per year (NOAA, 2010) due to dangerously high wind speeds, structural damage, and the lofting and transport of debris.

Doppler radar is capable of observing the full kinematic structure of a tornado and its parent storm at meaningful spatiotemporal resolution, making it vital technology for operational forecasters and convective storm researchers alike. Doppler velocity observations, especially from mobile radars, are often used to draw conclusions about the intensity of tornadoes independently of official tornado damage ratings (Snyder and Bluestein, 2014). A major limitation of the original Fujita scale and the more

recent Enhanced Fujita (EF) scale is that tornado intensity is inferred solely based on post-event damage surveys, wherein the official reported intensity is determined by the most significant damage found within the path of the circulation (Fujita, 1971; WSEC, 2006). The result of these damage surveys is the systematic underrating of tornado intensity in sparsely populated regions, especially for significant (EF-2 or higher) tornadoes occurring in largely rural areas (Simmons and Sutter, 2011). For a detailed overview of the various caveats and limitations of damage-based intensity ratings, see Edwards et al. (2013). Because of the biases present in official intensity ratings, tornado researchers often instead use close-range mobile radar observations as an alternative, more kinematics-based approach to tornado intensity assessment (e.g., Wurman and Gill, 2000; Wurman and Alexander, 2005; LaDue et al., 2012; Toth et al., 2013; Kingfield and LaDue, 2015; Smith et al., 2020).

A major limitation of radar velocity measurements is that radars do not observe the air itself, but rather the motion of scattering objects within the atmosphere. Using Doppler velocity data to study tornado dynamics is contingent on the assumption that scatterers act as passive tracers that travel at exactly the same trajectory and speed as the ambient winds. While this assumption may be valid in most weather situations, numerous studies and experiments have proven that in tornadoes, object motion largely deviates from the underlying vortex wind field due to processes such as centrifuging and drag (e.g., Snow, 1984; Dowell et al., 2005; Lewellen et al., 2008; Bodine et al., 2016b). Radar estimates of tornadic winds thus suffer from substantial biases, resulting in a Doppler velocity field that is unrepresentative of the true wind field. In three-dimensional wind retrievals, debris tends to produce anomalous low-level radial divergence, severe underestimation of azimuthal wind speeds—especially near the radius of maximum winds (RMW)—and overall negative bias in vertical winds,

especially near the vortex core (e.g., Dowell et al., 2005; Wakimoto et al., 2012; Nolan, 2013; Bodine et al., 2014, 2016a).

A numerical method for estimating particle motion in a vortex was developed by Dowell et al. (2005) as a solution for mitigating debris centrifuging bias in radar estimates of tornadic winds. This method, based on approximations and simplifications to the governing equations for particle motion and number concentration, estimates an object's velocity as a function of its terminal fall speed and its radial distance from the vortex center. Difficulty arises in applying this technique from the dependence of these calculations on the object's fall speed, which translates to a dependence on the object's size. Thus, utilizing this method to correct debris-induced velocity errors requires that the physical characteristics of the lofted debris be known. While exact debris sizes and fall speeds are known in numerical simulation studies such as that performed by Dowell et al. (2005), these properties are largely unknown in observational studies. However, debris characteristics could potentially be inferred from the unique signatures produced by lofted debris in polarimetric observations of tornadoes.

Tornadoes are often associated with a distinctive polarimetric signature called the tornadic debris signature (TDS; Ryzhkov et al., 2002, 2005). The TDS was officially defined by Ryzhkov et al. (2005) to meet the following criteria:

- Low co-polar cross-correlation coefficient ($\rho_{HV} < 0.8$)
- Low differential reflectivity ($Z_{DR} < 0.5$ dB)
- High radar reflectivity factor ($Z_H > 45$ dBZ)
- Collocation of the above polarimetric signatures with a tornadic vortex signature (TVS; Brown et al., 1978)

Of these criteria, the strongest indicator for confirming the existence of a tornado is extremely low values of ρ_{HV} (Ryzhkov et al., 2005; Schultz et al., 2012a). Z_H can take

on a wide range of values in the vicinity of a tornado depending on the size of dominant lofted scatterers (Kumjian and Ryzhkov, 2008; Van Den Broeke and Jauernic, 2014; Van Den Broeke, 2015), and can be much lower than the 45 dBZ threshold determined by Ryzhkov et al. (2005). Additionally, while Z_{DR} is expected to be near zero for lofted debris, TDS observations often display negative values of Z_{DR}, suggesting either common vertical alignment of debris or resonance scattering effects (e.g., Bluestein et al., 2007; Bodine et al., 2014; Umeyama et al., 2018), while significant entrainment of precipitation can instead raise Z_{DR} to positive values within the TDS (Kumjian and Ryzhkov, 2008; Bodine et al., 2011). TDSs are often treated operationally as radar-based confirmation of a tornado in both real-time storm surveillance and post-event damage surveys (Ryzhkov et al., 2005; Schultz et al., 2012a,b; Saari et al., 2014).

The polarimetric characteristics of TDSs and their relationship to physical characteristics of the wind field present an attractive potential tool for diagnosing tornado intensity and damage potential in near-real time (Ryzhkov et al., 2005; Schultz et al., 2012a; Bodine et al., 2013; Gibbs, 2016; Griffin et al., 2017; Wakimoto et al., 2020; Wienhoff et al., 2020; McKeown et al., 2020). Correlations between observed damage intensity and average and extreme values of TDS polarimetric variables have been proposed based on the hypothesis that intense tornadoes produce more and larger debris, leading to relative increases in Z_H and reductions in Z_{DR} and ρ_{HV}. Spatial TDS characteristics are also believed to be related to tornado intensity and damage severity—it is hypothesized that the maximum height of a TDS column is related to the strength of the tornadic updraft, as stronger updrafts are able to loft debris higher, while the TDS diameter is related to the intensity and damage potential of the tornadic circulation.

Bodine et al. (2011) found a positive correlation between the maximum lowest-tilt Z_H and observed damage severity, suggesting that more intense tornadoes develop a higher concentration of small and fine-scale debris near the surface which can be

observed via radar. Bodine et al. (2013) extended that work to characterize relationships of damage intensity with lowest-tilt 90th percentile Z_H, 10th percentile ρ_{HV} and Z_{DR}, and TDS height and volume throughout tornadic life cycles. During tornado intensification, it was found that 90th percentile Z_H, TDS height, and TDS volume increase while 10th percentile Z_{DR} and ρ_{HV} decrease, and vice versa for tornado dissipation (although the applicability of TDS parameters is complicated by debris fallout). Similarly, Van Den Broeke and Jauernic (2014) found that TDS areal and vertical extent are positively correlated with tornado longevity and EF-scale rating, while Van Den Broeke (2015) found that higher EF-scale ratings are associated with increased Z_H and decreased ρ_{HV} within the TDS, and that maximum TDS height is primarily a function of tornado intensity. A significant caveat of these relationships is that, because of the wide variety of debris types lofted within a tornado, the limited nature of damage reporting, and the difficulty of obtaining detailed information about debris characteristics in observations, many of these relationships are qualitative and non-universal (Schultz et al., 2012a; Bodine et al., 2014). Further work is needed to develop these relationships into useful quantitative correlations.

The overarching goals of the work contained herein are to quantify and correct debris-induced errors in radar wind speed measurements using simulated polarimetric information about debris. The first objective of velocity bias estimation is performed as an extension of the work done by Dowell et al. (2005), which suggested qualitatively that relationships exist between centrifuging bias and physical characteristics of debris; however, this study did not account for debris scattering characteristics, which control the degree to which Doppler velocities become biased. This work thus seeks to more precisely quantify those relationships by incorporating debris scattering models, enabling us to examine the relative influence of debris characteristics such as size and concentration on velocity bias in greater depth and detail.

The second objective of velocity error correction is addressed using two different methods: a bulk (i.e., non-spectral) moment-based approach and a spectral approach. The moment-based approach involves correlating bulk polarimetric variables with corresponding velocity measurement errors to obtain empirical relationships that could potentially be used to infer velocity bias severity from polarimetric measurements. The spectral approach, contrarily, entails estimating polarimetric spectral densities and implementing a fuzzy logic scatterer classification algorithm in order to identify and filter debris-dominated contributions from a Doppler spectrum. Ideally, the debris-induced bias in a resolution volume will be reduced after Doppler velocity is recalculated using the resulting filtered spectrum. The overall performance of the spectral velocity correction methods is evaluated and discussed as a function of varying debris characteristics through the examination of velocity correction results for individual sample spectra and across full sector scans.

The remainder of this thesis will be structured as follows. Chapter 2 contains an overview of relevant background information on tornado dynamics, dual-polarization, and spectral signal processing. Chapter 3 provides a technical description of the radar time series simulator and its configurations, as well as an overview of dual-polarization spectral density estimation. Chapter 4 presents objective quantifications of Doppler velocity errors and how their severity correlates with the physical characteristics of debris, as well as a potential moment-based method for correcting debris-related bias. Chapter 5 discusses the design of a spectral filter to identify and remove debris contamination from a Doppler spectrum, and the effectiveness of this method in reducing the magnitude of velocity errors. Finally, Chapter 6 summarizes important findings and suggests directions for future work, particularly on the topic of debris-related velocity bias correction.

Chapter 2

Background

The problems posed in Chapter 1 fall at the intersection of several complex fluid dynamic and engineering concepts which must be understood in order to contextualize the motivation and conclusions of this work. This chapter provides the necessary background information to support the work in this thesis through an overview of each of these topics. A broad overview of tornado structure and vortex dynamics is given in Section 2.1. Section 2.2 presents a brief outline of weather radar theory and dual-polarization, along with descriptions of relevant radar-derived variables. Finally, Section 2.3 provides an overview of the fundamentals of radar signal processing and Doppler spectra.

2.1 Tornado Dynamics

Many reviews of tornado dynamics have been published over the past several decades. These reviews, which serve as compilations of a wide and comprehensive set of tornado-related publications, outline the state of tornado research and discuss which knowledge gaps have been filled, what questions still remain, and what new gaps have been opened in answering older questions. For detailed overviews of tornado dynamics and tornado vortex processes, refer to Rotunno (1986); Church et al. (1993); Davies-Jones et al. (2001); Markowski and Richardson (2010); Bluestein (2013); Rotunno (2013).

At its simplest, a tornado is defined as a rapidly and violently rotating column of air that extends from the surface to the cloud base of its parent storm. A typical tornadic circulation has a horizontal diameter on the order of 100 m, although extremely large tornadoes can have horizontal diameters on the order of 1 km. While most tornadoes have azimuthal velocities below 50 m s^{-1}, the strongest tornadoes can have measured velocities in excess of 75 m s^{-1}. Mobile research radars recorded azimuthal velocities up to 135 m s^{-1}, the highest wind speeds ever observed on Earth, in the May 31, 2013 tornado in El Reno, Oklahoma (Snyder and Bluestein, 2014), although the status of this measurement as the true maximum peak instantaneous velocity contains a degree of uncertainty due to the subjective velocity dealiasing methods as well as potentially unresolved vortices and subvortices (Bluestein et al., 2018). Vertical vorticity values within tornadoes are on the order of 1 s^{-1}. Strong nonlinear dynamic pressure perturbation effects create a low pressure perturbation at the center of the tornadic circulation. Because of this, tornadoes also have intense updrafts and radial inflow. The inflow region is a shallow layer near the surface—its depth is on the order of a only few tens of meters—with radial inflow velocities ranging from 20–60 m s^{-1}. Vertical velocities in tornadic updrafts can exceed 75 m s^{-1}, far stronger than the updraft speeds of their parent storms.

It is commonly assumed that tornadic flow is axisymmetric, meaning the flow characteristics are symmetric about the rotational axis of the tornado. Another common assumption is that tornado core flow is in cyclostrophic balance. Because tornadoes occur on small horizontal length scales, the primary force balance is between the pressure gradient force, directed toward the perturbation pressure minimum at the center of the tornado, and the centrifugal force, directed outward from the center of the tornado due to rotation. The assumption of cyclostrophic balance allows the perturbation pressure

within the tornado to be modeled as a function of radius in cylindrical coordinates, with the governing equation given as

$$\frac{\partial p'}{\partial r} = \frac{\rho v^2}{r}, \tag{2.1}$$

where p' and ρ are the perturbation pressure and air density at radius r, respectively. The minimum perturbation pressure, located at the center of the vortex, is given by $p'_{min} = -\rho v_{max}^2$, where v_{max} is the maximum azimuthal velocity.

2.1.1 Tornado Structure

The simplest conceptual model of tornado structure under balanced conditions is that of a Rankine vortex. A Rankine vortex is split into two distinct annuli, where the behavior and conserved quantities of the flow differ between the regions inside and outside of the radius of maximum wind (RMW). Within the RMW, the flow behaves as a solid-body vortex, which is characterized by a direct linear relationship between radius and azimuthal wind magnitude. In the inner region, angular velocity, and thus vorticity, are conserved with respect to radius such that $\omega = \frac{V_t(r)}{r}$ is constant, where V_t is the azimuthal velocity at radius r. Outside of the RMW, the flow behaves instead as a free vortex, a vortex model which is characterized by an inverse linear relationship between radius and azimuthal wind magnitude. Within the outer region, angular momentum, rather than angular velocity, is conserved with respect to radius such that $L = V_t r$ is constant.

Realistically, a tornadic circulation has not two, but five distinct flow regions: inner core, outer core, corner flow region, boundary layer, and overlying parent updraft (see Fig. 2.1). Located beneath the parent updraft are the inner and outer cores of the tornadic circulation, which together comprise the most of the tornado itself. The inner

core is a narrow column above the surface extending outward from the axis of rotation to the RMW. Flow within the inner core is in approximate cyclostrophic balance due to the intensity of rotation and large horizontal pressure gradient force in this region. There is almost no radial inflow within the inner core. The outer core surrounds the inner core, extending from the RMW to the outermost edge of the tornadic circulation. In contrast to the inner core, the flow in the outer core approximately conserves its angular momentum, meaning the intensity of rotation increases as air approaches the core. There is also a radially inward component to the rotating flow in the outer core. Due to the manner in which the flow behavior changes across the RMW, the inner and outer cores can be modeled using the dynamics of a Rankine vortex.

While the assumptions of Rankine vortex structure, cyclostrophic balance, and axisymmetry are valid for most of the tornado, they tend to fall apart in the lowest levels of the tornado due to frictional influences, which act to disrupt cyclostrophic balance and destabilize the flow. This means that the dynamics of the lowest regions of a tornado—the boundary layer and corner flow region—are much more complex than those of the previously described regions. The tornado boundary layer is a shallow layer, often only 10–100 m deep, where the coupling of intense cyclonic rotation with frictional influences creates a tornado-scale Ekman pumping effect. In this manner, friction induces strong radial inflow within the boundary layer. Through transport of angular momentum toward the inner core by the surface inflow, surface friction ultimately acts to intensify the tornado in the low-levels. The expected friction-induced strong radial inflow in the tornado boundary layer has been verified by numerical simulations of tornadoes, which have predicted that the strongest radial inflow should be within the lowest tens of meters of the circulation (e.g., Lewellen et al., 1997).

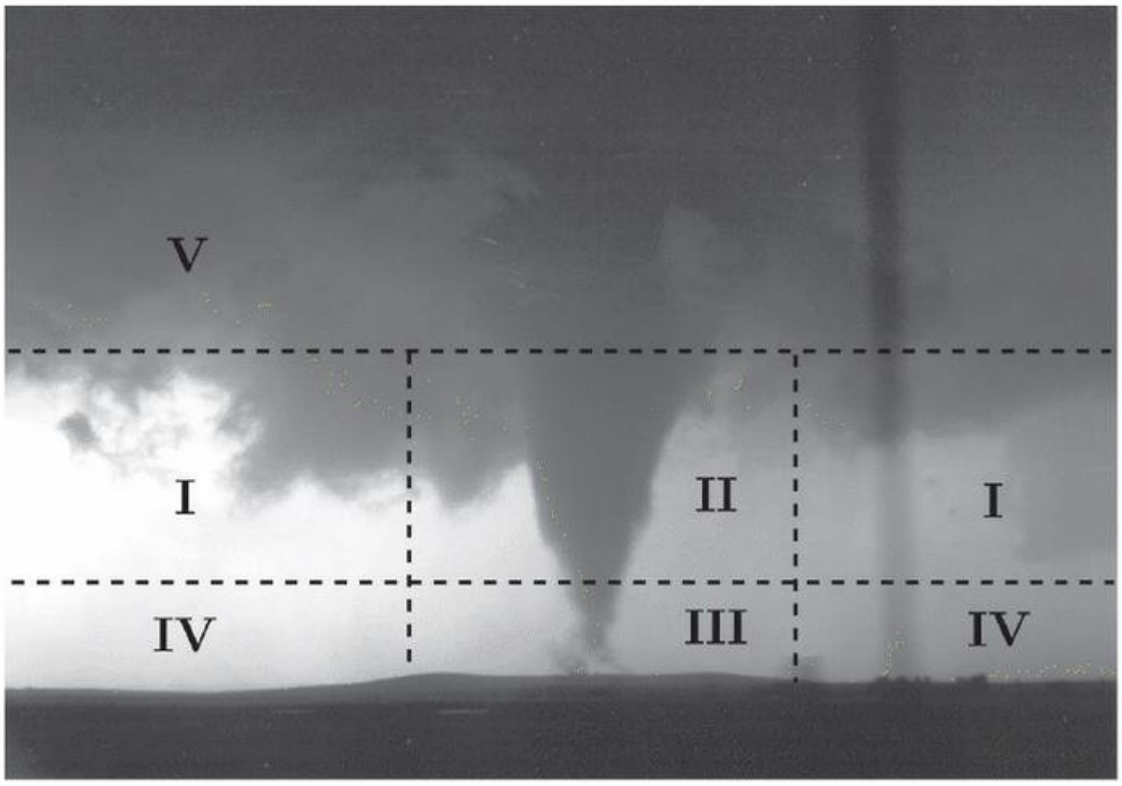

Figure 2.1: The five flow regions of a tornado: (I) outer core, (II) inner core, (III) corner flow, (IV) boundary layer, and (V) overlying updraft. Image originally from Markowski and Richardson (2010).

The corner flow region is the part of the boundary layer where the vortex core meets the surface and the low-level flow "turns the corner"—i.e., where the radial inflow turns abruptly upward into the vertical direction and becomes the tornado updraft. Because of the complex dynamics and dearth of observations of the corner flow, it is also the most poorly understood region of a tornado. The structure and dynamics of the corner flow are influenced by a multitude of factors including the overlying upper core circulation, low-level inflow, terrain characteristics, storm motion, debris loading, and the overall structure of the tornadic vortex (Lewellen et al., 1997, 2000; Gong et al., 2006; Lewellen et al., 2008; Bodine et al., 2016b; Satrio et al., 2020). In turn, the corner flow response to these influences may play a significant role in the structure, intensification, and overall evolution of the tornado as a whole (Lewellen et al., 2000; Lewellen and Lewellen, 2007).

Tornado structure is largely governed by a quantity called the swirl ratio (Davies-Jones, 1973; Church et al., 1979). Swirl ratio (S) is a dimensionless parameter derived from laboratory vortex chamber experiments that measures whether a vortex flow is dominated by updraft or rotation, and is given by

$$S = \frac{V_t}{w}, \tag{2.2}$$

where V_t is the azimuthal velocity at some radius and w is the mean vertical velocity at the top of the tornado. For a tornado with small swirl ratio (e.g., $S < 1$), the flow and structure are dominated by the updraft rather than rotation, resulting in a single-cell vortex with updraft throughout its depth. As swirl ratio increases ($S > 1$), tornado structure becomes increasingly dominated by rotation, inducing a downward-directed perturbation pressure gradient force in the center of the vortex due to nonlinear dynamical effects. A downdraft subsequently forms along the central axis within the

tornado updraft region. In a process termed "vortex breakdown", the interaction between the core downdraft and the surrounding central updraft causes the tornado to transition from a one-celled vortex to a two-celled structure. As swirl ratio continues to increase to larger values, the downdraft is able to reach the ground. Here, at the interface between the intensely rotating updraft and the weakly rotating downdraft, the abrupt radial gradients in azimuthal and vertical velocities induce shearing instability, causing the formation of multiple vortices that orbit around the parent circulation (Rotunno, 1978; Nolan, 2012).

2.1.2 Tornadic Debris Processes

Tornadic debris presents unique challenges to tornado researchers because of the complex processes that influence debris behavior and motion. Simulation studies have shown that debris loading can modify the tornadic wind field itself, especially in the lowest levels of the tornado where the majority of debris tends to remain rather than being lofted to higher altitudes (e.g., Wurman et al., 1996; Lewellen et al., 2004; Gong, 2006; Gong et al., 2006; Lewellen et al., 2008; Bodine et al., 2016b). Additionally, hydrometeors and debris particles in a vortex tend to follow trajectories and velocities that deviate substantially from the ambient mean winds due to the effects of drag, centrifuging, and fallout, with centrifuging being of particular importance in understanding the deviation of particle trajectories from the mean wind (Snow, 1984; Dowell et al., 2005; Lewellen et al., 2008; Wakimoto et al., 2012, 2020). A conceptual illustration of the phenomenon of particle centrifuging is shown in Fig. 2.2 (adapted from Wakimoto et al., 2012).

The discussion of debris effects here focuses primarily on those observed near the tornado vortex, as opposed to large-scale debris fallout (e.g., Snow et al., 1995; Magsig

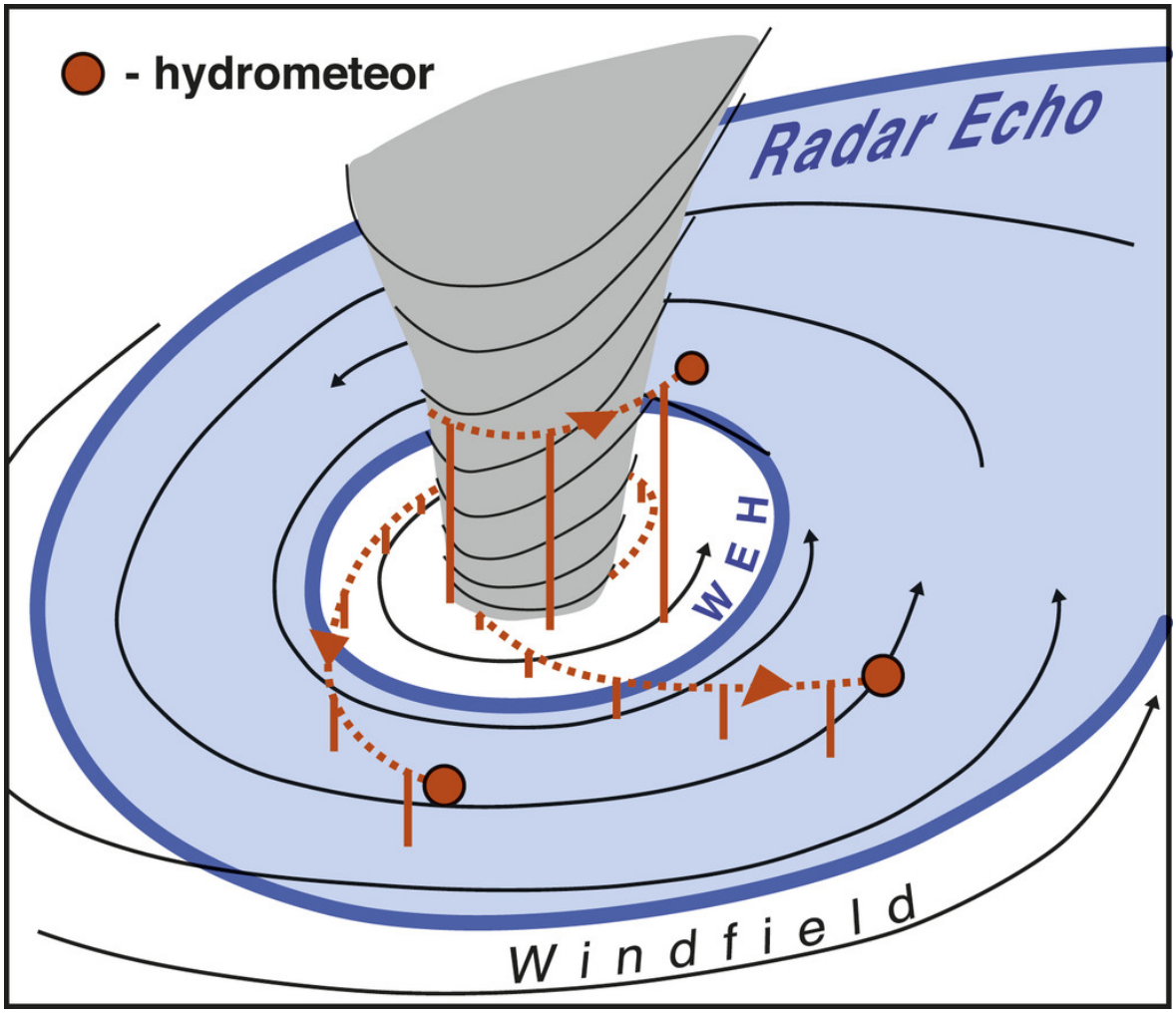

Figure 2.2: Illustration of centrifuged hydrometeor trajectories in a tornadic circulation. Image originally from Wakimoto et al. (2012).

and Snow, 1998). The rate of debris centrifuging is governed not only by tornado vortex characteristics, but by debris characteristics as well. Simulations by Dowell et al. (2005), and to some degree by Lewellen et al. (2008) as well, have demonstrated that larger debris particles are centrifuged and ejected more quickly than small debris. In particular, Dowell et al. (2005) showed that centrifuged rain drops tend to remain within the outer circulation and recycle through the inflow, while larger particles such as hail and debris are rapidly centrifuged and ejected from the circulation without recycling. It was additionally found that particle centrifuging increases with particle fall speed—since the maximum fall speed of a particle is largely dependent on its size and density, this means that larger, denser debris particles experience greater centrifugal accelerations.

The effects of debris centrifuging on radar observations are most clearly seen in Doppler velocity measurements and retrievals. Because debris particles experience intense centrifuging, it thus follows that Doppler velocity measurement errors will increase as well in the presence of debris, especially near the surface (Dowell et al., 2005). This conclusion was extended in both Dowell et al. (2005) and Nolan (2013) to include debris-induced errors in radar-derived velocity retrievals. In axisymmetric wind retrievals, the strongest signature associated with debris centrifuging is low-level positive radial bias, or even anomalous radial divergence where conceptual and numerical tornado models predict radial inflow. Other common wind retrieval errors due to debris centrifuging and fallout are the systematic underestimation of azimuthal velocities and the overestimation of axial downdraft speed and areal extent (Nolan, 2013).

These studies, however, did not consider electromagnetic scattering by debris and hydrometeor particles. In accounting for particle scattering, Bodine et al. (2016a) found a dependence of centrifuging errors on radar wavelength due to changes in scattering behavior at different wavelengths. While debris particles are the dominant scatterers

at longer wavelengths, shorter wavelengths tend to be dominated more by rain drops and thus tend to provide more accurate wind retrievals. Regardless, the centrifuging signatures and errors predicted by simulations have been reproduced in numerous high-resolution mobile radar data sets from tornadoes (e.g., Wurman and Gill, 2000; Bluestein et al., 2003; Lee and Wurman, 2005; Tanamachi et al., 2007; Kosiba et al., 2008; Wakimoto et al., 2012).

In addition to TDSs as discussed in the Chapter 1, debris centrifuging can also create a local minimum in Z_H at the center of the tornadic circulation surrounded by a closed ring of higher Z_H, often referred to as an "eye" or a weak echo hole (WEH; e.g., Wurman and Gill, 2000; Dowell et al., 2005; Bluestein et al., 2007; Wakimoto et al., 2011; Schultz et al., 2012a; Schultz, 2014). The outer ring of maximum Z_H corresponds to the accumulation of displaced debris and hydrometeors in sheaths surrounding the tornado, as illustrated in Fig. 2.2, and is likely collocated approximately with the RMW, as centrifuged raindrops tend to accumulate just outside the RMW (Dowell et al., 2005). Oftentimes, the WEH signature occurs primarily above the surface, with a Z_H maximum located directly near the surface, below the local Z_H minimum, due to the lofting of small and fine-scale debris (e.g., Bluestein et al., 2004; Wakimoto et al., 2011, 2020).

2.2 Fundamentals of Polarimetric Radar

Meteorologists use radar measurements to extract information from backscattered electromagnetic signals. The scattering and backscattering behavior of a target object depends on its physical properties such as size, shape, composition, phase, and motion. Based on knowledge of these scattering behaviors, scientists can retrieve information about the atmosphere and weather phenomena from radar signals.

Doppler radar operates on the principles of Rayleigh scattering, though many radars do operate within the Mie scattering regime, and scatterers often deviate from the Rayleigh assumption. The Rayleigh scattering regime describes wave scattering behavior for particles whose sizes are much smaller than the incident wavelength. Since radar wavelengths are on the order of 10 cm for S-band and 1 cm for other bands, while most hydrometeor diameters are on the order of 1 mm, the Rayleigh scattering approximation is generally valid for describing the electromagnetic scattering physics of hydrometeors. Under the Rayleigh approximation, particle wave scattering is modeled as dipole radiation from a sphere. When an incident wave encounters a small particle, an electric field is applied to the particle, causing the particle to become polarized. As the wave changes phase, the direction of the electric field changes as well, causing a reversal of the particle's polarization. Through this process, the particle acts as a dipole antenna by emitting a new electromagnetic wave after excitation by the incident wave.

Early radar systems transmitted in single-polarization, where the incident wave is polarized in only one dimension—typically the horizontal direction. From these single-polarization data, three radar moment variables can be obtained. Radar reflectivity factor, the zeroth spectral moment, is a measure of how much electromagnetic power has been returned to the radar via backscattering of power from the transmitted wave by hydrometeors and other particles. The reflectivity factor Z_h from a collection of rain drops is defined as

$$Z_h = \int_0^\infty N(D) D^6 dD, \tag{2.3}$$

where D is drop diameter and $N(D)$ is the drop size distribution (DSD), and Z_h is given in linear units of $\text{mm}^6\ \text{m}^{-3}$. For weather applications, Z_h is almost always converted into logarithmic units of dBZ via the relation $Z_H = 10\log_{10}(Z_h)$, where a lowercase

subscript denotes linear units and an uppercase subscript denotes logarithmic units. This is the conventional notation for linear and logarithmic quantities, and will be used throughout this thesis for variables related to signal power.

The other two single-polarization variables—Doppler velocity v and spectrum width σ_v—are related not to signal power, but instead to signal frequency. The first spectral moment v is defined based on the principle of Doppler shift, where the frequency of a signal is modified by the motion of its source. In weather radar applications, particle motions aligned with the radar beam induce a frequency shift in the backscattered signal. Since the original transmit frequency and the modified receive frequency are both known, the Doppler velocity of a scatterer is defined as

$$v = -\frac{\lambda f_D}{2}, \tag{2.4}$$

where λ is the radar wavelength and f_D is the Doppler shift frequency. Since a weather signal represents a distribution of many scatterers within a finite volume, there is variability in the measured velocities of scatterers in the volume, creating a return signal with a spectrum of frequencies rather than one single frequency. The second spectral moment σ_v, or the variability of measured velocities, can be used to evaluate the distribution of particle velocities within a resolution volume.

The single-polarization moments are invaluable measurements for meteorologists and other radar users, but a drawback of these quantities is that they contain no information about particle shape or orientation, which limits the conclusions we can reasonably draw about scatterer characteristics and physical processes in storms. Dual-polarization data, however, *does* contain this information. For this reason, utilizing

dual-polarization in weather radar technology allows for much more reliable and detailed conclusions to be drawn about scatterer characteristics. Per the recommendations of Doviak et al. (2000), most polarimetric radars utilize dual-linear polarization, wherein the radar transmits and receives two signals simultaneously and in-phase, with one wave having horizontal polarization while the other having vertical polarization. From these signals, several useful polarimetric variables can be calculated in order to study physical characteristics of scatterers in both the horizontal and vertical dimensions.

One such variable is differential reflectivity, or Z_{DR}, which represents the power ratio between the received signal power in the horizontal (H) and vertical (V) channels. This quantity is calculated as

$$Z_{DR} = 10\log_{10}\left(\frac{Z_h}{Z_v}\right) = Z_H - Z_V, \tag{2.5}$$

where Z_h and Z_H represent the H channel reflectivity factor and Z_v and Z_V represent the V channel reflectivity factor, in linear and logarithmic units, respectively.

Z_{DR} contains information about both the shape and orientation of scatterers within a resolution volume, assuming Rayleigh scattering. The amount of power returned in either channel is proportional to the size of the scatterer in the same dimension—a particle with greater horizontal width will return more power in the H channel than in the V channel. Therefore, a positive value of Z_{DR} means that scatterers within a resolution volume are on average wider than they are tall—or, in other words, they have common horizontal orientation. The reverse is true for negative Z_{DR}, which denotes common vertical alignment of scatterers within a volume. Finally, near-zero Z_{DR} can mean one of two things: either scatterers within a volume are roughly spherical, with similar sizes in both the horizontal and vertical dimensions; or scatterers are randomly

oriented such that there is no common alignment, and thus the average power returned in each channel is nearly equal.

A similarly common polarimetric variable is the co-polar cross-correlation coefficient, denoted as ρ_{HV} and generally referred to simply as the correlation coefficient. ρ_{HV} is a measure of the cross-channel correlation between the horizontal and vertical signal power from scatterers within a resolution volume. Similar to the Pearson correlation coefficient, this quantity is given by

$$\rho_{HV} = \frac{S_{hv}}{\sqrt{S_{hh}S_{vv}}} = \frac{|X_h X_v^*|}{\sqrt{|X_h X_h^*||X_v X_v^*|}}, \tag{2.6}$$

where X_h and X_v are the time series signals from the H and V channels, while S_{hh} and S_{vv} are the H and V channel signal power and S_{hv} is the cross-channel power.

Though Z_{DR} and ρ_{HV} are similar in that they can provide information about mean scatterer shapes, there are important differences between these two variables—namely, while Z_{DR} can be used to determine scatterer alignment, ρ_{HV} cannot. As a correlation measure, ρ_{HV} can only be positive-valued, and has weak dependence on orientation, although the value of ρ_{HV} is thought to decrease as scatterer orientations become more random. However, the approximate orientation independence of ρ_{HV} offers a different advantage over Z_{DR}. As described previously, Z_{DR} values are near-zero for both spherical particles and randomly oriented scatterers, but these cases are easily distinguished in ρ_{HV} information; spherical scatterers will produce ρ_{HV} values near 1.0, while irregularly shaped scatterers will produce much lower values of ρ_{HV} regardless of their orientation. When these two variables are used in conjunction with each other, Z_{DR} and ρ_{HV} can provide a wealth of information about scatterer shape and orientation.

A third common polarimetric variable is the specific differential phase, or K_{DP}, which quantifies the rate of signal phase shift between the horizontal and vertical channels as a function of range. This variable is calculated as

$$K_{DP} = \frac{1}{2}\frac{d\Phi_{DP}}{dr}, \tag{2.7}$$

where Φ_{DP} is the differential propagation phase shift, given by $\Phi_{DP} = \Phi_H - \Phi_V$. Φ_{DP} itself is a radially cumulative measure of the total shift between the H and V channel signal phases ($\Phi_{H,V}$) as the pulse moves outward from the radar.

When a wave travels through a field of scatterers, the amount of phase shift it experiences as it encounters each scatterer is relative to the size of the scatterer in the direction of the wave's polarization—a dual-polarized wave traveling through a field of horizontally oriented scatterers will experience a larger phase shift in the H channel. The more particles the wave encounters, the more its phase will shift as it travels through space, producing a greater phase difference between the H and V channels. While Φ_{DP} accumulates with radial distance from the radar, K_{DP}, as the radial rate of change of Φ_{DP}, does not, making K_{DP} more useful for identifying regions where signals experience the greatest degree of phase shift. K_{DP} can be used indirectly as a measure of drop size distribution because large rain drops are more oblate than small drops, leading to a larger differential phase shift between the two channels. A major advantage of K_{DP} is that, as a measure of signal phase, it is immune to attenuation effects. Therefore, K_{DP} can be used to obtain more robust estimations of rainfall rates as well as correct attenuation errors in Z_H and Z_{DR}.

2.3 Overview of Doppler Spectra

Radar data analysis can be performed in either the time domain or the frequency domain, which are fundamental concepts in signal processing. Raw data are typically collected in time domain form, where variations of the signal over time can be examined directly. These signal variations, especially for electromagnetic signals, are often periodic. A periodic signal can decomposed into a series of superimposed sinusoidal functions with varying frequencies via Fourier transforms, allowing the signal to be analyzed in the frequency domain as a function of frequency rather than as a function of time. For periodic signals, working in the frequency domain often simplifies mathematical analysis through the transformation of equations and operations into more easily solvable forms.

Radar time series data are collected as echo voltage signals. After passing through a series of filters, amplifiers, and mixers in the coherent receiver circuits, the voltage signal consists of an in-phase component $I(t)$ and a quadrature component $Q(t)$, which are superimposed to create a composite voltage phasor sample $V(t) = I(t) + jQ(t)$, hereafter referred to as an I/Q signal or I/Q data. The most common time-domain signal statistic used to analyze I/Q data is the autocorrelation function (ACF). The ACF is a measure of similarity of a signal $V(m)$ with itself over time, and is given by

$$R(l) = E[V^*(m)V(m+l)] = E[V^*(m-l)V(m)], \tag{2.8}$$

where l is the time lag by which the signal $V(m)$ is shifted and E denotes an expected value. For most weather radar signals, as the lag increases, the magnitude of the ACF tends to decrease, meaning weather signals decorrelate over time as the atmospheric conditions evolve.

Complex signals, such as those from radar, are often more straightforward to analyze in the frequency domain rather than the time domain. In radar data analysis, this is accomplished using the power spectral density (PSD), which represents the frequency distribution of signal power. Since signal frequency is related to the scatterer velocity, a PSD provides information about the predominant motion of scatterers within a resolution volume. Mathematically, the PSD is defined as the discrete Fourier transform (DFT) of the ACF, given by

$$sS(f) = \lim_{M\to\infty} T_s \sum_{l=-(M-1)}^{M-1} R(l)e^{-j2\pi f T_s l}, \tag{2.9}$$

where $R(l)$ is the ACF at lag l, T_s is the PRT of the radar, M is the number of samples in the time series signal, and f is the signal frequency. Because the periodic components of a time series signal $V(m)$ are preserved in its autocorrelation, the PSD as a Fourier transform of the ACF is useful for evaluating spectral statistics of the original time series signal.

The most commonly used PSD estimator is the periodogram estimator due to its simplicity and computational efficiency. To compute the PSD of a radar signal using this method, a DFT is first applied to the I/Q time series signal as

$$Z_{H,V}(k) = \sum_{m=0}^{M-1} d(m)V_{H,V}(m)e^{-j\frac{2\pi mk}{M}}, \tag{2.10}$$

where $V_{H,V}(m)$ is the I/Q signal corresponding to either the H or V channel, M is the number of samples in the time series, k is the spectral index ($0 \leq k < M$), and $d(m)$ is a data windowing function applied to the DFT to reduce spectral leakage. Using

the transformed signal, the periodogram estimators for the H, V, and cross-spectrum PSDs are calculated as

$$s\hat{S}_{H,V}(k) = \frac{|Z_{H,V}(k)|^2}{M}, \tag{2.11}$$

and

$$s\hat{S}_X(k) = \frac{Z_H(k)Z_V^*(k)}{M}, \tag{2.12}$$

where M, k, and $Z_{H,V}(k)$ are the same as above in equation 2.10 and the hatted quantity $s\hat{S}(k)$ represents an estimate of the true power spectral density $sS(f)$.

Because weather signals consist of a large number of independently measured samples, the central limit theorem can be applied to weather radar signals to conclude that a PSD from a precipitation signal should be approximately normally distributed and symmetric about a mean velocity $\mu = \overline{v}$ with standard deviation equal to the spectrum width σ_v. In practice, precipitation spectra has been shown to deviate significantly from a Gaussian distribution in approximately 25% of cases (Janssen and Van Der Spek, 1985); however, the assumption of normality remains standard for most weather radar signals (Doviak and Zrnić, 1993). The assumption of normality allows the radar signal to be described by its first three spectral moments—reflectivity factor, mean radial velocity, and spectrum width; or the zeroth, first, and second moments of the Doppler spectrum, respectively. An example of a quasi-Gaussian PSD from a weather signal is shown in Fig. 2.3.

The assumption of Gaussian-distributed Doppler spectra has been demonstrated to lose its validity in the case of a tornado vortex, which often produces a PSD with a distinct shape referred to as a tornadic spectral signature (TSS) (Zrnić et al., 1977; Zrnić and Istok, 1980; Zrnić et al., 1985). Observations of PSDs from tornadoes commonly display non-Gaussian features such as bimodal distribution, flattened spectral peak, or strong skewness. An example of a bimodal TSS is provided in Fig. 2.4 to illustrate

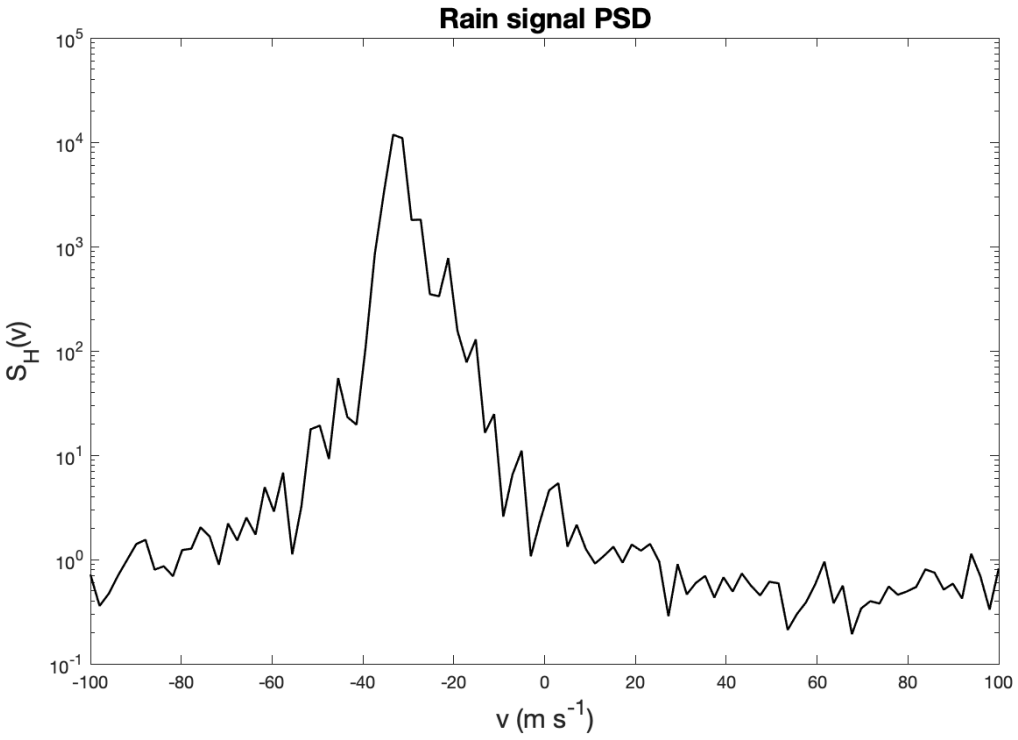

Figure 2.3: Example PSD from a quasi-Gaussian rain signal.

the often non-Gaussian nature of tornadic Doppler spectra. These departures from normality can likely be attributed in part to the effects of debris presence, due to its deviant and irregular motion.

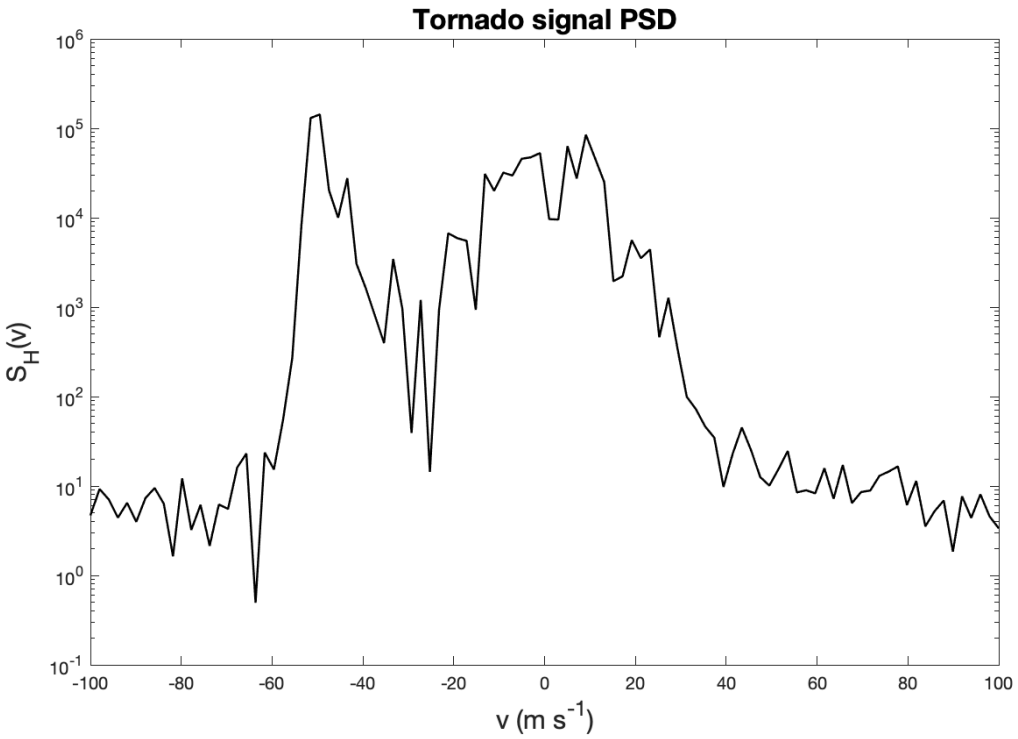

Figure 2.4: Example PSD from a non-Gaussian, bimodal tornado signal.

Chapter 3

Data & Methods

This work follows a simulation-based framework to study debris influences on wind speed measurements in a controlled manner. Studying the influence of debris on velocity measurements requires that the true velocity field be known in order to serve as a control data set, against which the measured debris-contaminated velocity fields are compared in order to quantify their differences. To accomplish this using observational data sets, we would need in situ measurements of the true tornadic wind field and characteristics of the debris field, which is not possible for a multitude of reasons—thus, a simulation-based approach is the only feasible method for this work.

As outlined earlier in this thesis, some work has been done to directly simulate the trajectories of debris and other lofted particles (e.g., Snow, 1984; Dowell et al., 2005; Lewellen et al., 2008; Maruyama, 2011; Bodine et al., 2016b; Umeyama et al., 2018). However, little work has been done to simulate radar observations of debris, which is a more operationally relevant aspect of tornadic debris studies. Therefore, the work presented in this thesis is novel in its use of realistic radar simulations to study debris processes and associated influences on Doppler velocity observations in tornadoes. This chapter provides an overview of these radar simulations and the software used to generate them, as well as a discussion of signal processing methods that are central to the spectral filtering aspect of this work.

3.1 SimRadar

SimRadar is a polarimetric radar time series simulator developed by faculty, research scientists, engineers, and students at the University of Oklahoma Advanced Radar Research Center in Norman, Oklahoma (Cheong et al., 2008, 2017). The SimRadar software package incorporates several different components in order to accurately model radar observations of tornadic debris. These components include high-resolution large-eddy simulations (LES) of tornadoes, air-drag model (ADM) data to accurately model debris trajectories and orientations, and modeled radar cross section (RCS) information to emulate debris and rain electromagnetic scattering. Included in the SimRadar software package are tables of preexisting LES, ADM, and RCS data for SimRadar to easily and efficiently look up at runtime. For a detailed discussion of the technical design and specifications of SimRadar, the reader is referred to Cheong et al. (2017). The source code for SimRadar is also available at https://github.com/OURadar/SimRadar.

A simplified chronology of the simulation process begins with the LES lookup tables. Output files from preexisting LES runs are ingested into SimRadar to serve as the background kinematic field in the simulation domain. The domain is then populated with rain ("background") and debris particles as specified by the user at runtime via command line input options. The trajectory and orientation of each debris particle within the background wind field is calculated at each time step using precalculated aerodynamic data ingested from the ADM lookup tables. Finally, electromagnetic debris scattering data, modeled using Ansys High-Frequency Structure Simulator (HFSS) software, are ingested from the RCS lookup tables in order to realistically emulate the radar signals received from across the domain.

In using SimRadar, the user is granted the ability to specify numerous characteristics of the emulated radar, including wavelength, pulse repetition time (PRT),

beamwidth, scanning mode (i.e., plan position indicator [PPI] or range-height indicator [RHI]), sector scan width, and the number of sector sweeps to be collected within an individual simulation. Giving users the ability to fully customize the radar characteristics and parameters allows SimRadar to be used to emulate real radar systems for comparisons between simulations and observations. Additionally, users are able to specify many characteristics of the simulation configuration itself; the most important of these model configuration inputs in this work are LES wind field, debris type and concentration, and simulation concept.

The LES input parameter specifies an LES configuration to serve as the background kinematic field for the radar simulator. A more detailed discussion of the LES model and configuration used in this work is contained in Section 3.1.1 of this chapter. After SimRadar ingests the LES data, the model domain is populated with rain and debris. For each simulation, debris types and number concentrations are chosen—each debris type input must be paired with a debris concentration input, which dictates the total amount of the associated debris type to be populated throughout the entire model domain. SimRadar can be run with multiple debris types in the same simulation simply by specifying multiple debris type-concentration pairs in the run command, and it can also be run with no debris by leaving out those inputs entirely. Descriptions of the predefined debris types and their characteristics are compiled in Table 3.1. To ensure that the debris particles are actually lofted by the simulation winds, debris injection occurs at a predefined minimum height of 10 m above the bottom of the domain.

The simulation concept input parameter allows the user to dictate more specific configurations related to the numerical simulations of debris and background rain. Any number of the predefined concept options can be specified for a given simulation, although a few of these options do directly contradict each other. While several

Table 3.1: List of SimRadar predefined debris types with their dimensions and RCS calculation method.

Debris Type	**Dimensions (inches)**	**RCS Method**
d1: Leaf	0.08 × 1.6 × 1.6	HFSS
d2: Leaf	0.04 × 3.2 × 2.4	HFSS
d3: Wood board	2 × 12 × 4	HFSS
d4: Wood board	4 × 12 × 8	HFSS
d5: Metal sheet	0.04 × 40 × 40	HFSS
d6: Brick	2.5 × 8.5 × 4.5	HFSS
d7: Wood board	1.5 × 96 × 3.5	HFSS
d8: Wood board	1.5 × 48 × 3.5	HFSS
d9: Wood board	1.5 × 24 × 3.5	HFSS
d10: Wood board	1.5 × 12 × 3.5	HFSS
d11: Wood sheet	0.25 × 48 × 48	HFSS
d12: Wood sheet	0.25 × 36 × 36	HFSS
d13: Wood sheet	0.25 × 24 × 24	HFSS
d14: Wood sheet	0.25 × 12 × 12	HFSS

concept options are built into SimRadar, the most important options related to this work in particular are dragged background, transparent background, uniform drop size distribution (DSD), and power-law debris concentration.

The dragged background option determines the behavior of the rain background with which the model domain is populated. If this option is not selected, the background rain drops will follow the exact trajectory of the LES wind field. If the dragged background option *is* specified, then drag influences will be included in the rain drop trajectory calculations, creating a more realistic simulation of hydrometeor motion. Bodine et al. (2016b) provides a more detailed discussion of the two-way air-particle coupling scheme used in SimRadar for calculating rain drop trajectories. Contrarily, the transparent background option determines whether the background rain should contribute to the radar signal at all. If this option is selected, then rain will not be injected into the model domain at all, and thus the only scatterers observed by the radar will be debris particles without any added rain influence. If this option is not selected, then rain will be populated into the model domain along with debris, and both scatterer types will contribute to the radar output data.

The uniform DSD option is intended to improve the computational efficiency of simulating rain drop trajectories. When this option is selected, the model domain is populated with rain drops of uniform physical size, thus reducing the computational load of trajectory calculations to only one drop size. To maintain the realism of the simulation, a distribution of scaled RCS following a Marshall-Palmer DSD is applied to the rain background across the domain. The implementation of scaled RCS distributions with this option ensures that while the trajectory calculations are simplified, the scattering behavior of the background rain still represents a realistic DSD. The scaled RCS method is the most common DSD modeling option used for SimRadar applications due to its computational efficiency.

The power-law debris concentration option determines debris flux based on the background LES wind field at 10 m above the surface level. If this option is not specified, debris particles are injected throughout the model domain independently of the wind field, which does not account for the fact that in a physical tornado, the lofting of debris is driven by the ambient wind field. The wind speeds must be sufficiently large to initiate damage at all, and more debris should be lofted in areas of stronger winds. Thus, when this option is specified, debris particles are selectively injected only into regions of the model domain where the horizontal velocity exceeds a predefined threshold wind speed—in this work, the threshold wind speed is 20 m s^{-1}. The spatial distribution of debris is modeled as a power-law relationship with background velocity following Batt et al. (1999). By emulating the dependence of debris flux on the background wind field, this option enables more realistic simulation of actual debris behavior within a tornadic circulation.

3.1.1 Large-Eddy Simulation

The simulated tornadic wind fields utilized in SimRadar are generated using an LES model based on the Research Institute for Applied Mechanics Computational Prediction of Airflow over Complex Terrain (RIAM-COMPACT) model developed at Kyushu University (Uchida and Ohya, 2003). The LES model was modified to simulate tornadic winds using a vortex chamber plate configuration by Maruyama (2011), to which the reader is referred for more detailed discussion on the simulation of tornado-like vortices. Bodine et al. (2016b) further modified this model configuration to eliminate the simulated plates; this configuration is the one ultimately used to generate LES tornadic wind fields for ingestion into SimRadar, with additional modification described below for specific simulations herein.

The simulated flow is that of a mature two-celled tornado beginning to undergo vortex breakdown, although all analyses in this thesis are performed at time steps prior to the onset of breakdown, meaning that the vortex represented in all subsequent analyses is a one-celled vortex. The updraft is initialized at the upper boundary of the domain with a horizontal radius of 650 m, or a diameter of 1.3 km, and a mean and maximum vertical velocity of 21 m s^{-1} and 30 m s^{-1}, respectively. The prescribed inflow layer is shallow, with a depth of 300 m. The initial mean angular momentum at the side boundaries of the domain is $L = 12,629$ m^2 s^{-1}, and the vortex is initialized with a swirl ratio of $S = 3$. Figs. 3.1 and 3.2 show the initial kinematic structure and angular momentum, respectively, of the simulated tornado-like vortex in the lower half of the model domain.

The LES model used in this work has a domain 1.3 km in width and 2 km in height, and contains 195 grid points in the x and y dimensions and 79 grid points in the z dimension. The initial conditions of the simulation are defined with a roughness length of $z_0 = 0.1$ m. The model is configured with stretched grid spacing throughout the domain such that the maximum spatial resolution occurs at the surface and tornado center, with progressive stretching of the grid spacing with horizontal distance from the center of the domain and vertical distance from the surface, in order to study the complex low-level dynamics of the vortex. The lower boundary condition used in this model is a semi-slip condition, and subgrid-scale turbulence is modeled using the Smagorinsky scheme (Smagorinsky, 1963).

3.1.2 SimRadar Configurations

The simulation volumes considered in this work are composed of vertically stacked PPI sector scans in order to perform analyses and comparisons volumetrically and

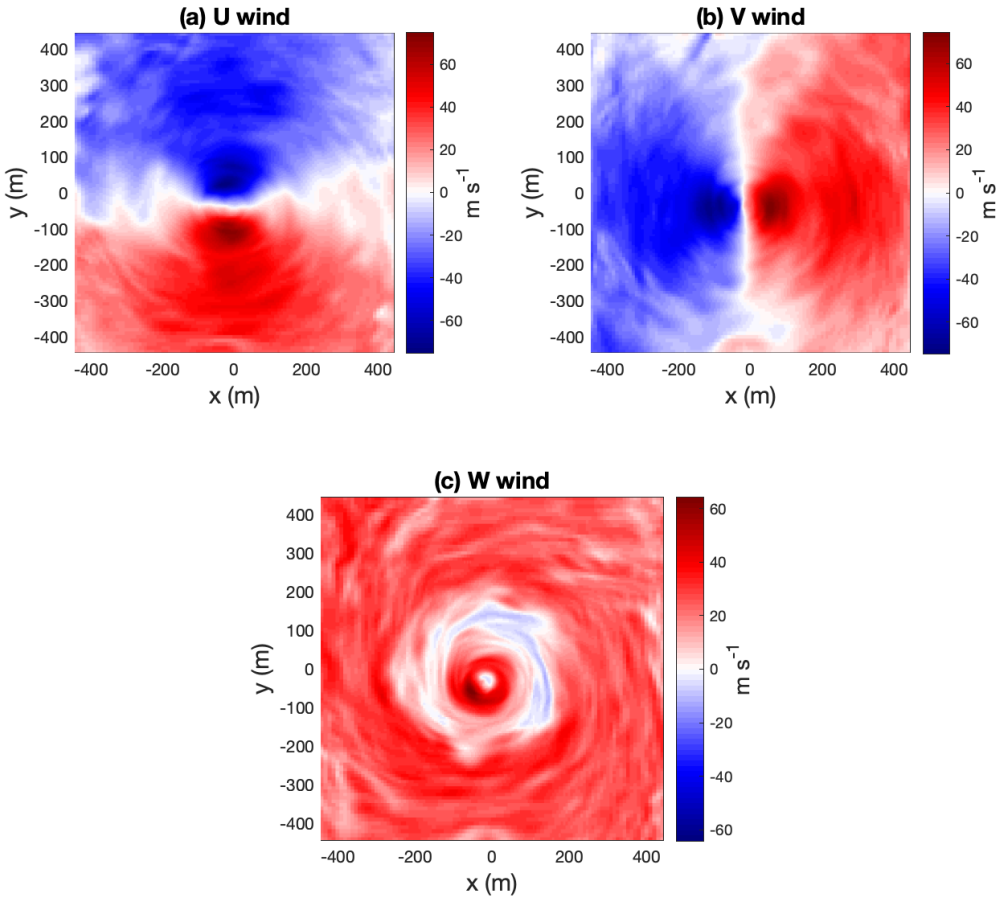

Figure 3.1: Horizontal cross sections of the (a) u, (b) v, and (c) w winds (m s^{-1}) at $z = 750$ m at the first time step in the model run.

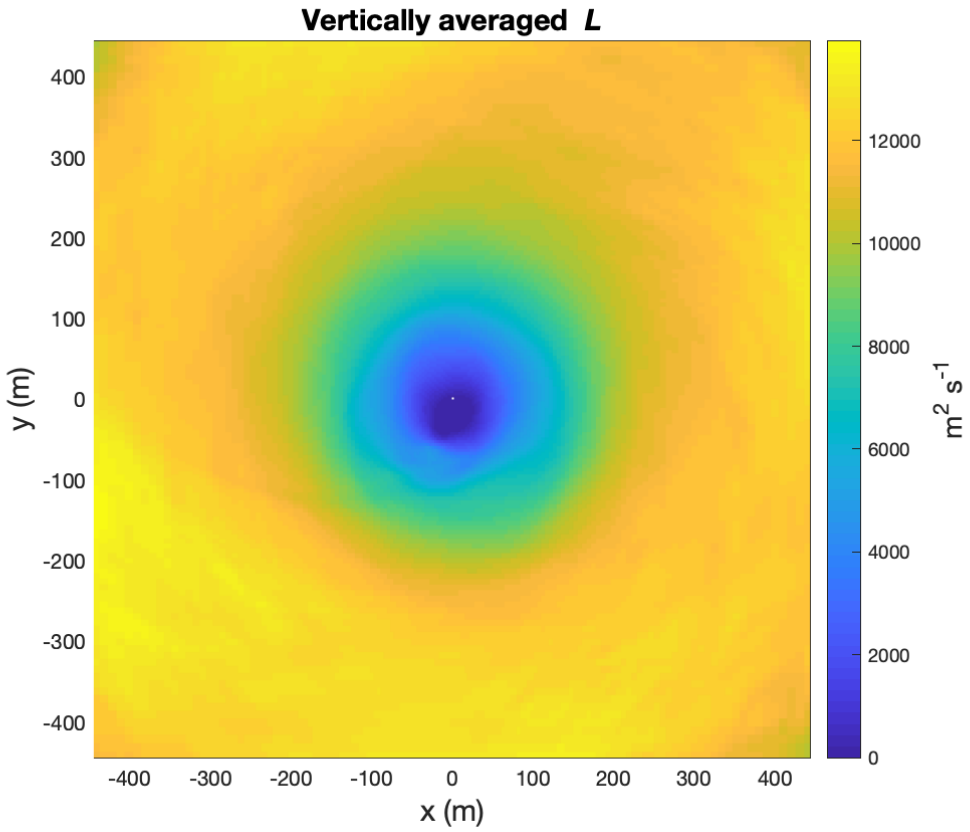

Figure 3.2: Vertically averaged angular momentum L ($\mathrm{m}^2\ \mathrm{s}^{-1}$) between 0–750 m at the first time step in the model run.

at multiple heights. To achieve very high spatial sampling resolution, each sector is centered approximately 2 km from the radar, with an azimuthal resolution of 0.5° and a default radial resolution of 30 m. There are 48 radials in a sector and 21 range gates per radial—with the given angular and radial resolutions, this comes out to a 24°-wide sector with a total radial depth of 630 m. These scans are collected at elevation angles from 0.5° to 5.0° in increments of 0.5°, resulting in a volume of 10 vertically stacked sector scans. The simulation domain is sampled at an S-band wavelength of 10 cm and a PRT of 0.00025 s (0.25 ms) to attain an aliasing velocity of 100 m s^{-1}.

The simulations used in this work can be divided into three main classifications in order to study the differences between radar measurements of meteorological scatterers and tornadic debris. As discussed earlier in this chapter, analysis of debris-induced velocity errors requires a control data set to represent the true wind field. Therefore, a simulation without debris was run at every elevation angle for any given simulation—this is the first simulation type, and the simulations using this rain-only configuration are hereafter referred to as the "rain" simulations. Because these simulations contain only rain, they serve as this work's control data sets. The rain simulations were run with dragged background, uniform DSD with scaled RCS, and power-law debris flux concept options. An example PPI sector scan for a rain simulation is shown in Fig. 3.3.

The second simulation type encapsulates SimRadar simulations that were run with debris, but without background rain by using the transparent background and power-law debris flux concept options. Simulation runs with this debris-only configuration are hereafter referred to as "debris" simulations. These debris simulations are primarily used for the work in Chapter 5 for identifying and quantifying the distinct spectral characteristics of debris without any potential interference from rain signals in the data.

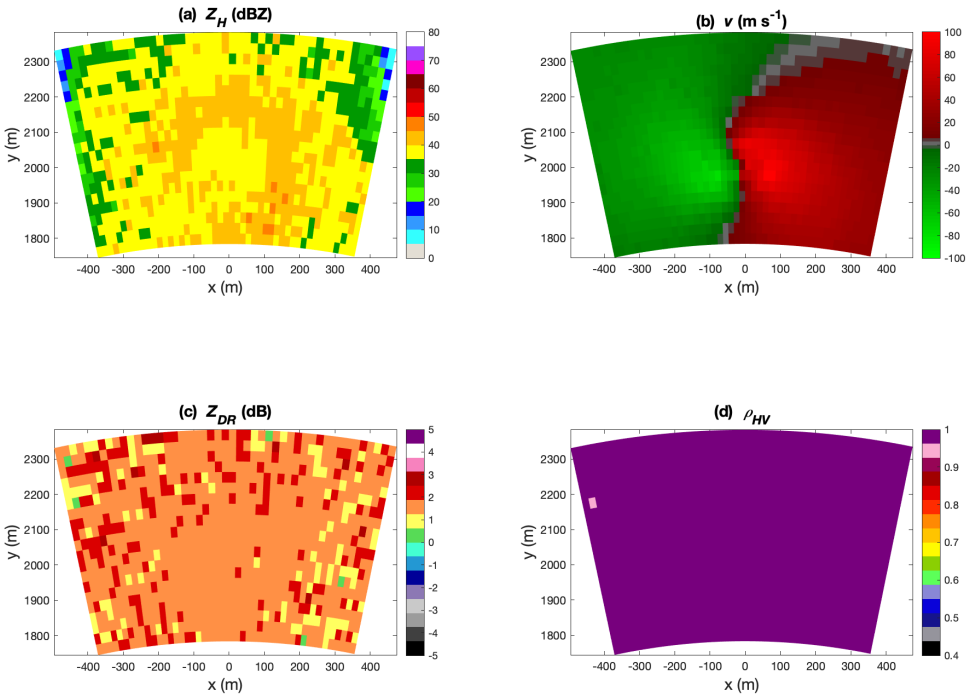

Figure 3.3: Color fill PPIs of (a) Z_H (dBZ), (b) v (m s^{-1}), (c) Z_{DR} (dB), and (d) ρ_{HV} for a rain simulation.

For the error quantification analysis in Chapter 4, however, no debris-only simulations are used because the lack of rain in the signal diminishes its representativeness of a realistic signal, which should include contributions from both rain and debris in a tornado.

The third simulation type represents a more realistic radar signal including both rain and debris in the domain—these simulations are thus hereafter referred to as "realistic" simulations. Similarly to the rain simulations, this SimRadar configuration is attained using the dragged background, uniform DSD with scaled RCS, and power-law debris flux concept options. The combination of the dragged background with the power-law debris flux is especially important in these simulations, as specifying these options ensures that the modeled trajectories of both debris and background rain are as physically realistic as possible. Because this configuration is intended to be the most representative of real signals from tornadoes given the defined scatterer options in SimRadar, these simulations are the main focus of all analyses in this work. An example PPI sector scan for a realistic simulation is shown in Fig. 3.4. By using the previously described rain and debris simulations as comparison data sets to quantify debris-induced velocity errors and distinguish spectral characteristics in the realistic simulated signals, we can test a variety of different scenarios encountered in nature and determine the best way to estimate and mitigate debris velocity bias.

The work in this thesis primarily focuses on the leaf and wood board models represented by debris types 1 through 4 in Table 3.1 (Lujan, 2016; Cheong et al., 2017). Since the first six debris types were generated earlier than the wood board and wood sheet models represented by debris types 7 through 14, they have undergone more testing and evaluation to ensure the simulated returns they produce are realistic. While the analyses in this work were performed for all debris types, the metal sheet and brick

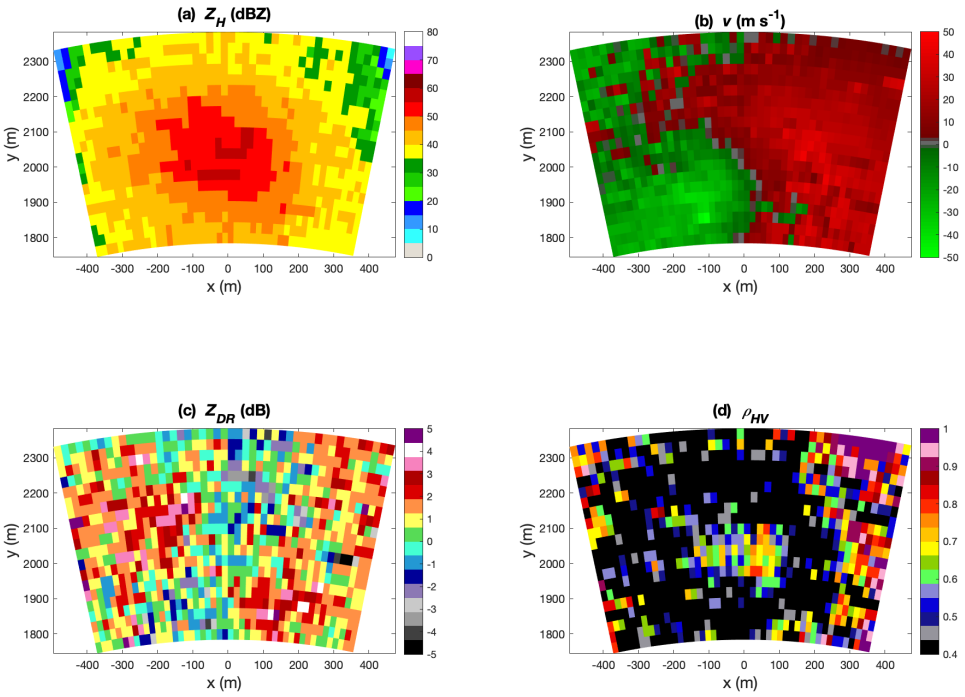

Figure 3.4: As in Fig. 3.3, but for a realistic simulation.

models (debris types 5 and 6) receive less attention because they were only modeled at one size each, whereas the leaf and wood board debris types were modeled at multiple sizes each.

Because several predefined debris types in the SimRadar RCS tables represent different sizes of the same material, we are able to study velocity error magnitude as a function of debris particle size without needing to account for variation in the scattering characteristics between materials. Another goal of this work is to study velocity error magnitude as a function of debris particle concentration, as most prior work in the realm of relating debris properties to velocity measurement errors has placed more emphasis on the role of debris size rather than debris concentration. To achieve this goal, we chose to run all of the debris and realistic simulations with debris concentrations varying between 10,000, 100,000, and 1,000,000 particles (hereafter referred to as "low", "medium", and "high" concentrations, respectively). It is noted that while the larger debris concentrations might be very high in terms of the total debris number, only a small subset of the debris (around 10%) is actually lofted to the altitude of the simulated radar beam in SimRadar. Therefore, the amount of debris actually lofted to the beam height may be physically realistic, even for very high total debris concentrations. Additionally, there is significant uncertainty in debris observations, which is why we have chosen a wide range of debris concentration values. Since debris trajectories are complex, it is not possible to predict where debris will or will not be lofted.

As shown in the flowchart in Fig. 3.5, a total of 850 simulated sector scans are generated for each LES base, as each individual simulations only represents one elevation angle, one debris type at a single concentration, and one configuration (rain, debris, or realistic). Therefore, the prioritization of only a few debris types and concentrations

serves to simplify the data analysis and visualization by reducing the amount of data to be considered.

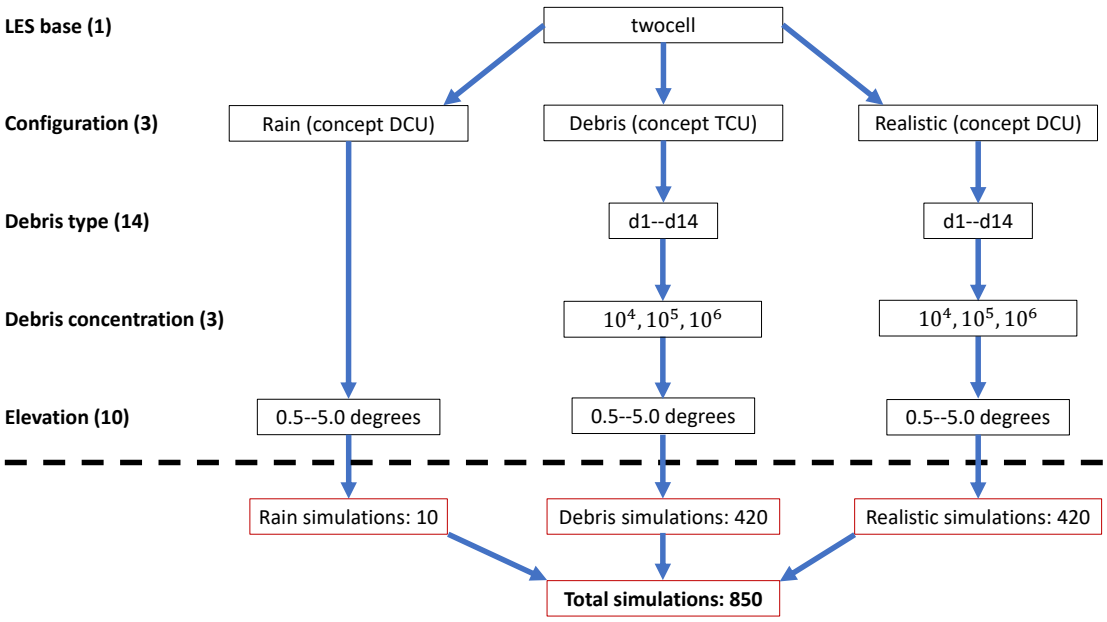

Figure 3.5: Flowchart of all SimRadar simulations generated for a given LES model based on the variation of input parameters to obtain a comprehensive set of simulations.

3.2 Dual-Polarization Spectral Density

As has been shown in prior work, raindrops and debris do not travel at the same airspeed in a tornado, and often follow significantly different trajectories as well. If a tornado is sampled by Doppler radar at sufficiently high spatial resolution—that is, if the size of the radar resolution volume is much smaller than the tornado—then the differing motion of precipitation and debris may be distinguishable within the Doppler spectra. Under these sampling conditions, we therefore expect that Doppler spectra from tornadoes would tend to feature bimodal power distributions, where one peak is associated with the motion of small meteorological targets like rain drops, and the other is associated with the motions of tornadic debris being lofted, centrifuged, and ejected. Because rain drops experience considerably less aerodynamic drag or centrifuging than debris, they are more accurate tracers of the surrounding wind field. Therefore, the spectral peak associated with raindrop motion can be taken as the true Doppler velocity representing the tornadic winds. This raises an important question: how can we determine whether a spectral peak is associated with raindrop motion or the deviant motion of debris? To this question, the dual-polarization spectral density (DPSD) presents a compelling solution.

Like a PSD, a DPSD is a spectral distribution of polarimetric variables, which allows us to analyze quantities such as Z_{DR} or ρ_{HV} as functions of velocity within a resolution volume. Because the trajectories and polarimetric characteristics of debris are significantly different from those of rain, DPSDs can be utilized as a method for identifying debris and rain within a radar spectrum. DPSDs can be calculated for any polarimetric variable, but this study will focus on spectral differential reflectivity

($s\hat{Z}_{DR}$) and spectral correlation coefficient ($s\hat{\rho}_{HV}$) as these variables are the most relevant to tornadic debris studies, and are more commonly collected than polarimetric variables obtained with other polarization modes.

To illustrate the proposed method, Fig. 3.6 shows an idealized example of tornadic radar spectra. In this hypothetical case, the PSD (a) is bimodal with distinct peaks at different velocities representing rain and debris (hereafter referred to as rain and debris peaks). The DPSDs (b-c) then show the expected distributions of $s\hat{Z}_{DR}$ and $s\hat{\rho}_{HV}$. In the PSD, the rain peak is spectrally collocated with positive $s\hat{Z}_{DR}$ and $s\hat{\rho}_{HV}$ near 1.0, which are values typically associated with rain in a bulk (non-spectral) sense. Similarly, the debris peak is collocated with negative $s\hat{Z}_{DR}$ and low $s\hat{\rho}_{HV}$, which matches typical bulk polarimetric signatures of debris. In summary, this figure illustrates our hypothesis that where the magnitudes of $s\hat{Z}_{DR}$ and $s\hat{\rho}_{HV}$ are characteristic of rain, the corresponding velocity returns are dominated by rain motion, and vice versa for debris.

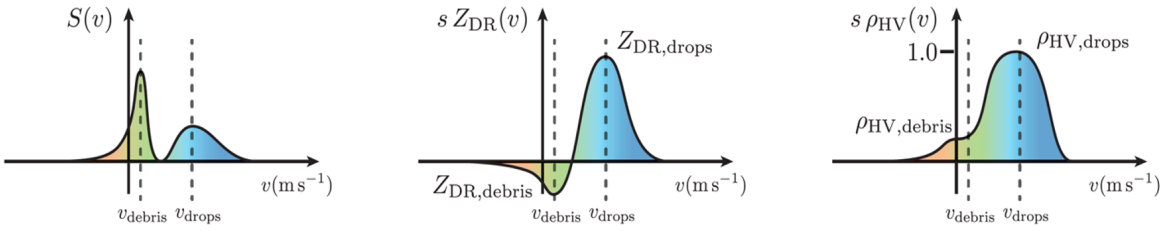

Figure 3.6: Idealized plots of (a) $s\hat{S}(v)$ (dB), (b) $s\hat{Z}_{DR}(v)$ (dB), and (c) $s\hat{\rho}_{HV}(v)$.

While the bulk polarimetric variables are calculated from bulk signal statistics, DPSDs are calculated from the spectral statistics of PSDs. The two spectral polarimetric variables used in this thesis—spectral differential reflectivity and spectral correlation coefficient—are estimated as

$$s\hat{Z}_{dr}(k) = \frac{\sum_{i=1}^{K} s\hat{S}_H^{(i)}(k)}{\sum_{i=1}^{K} s\hat{S}_V^{(i)}(k)}, \tag{3.1}$$

and

$$s\hat{\rho}_{HV}(k) = \frac{|\sum_{i=1}^{K} s\hat{S}_X^{(i)}(k)|}{\sqrt{\sum_{i=1}^{K} s\hat{S}_H^{(i)}(k) \sum_{i=1}^{K} s\hat{S}_V^{(i)}(k)}}, \tag{3.2}$$

where $s\hat{S}_H$, $s\hat{S}_V$, and $s\hat{S}_X$ respectively are the horizontal, vertical, and cross-spectrum PSD estimates as defined in Eq. 2.11–2.12, K is the number of independent spectra, k is the spectral index, and $s\hat{Z}_{dr}$ is given initially in linear units. To obtain meaningful DPSD estimates, averaging across multiple independent spectra ($K > 1$) is required, as it can be shown that estimation using a single spectrum produces $s\hat{Z}_{dr}$ with high spectral variance and renders $s\hat{\rho}_{HV}$ meaningless by always producing a value of 1. However, the averaging of multiple spectra introduces other non-negligible detrimental effects on the quality of DPSD estimates which are relevant to this work.

3.2.1 Bootstrap DPSD Estimation

Traditional methods for DPSD estimation generally either involve averaging PSDs in frequency (e.g., Bachmann and Zrnić, 2007) for a single-dwell estimate, or averaging in range, azimuth, or time for multiple-dwell estimates (e.g., Moisseev and Chandrasekar, 2009). The averaging process inherently results in smoothing of data, causing resolution loss in whichever dimension the averaging took place. For tornado studies and spectral debris identification especially, signal resolution loss in any of these dimensions would substantially diminish the amount of information that can be gleaned from the DPSD, thereby degrading the scientific value and robustness of any conclusions drawn.

The most obvious example of information degradation comes from spatial averaging, either in range or azimuth. Because most tornadoes are already coarsely resolved with 1°-beamwidth radars (except for extremely large tornadoes), any form of spatial averaging would easily mask important features of the tornado. Averaging in time is also a poor choice because in addition to small spatial scales, tornadoes also occur on

short time scales—on the order of tens of seconds. In comparison, a typical weather radar such as the WSR-88D requires several minutes to complete a full volume scanning pattern, which is already quite detrimental to studying tornadoes at a meaningful temporal resolution. Therefore, temporal averaging would also easily mask valuable information about the spatiotemporal evolution of the tornado.

Spectral averaging at least allows for single-dwell estimation of the DPSD and the preservation of spatiotemporal resolution; however, there are still substantial issues associated with frequency-domain averaging which degrade the utility of any such DPSDs for tornado studies. First, frequency averaging across a single PSD results in lower-quality DPSD estimates with large bias and variance, making it difficult to discern the signal from artificial noise (Umeyama et al., 2017, 2018). Second, frequency averaging leads to the reduction of velocity resolution through spectral smoothing, which masks valuable spectral information necessary for tornado studies. Given that the goal of this work is to analyze spectral distributions of polarimetric characteristics, preserving the spectral resolution of the data is vital.

To overcome the limitations of traditional DPSD estimators, Umeyama et al. (2017) developed a novel alternative method that utilizes bootstrap resampling of I/Q signals in order to generate multiple spectra for averaging while preserving the spectral characteristics of the original signal as much as possible. Three instances of the original polarimetric time series $\mathbf{V}_{H,V}$ are first concatenated to create an extended time series signal. K independent blocks of length M are randomly drawn from the extended signal using bootstrap resampling. The H, V, and cross-channel PSDs are then calculated for each sample block using Eq. 2.11 and 2.12 (with each time series multiplied with a Blackman-Harris data windowing function to suppress spectral leakage), and finally the DPSD estimates $s\hat{Z}_{dr}$ and $s\hat{\rho}_{HV}$ are calculated using Eq. 3.1 and 3.2 such that averaging is performed across the set of bootstrapped blocks. By utilizing bootstrap

resampling methods, this technique produces meaningful DPSD estimates while maximizing the preservation of spectral and spatiotemporal information from the original radar signal. The reader is referred to Umeyama (2016) and Umeyama et al. (2017) for a full description of this method and its implementation.

3.2.2 Polarimetric Time Series Emulator

Although the algorithms in this work are ultimately written to accept SimRadar files as their input data sets, the initial design of the DPSD algorithm was built and tested with a simple polarimetric I/Q time series emulator. The polarimetric emulator design is detailed in Yu et al. (2012), and is based on the time series simulation technique originally proposed by Zrnić (1975). Briefly, the polarimetric I/Q emulation technique in Yu et al. (2012) uses pre-specified model spectra of vertical channel power $S_V(v)$, $sZ_{DR}(v)$, and $s\rho_{HV}(v)$ to generate the appropriately correlated I/Q time series signals for the H and V channels. By using the emulated time series signals as inputs for the DPSD estimation algorithm during development, we were able to compare the output DPSDs to the originally specified model spectra, which was invaluable in debugging and verifying that the calculations were free of errors. A comparison between the input DPSDs used to generate the time series and the resulting bootstrap method DPSD estimates are shown in Fig. 3.7.

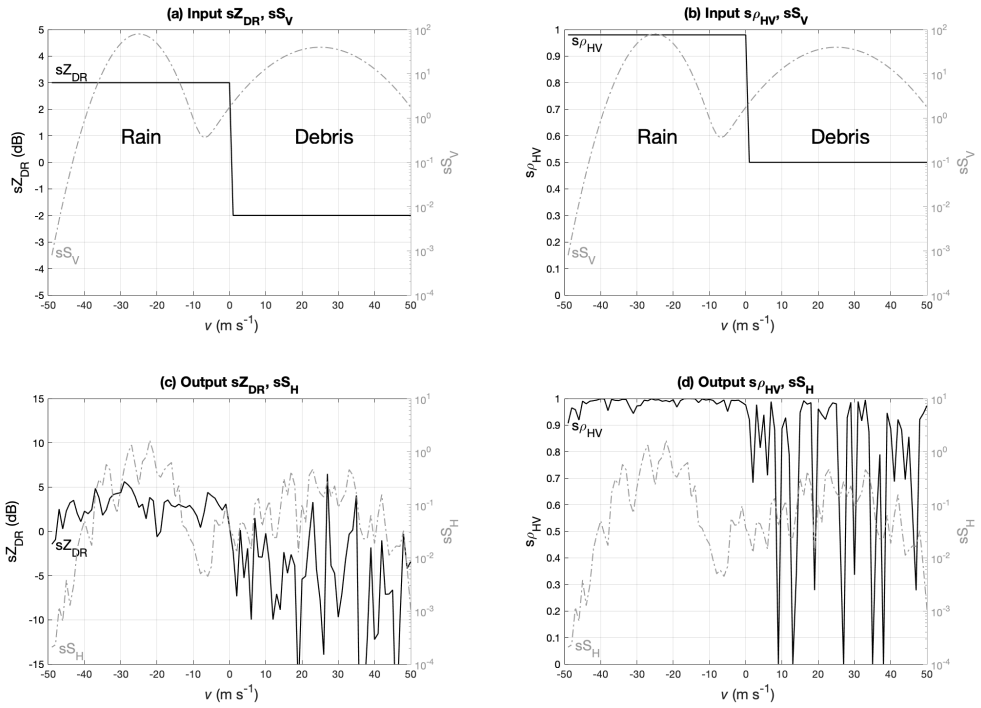

Figure 3.7: Emulator input spectra (a) sZ_{DR} and (b) $s\rho_{HV}$, both shown with the input PSD sS_V (dashed gray); and the resulting output spectra (c) $s\hat{Z}_{DR}$ and (d) $s\hat{\rho}_{HV}$ obtained using the bootstrap estimation method with the emulated time series data, co-plotted with the corresponding PSD estimate $s\hat{S}_H$ (dashed gray).

Chapter 4

Relating Velocity Bias to Debris Characteristics

4.1 Bias Quantification Methods

To fully characterize the effects of debris on radar observations of tornadic wind fields, we consider not only errors in the Doppler velocity itself, but also errors in retrieved three-dimensional velocity fields. Using three-dimensional wind retrievals in this analysis allows us to characterize the influences of debris on each individual velocity component, enabling us to more fully understand how individual debris processes contribute to measured velocity errors. These objectives are accomplished through the calculation of two different measures of velocity: Δv to estimate Doppler velocity bias on a common metric of tornado intensity, and single-Doppler axisymmetric wind retrievals to estimate bias for individual velocity components. To evaluate the effects of debris presence, these calculations are performed for both rain and realistic simulations so that quantitative comparisons between simulations with and without debris can be made.

Δv is a gate-to-gate velocity difference calculated for a plan-position indicator (PPI) radar scan, and is defined as

$$\Delta v = v_{max,out} - v_{min,in}, \tag{4.1}$$

where $v_{max,out}$ and $v_{min,in}$ are the maximum outbound (positive) and minimum inbound (negative) Doppler velocities from the PPI sector. In radar studies of tornadoes, Δv is often used as a proxy for the maximum rotational velocity v_{rot} of the tornado, where $v_{rot} = \frac{1}{2}\Delta v$. Researchers and operational forecasters alike often use Δv estimates to draw conclusions about tornado intensity, and potentially even tornadic structure if the radar is close enough to the tornado to resolve subvortices. Considering Δv as a function of height is also useful for evaluating tornadic structure, especially in studying kinematic evolution and structure in the lowest levels of a tornado.

The wind retrieval method used in this work is the ground-based velocity track display (GBVTD) method. The GBVTD method is a single-Doppler retrieval technique originally developed by Lee et al. (1999) for wind retrievals in tropical cyclones. The method was later adapted by Dowell et al. (2005) to perform tornadic wind retrievals, and that adapted GBVTD technique is the one used in this work. The Doppler velocity is first converted from a spherical coordinate system (with the origin at the radar) to a cylindrical coordinate system (with the origin at the center of the tornado at the lowest analysis height). The radial and azimuthal velocities u_r and v_t are retrieved through cost function minimization, with the resulting expressions for these wind components given by Eqs. 25–27 in Dowell et al. (2005). The vertical wind component w is then calculated through upward vertical integration of radial mass flux as in Nolan (2013). Finally, azimuthal averages of the retrieved velocities are calculated with respect to the center of the tornadic circulation in order to obtain the axisymmetric tornadic wind field.

In a GBVTD analysis of observational data, the conversion from spherical to cylindrical coordinates would need to account for the tornado's translational speed and direction; however, the SimRadar domain is stationary and always centered on the

tornado, which simplifies the retrieval by eliminating the need to correct for the tornado's movement. The automatic positioning of the domain also serves to simplify the determination of the tornado center by enabling us to simply place the origin of the cylindrical coordinate system at the center of the domain, rather than manually determining the center of the circulation using perturbation pressure or wind fields directly from the LES. For the horizontal wind retrieval, we use a radial increment of 30 m to match the range resolution of the SimRadar data sets. For the vertical integration, the height of each scan is taken to be the beam height at the center of the tornado since the simulated sectors have small radial depth, so the change in beam height across the domain is also small.

Given that lofted debris causes distinctive polarimetric signatures in radar data as well as erroneous Doppler velocity measurements, we also sought to identify relationships between the magnitude of velocity error and corresponding values of Z_H, Z_{DR}, and ρ_{HV}. To directly calculate the velocity bias, Doppler velocities from a rain simulation are subtracted from the Doppler velocities of a corresponding realistic simulation such that

$$v_{bias}(r, \phi) = v_{realistic}(r, \phi) - v_{rain}(r, \phi), \tag{4.2}$$

where r and ϕ are the range and azimuthal angle, respectively, of a given radar gate. By performing this calculation for every gate in a PPI sector, the full velocity error field for the sector is obtained. The velocity bias fields are then compared to the polarimetric fields from the realistic simulation in the same gate-to-gate manner—i.e., the velocity bias at a given radar gate is "paired" with the Z_H, Z_{DR}, and ρ_{HV} values at the same gate.

Snyder and Bluestein (2014) suggested that another impact of tornadic debris on Doppler velocity measurements is large differential velocity, or considerable differences

in velocity estimates from the H and V channels, due to complex debris scattering and reduced ρ_{HV}. Therefore, we chose to also correlate velocity bias with differential velocity, given by

$$v_D(r, \phi) = v_H(r, \phi) - v_V(r, \phi), \tag{4.3}$$

where v_H and v_V are the velocity estimates from the H and V channels, respectively. In the same gate-to-gate manner as Z_H, Z_{DR}, and ρ_{HV}, velocity bias magnitude is compared with v_D magnitude to evaluate whether v_D could be a useful predictor of velocity bias. The advantage of using v_D to predict velocity bias magnitude is that v_D can be measured from observations, while velocity bias cannot.

This analysis is performed with two primary objectives in mind. The first objective is to determine whether relationships between velocity bias and bulk polarimetric variables exist such that velocity bias could be modeled as a function of Z_H, Z_{DR}, and ρ_{HV}. The second objective is to determine whether any useful correlation exists between v_D and velocity in order to evaluate the potential utility of using v_D as a proxy quantity to estimate velocity bias. The scope of this particular work is limited to qualitative evaluation of the relationships between velocity bias and polarimetric characteristics of a resolution volume, but in the future may be extended to include quantitative correlation analysis.

4.2 Relationship to Debris Size and Concentration

The overarching hypothesis of this chapter is that there are systematic quantitative relationships between the physical characteristics of lofted debris and the resulting debris-induced errors in Doppler velocity measurements. In this thesis, we focus primarily on how the magnitudes of velocity measurement errors are influenced by the size of lofted debris particles and the overall amount of debris lofted within the domain.

We hypothesize that both debris size and debris concentration are positively correlated with velocity bias magnitude—that is, velocity error magnitude should increase as debris size increases, and likewise for increasing debris concentration. We also evaluate these relationships as functions of elevation angle and radial distance from the center of the tornado.

Our first hypothesis, which is one that has been proposed in past work such as Dowell et al. (2005), is that larger debris should result in velocity measurement errors of greater magnitude. The physical basis for this hypothesis follows from the fact that the amount of backscattered signal power from a target increases exponentially with the RCS of the target, which is largely determined by its size. Because tornadic debris is often several orders of magnitude larger in size than a typical rain drop, an individual piece of debris will return much more signal power to the radar than a rain drop such that the PSD is likely to be dominated by debris contributions, although this is wavelength-dependent as shown in Bodine et al. (2016a). The Doppler velocity of a radar resolution volume is estimated as a power-weighted average, meaning that velocity measurements are skewed toward the frequency at which the largest amount of signal power is returned—in a tornado, this means that measured Doppler velocities are skewed toward the dominant debris velocity and away from the dominant rain velocity. As debris size increases, the degree to which the PSD is dominated by debris contributions also increases, further skewing the power-weighted mean velocity away from rain motion and toward debris motion. Large debris is also likely to deviate more from the ambient wind speed than small debris, creating a greater spectral distance between rain and debris contributions to the PSD. In this manner, the magnitude of Doppler velocity errors should be correlated with the size of lofted debris.

Our second hypothesis is that higher number concentrations of debris should result in larger velocity measurement errors. This hypothesis has a similar physical basis

as the first hypothesis regarding debris size, in that the magnitude of velocity error is driven by the degree to which a PSD is dominated by debris contributions. If a tornado lofts a large amount of debris, a higher proportion of the total returned signal power will be from debris contributions due to the overall larger number of debris-like scatterers. From a radar perspective, increased debris size and increased debris concentration both lead to the same outcome: an increase in the total surface area of debris particles within the resolution volume. As the total debris surface area increases relative to the total rain surface area, whether by increasing the amount of debris pieces or the size of debris particles, the PSD becomes increasingly dominated by debris motion. In observations, correlations between TDS characteristics and qualitative debris information (e.g., damage surveys or photogrammetry) have suggested that ρ_{HV} decreases as more debris are generated or as the debris cloud becomes larger and more opaque (Bodine et al., 2013; Wakimoto et al., 2020). Thus, we hypothesize that there should be a correlation between the magnitude of Doppler velocity errors and the number concentration of lofted debris.

4.2.1 Bias in Δv

As explained earlier in this chapter, Δv is often taken as a proxy for the maximum rotational (azimuthal) velocity of the tornadic wind field. Therefore, evaluating the correlation between debris characteristics and Δv may provide insight into how the presence of lofted debris can introduce bias and inaccuracy into radar-based estimates of tornado intensity. To evaluate the influence of debris on the radar-measured rotational intensity of tornadoes, we compare vertical profiles of Δv from realistic simulations containing various types and sizes of debris to a control Δv profile obtained from the volume scan of rain simulations. As an example, Fig. 4.1 displays profiles of Δv from simulations with debris type 1, or leaves. In the top panel (a), the control vertical

profile of Δv from the rain simulation volume is denoted by a solid red line, while the black lines denote the target Δv profiles from realistic simulations containing varying concentrations of leaves. The bottom panel (b) shows profiles of Δv bias, which is calculated by subtracting the red rain profile from each of the black realistic profiles in (a) as

$$\Delta v_{bias} = \Delta v_{realistic} - \Delta v_{rain}. \tag{4.4}$$

The vertical profile of Δv_{rain} remains constant across all of these analyses because only one set of rain simulations is produced for any given LES model run, and all of the data used in this thesis were generated using the same LES wind field in SimRadar. At the lowest elevation angle of 0.5°, Fig. 4.1a shows a near-surface Δv_{rain} value of approximately 166 m s^{-1}. Moving upward from the surface, Δv_{rain} increases with height through a shallow layer until it reaches a maximum magnitude of 196 m s^{-1} at 1.5°. The beam height at the center of the sector for an elevation angle of 1.5° is approximately 55 m, which is thus taken as the ground-relative height of maximum tornado intensity. Above this elevation, Δv_{rain} steadily decreases until 4.0° in elevation, at which point Δv_{rain} becomes nearly constant with height with a magnitude of approximately 120 m s^{-1}. The rain profile resembles a maximum in azimuthal velocity typically seen in roughly the lowest 50 m in large-eddy simulations of tornadoes. Radar observations of tornadoes have shown a variety of different wind profile structures with maxima at the surface (Bluestein et al., 2004; Kosiba and Wurman, 2013) and other trends of near-surface winds increasing, decreasing, or staying approximately constant with height (Kosiba and Wurman, 2010).

The Δv profiles in Fig. 4.1 are from simulations populated with leaves (debris type 1). From the RCS dimensions listed in Table 3.1, it is clear that the leaf models are the smallest debris for which RCS scattering data have been produced in HFSS.

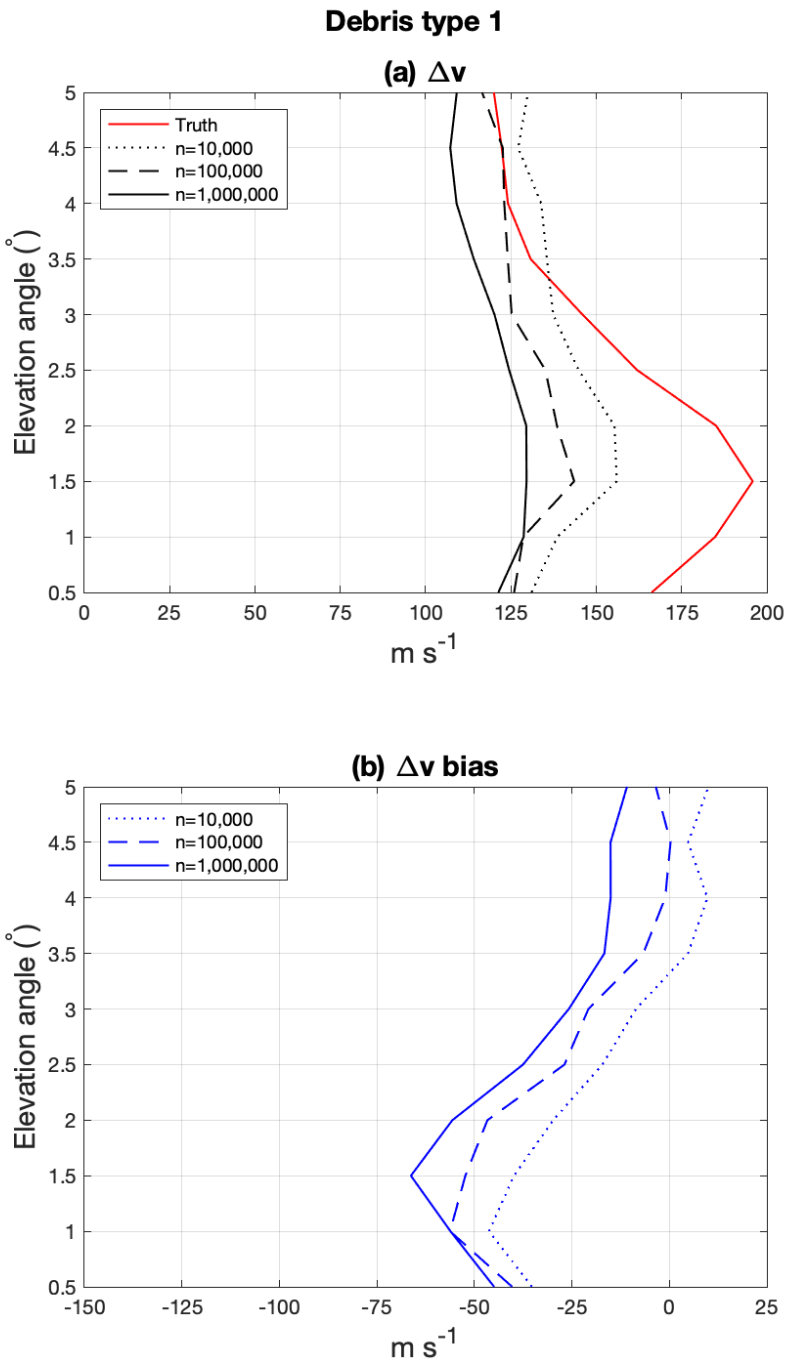

Figure 4.1: Vertical profiles of (a) Δv and (b) Δv bias as a function of elevation angle for SimRadar simulations with varying concentrations of leaves (debris type 1).

Therefore, we expect based on our first hypothesis that these leaf simulations should have the lowest velocity error magnitudes in comparison to other realistic simulations containing larger debris types. These leaf simulations have near-surface Δv values ranging between 121–131 m s^{-1}, depending on the concentration of debris. These profiles show extremely weak Δv maxima at an elevation of 1.5°—the same vertical level as the much stronger Δv maximum in the truth profile. This relative weakening of the Δv maximum in the leaf profiles implies that inferences from Doppler velocity data about changes in tornado intensity with height are detrimentally affected by debris centrifuging bias. Additionally, elevations between 1.0°–1.5° are also where Δv bias magnitude is maximized (Fig. 4.1b), ranging between –46 m s^{-1} for low debris concentration ($n = 10,000$) to –66 m s^{-1} for high debris concentration ($n = 1,000,000$). Above 4.0°, the Δv bias profiles for all debris concentrations become approximately uniform with height. These observations suggest that stronger wind speeds may suffer from greater debris-related bias.

Fig. 4.2 contains Δv profiles for simulations with small wood boards (debris type 3), which are taken as a medium-sized debris model with respect to its dimensions in Table 3.1. In contrast with the truth profile, which displays a clear level of maximum rotational intensity, the small wood board Δv profiles show instead minimum Δv values of 78, 66, and 75 m s^{-1} near the surface for the low, medium, and high debris concentrations, respectively. For all three concentrations, Δv increases between 0.5° until approximately 1.5°, above which Δv becomes roughly constant throughout the remainder of the profile. Below 1.5° in elevation, the Δv bias for the small wood boards (Fig. 4.2b) ranges between –90 m s^{-1} and –110 m s^{-1}, with a weak maximum in bias magnitude near 1.5° in the two higher concentrations. Above 1.5°, the magnitude of Δv bias decreases steadily until around 4.0° in elevation, where the Δv bias starts to become nearly constant with height—similarly to the leaf profiles in Fig. 4.1. Also

similarly, the magnitude of bias in Δv is substantially larger at low elevations than at higher tilts, but this pattern is significantly more pronounced in the small wood board profiles. While the leaf profiles of Δv show considerable damping of the near-surface maximum, the overall qualitative structure is preserved. In the wood board profiles, however, even qualitative interpretations of tornado intensity are incorrect, as the wind speed maximum at 1.5° is completely masked.

Vertical profiles of Δv from simulations with larger wood boards (debris type 4; Table 3.1) are shown in Fig. 4.3. Similarly to the smaller wood boards in Fig. 4.2, the large wood board profiles show clear near-surface minima in Δv, with magnitudes ranging between 39–58 m s^{-1}—the profiles for all three debris concentrations underestimate the near-surface Δv by more than 100 m s^{-1} compared to the truth profile. Like the smaller wood boards, the magnitude of Δv increases steadily between the 0.5–2.0° tilts, above which Δv becomes nearly constant with height. Unlike the smaller debris types, however, the maximum magnitude of Δv bias does not occur at the height of maximum truth Δv, but close to the surface (Fig. 4.3b). Above the lowest tilt, Δv bias magnitude decreases at varying rates throughout the depth of the profile. The severity of Δv bias for all three debris concentrations is largest in the low levels, with near-surface Δv bias at 0.5° being nearly 100 m s^{-1} greater in magnitude than the Δv bias at higher tilts like 5.0°. Of the three types of debris, the severity of low-level Δv bias is most pronounced for the larger wood board simulations (Fig. 4.3b) and least pronounced for the leaf simulations (Fig. 4.1b).

Figs. 4.1–4.3 provide comparisons of both Δv magnitude and Δv bias between multiple concentrations of each debris type. For all three debris types, Δv generally decreases as debris concentration increases throughout the column, indicating that higher debris concentrations tend to correspond to reductions in measured Doppler

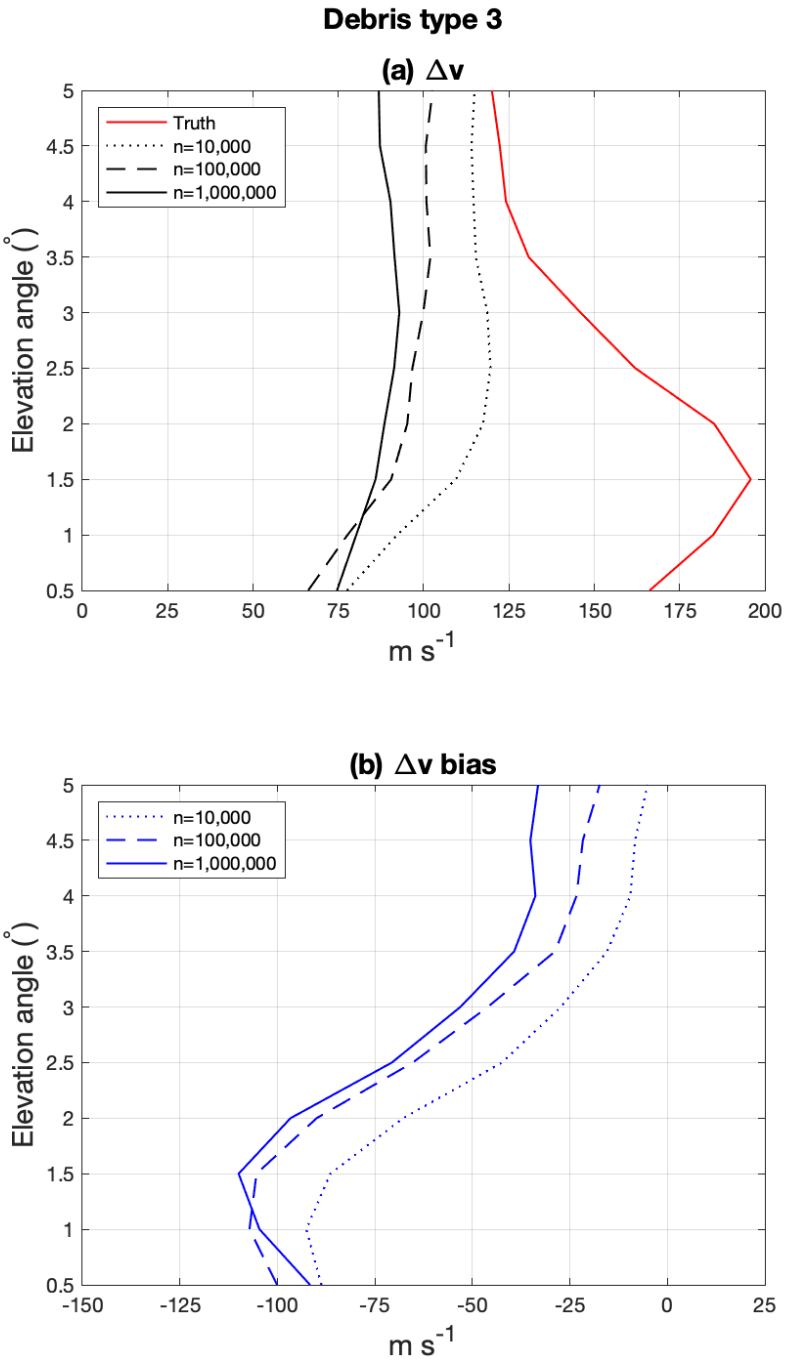

Figure 4.2: As in Fig. 4.1, but for small wood boards (debris type 3).

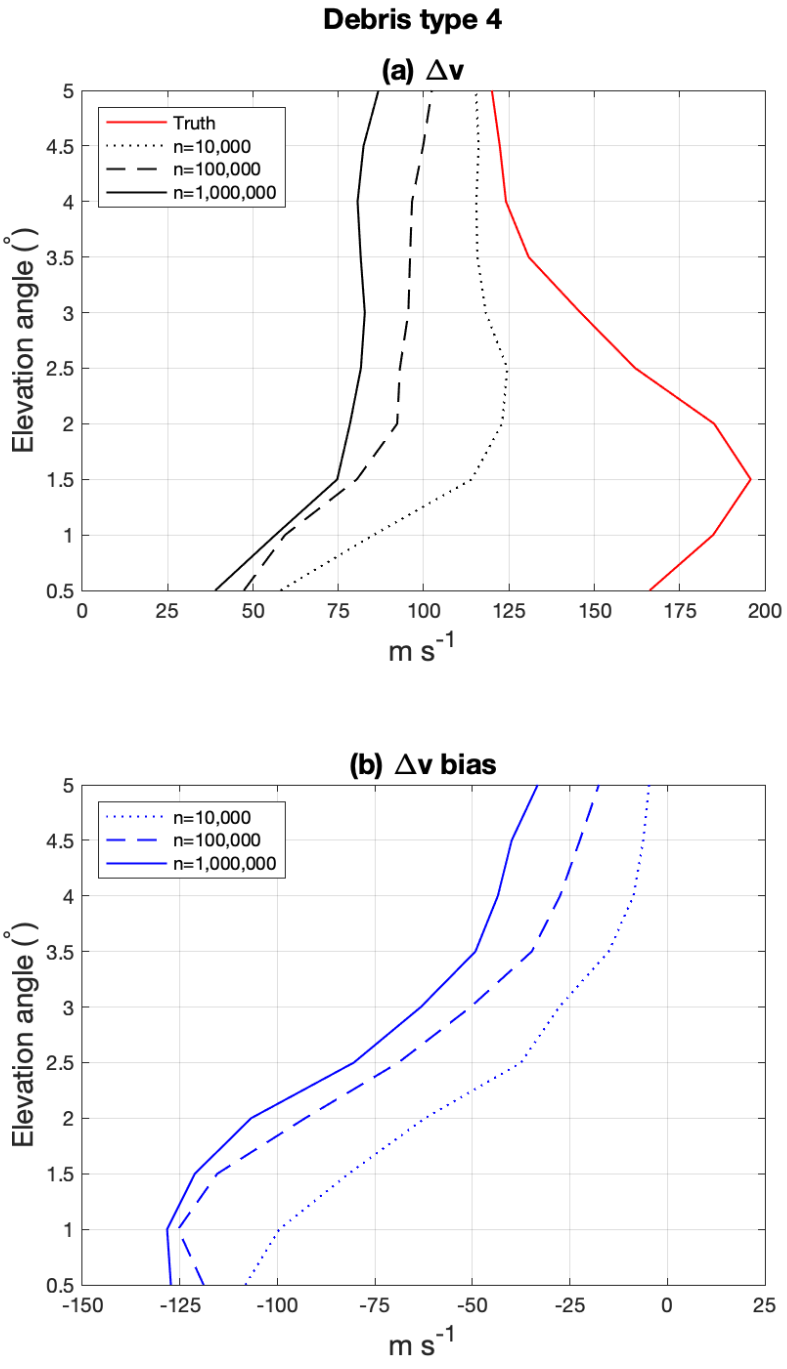

Figure 4.3: As in Fig. 4.1, but for larger wood boards (debris type 4).

velocity. Paradoxically, the reduction of Δv with increasing overall debris concentration tends to be least pronounced in the lowest levels, despite the fact that the majority of lofted debris tends to accumulate near the surface rather than being lifted to higher elevations. A possible explanation for this deviation is that perhaps there is a threshold to the influence of debris concentration on Doppler velocity bias, above which any further increases in debris concentration no longer induce a significant response in the velocity bias—i.e., the Doppler velocity bias reaches some intrinsic limit at this hypothetical concentration where the radar signal becomes saturated by debris. This could explain why an exponential increase in debris concentration only results in a slight increase in Δv bias magnitude at low levels. At higher tilts (e.g., above roughly 1.5°), the differences in velocity bias between low and high debris concentrations become more clear.

A more effective way to examine the relationship between Doppler velocity bias and debris concentration could be to instead consider Δv bias as a function of elevation angle, rather than directly as a function of concentration. As has been shown in prior work (see Chapter 2.1.2), debris particles tend to have the highest concentration near the surface due to their short residence time within the tornado—especially for larger debris, which tends to be quickly centrifuged out of the updraft. Therefore, the change in debris concentration between lower and higher tilts of a single simulation is likely more significant than the same-tilt difference in concentration between two simulations. This is reflected in one of the behaviors discussed above, wherein the magnitude of Δv bias for all three debris types is maximized in the lowest few elevation angles. Furthermore, the magnitude of the change in Δv bias with height—or the severity of low-level Doppler velocity bias—increases with increasing debris size, from leaves to small wood boards to larger wood boards. Thus, the comparisons between these Δv analyses support our main hypotheses that an increase in either debris size or debris

concentration results in increased Doppler velocity bias. However, it remains unclear whether the primary driver of centrifuging bias is debris concentration or size.

On the contrary, the aforementioned patterns in Δv as a function of elevation suggest that the velocity bias effects of debris size and debris concentration are coupled—at least in part—which has varying implications for the relative influences of debris size and concentration on Doppler velocity bias at high and low elevations. Figs. 4.1b, 4.2b, and 4.3b all show that at higher tilts ($> 4.0°$), there is little change in the magnitude of Δv bias between the three sizes of debris. While wood boards should generate greater velocity bias than leaves because of their larger size, this also leads them to fall out of the tornado before being lofted to higher altitudes. At higher elevations, therefore, small debris such as leaves are most likely to be the dominant scatterers. For the same reason, larger debris such as wood boards are more likely to be the dominant scatterers at low elevations than smaller debris, relative to their original concentrations. In a real tornado, the overall concentration of large debris such as wood boards is likely much lower than that of smaller debris such as leaves and soil particles.

4.2.2 Bias in GBVTD Winds

As discussed in Dowell et al. (2005) and Nolan (2013) and verified by numerous observational studies, lofted debris produces unique systematic biases in three-dimensional winds retrieved from Doppler velocity fields. A key difference between these previous studies and the present one, however, is that this work involves the simulation of radar signals for a realistic distribution of background hydrometeor scatterers superimposed with the varying debris fields. The GBVTD method is applied to Doppler velocity fields from various SimRadar simulations to retrieve axisymmetric averages of the tornado-relative radial, azimuthal, and vertical winds. In looking at each component separately, we seek to identify the influences of specific debris processes and determine

the relationships between velocity error characteristics and the physical characteristics of debris.

As with Δv, we again seek to examine the errors and systematic biases in the GBVTD winds as a function of both debris size and concentration. Fig. 4.4 shows the axisymmetric GBVTD winds and bias in each velocity component for a realistic case SimRadar simulation with 10,000 leaves. Based on our hypotheses about the influence of debris characteristics on Doppler velocity measurements, the retrieved winds shown in Fig. 4.4 should suffer from the least velocity bias, as this simulation represents the smallest debris at the lowest concentration.

Visually, the realistic case (Fig. 4.4a–c) and truth (Fig. 4.4d–f) GBVTD velocities show similar characteristics. The radial winds have an inflow maximum in the lowest 50–100 m and an overlying region of weak outflow above 100 m near the tornado axis, with weak to moderate inflow throughout the rest of the domain. The azimuthal winds show the RMW at approximately 100–200 m from the center of the tornado and shifting radially outward with height. Finally, the vertical winds show the strong central updraft generally contained within 250–300 m from the central axis.

However, the GBVTD wind errors (Fig. 4.4g–i) shows that small debris at low concentrations still generate bias in three-dimensional velocity fields. Throughout almost the entire domain, the radial winds are weakly positively biased (Fig. 4.4g), indicating that the presence of debris is causing general anomalous weakening of the tornadic inflow. The magnitude of radial bias is slightly enhanced in the lowest 100 m, within 200 m of the tornado's axis. Conversely, the azimuthal winds throughout the domain are weakly negatively biased (Fig. 4.4h), particularly in the lowest 50 m near the center of the tornado. In the vertical winds, the central updraft strength suffers considerable underestimation (Fig. 4.4i), with the realistic case GBVTD vertical winds (Fig. 4.4c)

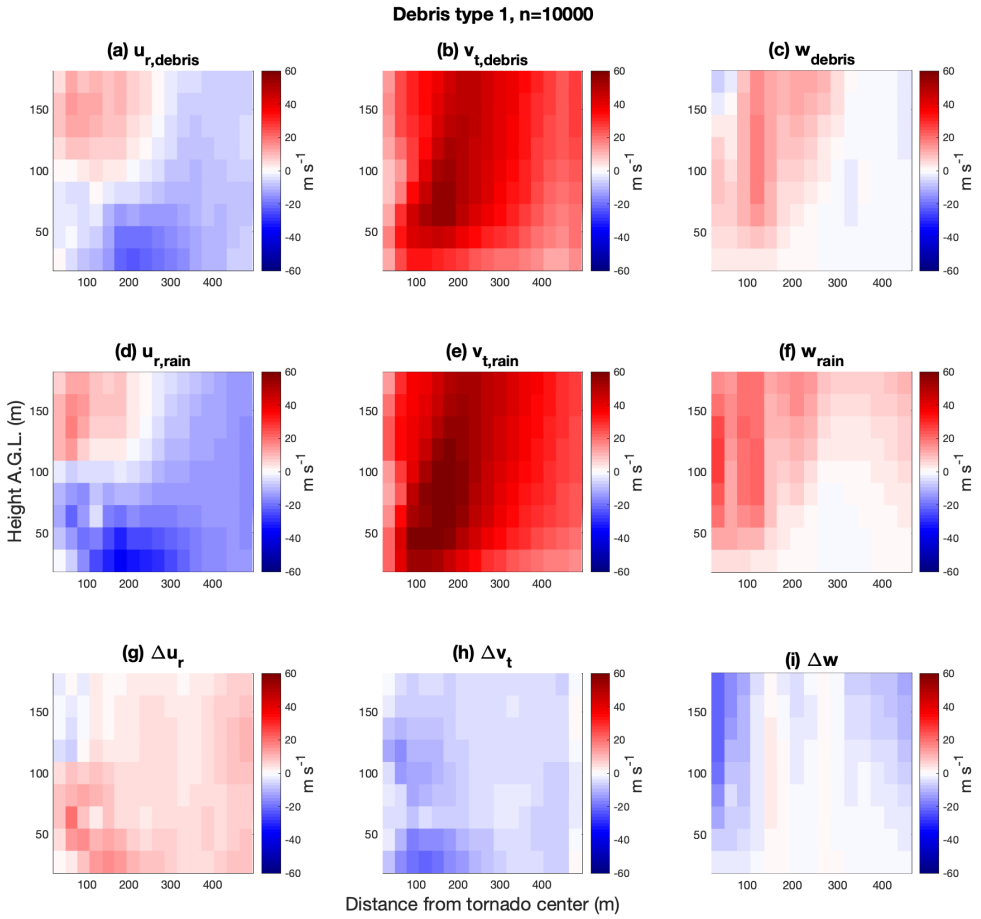

Figure 4.4: GBVTD retrievals of (left)–(right) u_r, v_t, and w axisymmetric winds from a realistic SimRadar simulation containing 10,000 leaves (top), the corresponding rain simulation (middle), and the resulting velocity bias (bottom) obtained by subtracting the rain velocities from the realistic velocities such that (g)=(a)−(d); (h)=(b)−(e); and (i)=(c)−(f). Each panel is an axisymmetric vertical cross-section, with the horizontal and vertical axes representing radial distance from the tornado center and height, respectively. Red shades denote positive velocities, while blue shades denote negative velocities.

falsely showing the beginnings of an axial downdraft—this downdraft does not exist in the truth wind field, which consists of a single-celled vortex. Additionally, the wider updraft throughout the domain above the tornado boundary layer is underestimated or masked completely in the realistic case winds, though there is the possibility that the truth simulation may also be biased itself due to hydrometeor centrifuging.

Following the previous analysis, Fig. 4.5 shows the GBVTD winds from a simulation with 100,000 leaves, representing small debris at a medium concentration; with this increase in concentration, the differences between the realistic case velocities (Fig. 4.5a–c) and the truth velocities (Fig. 4.5d–f) become considerably more severe. The weak radial inflow present in the outer radii of the domain in the truth case is replaced with weak outflow (Fig. 4.5g). The near-surface inflow maximum located between 100–300 m from the tornado center is still present in the realistic case, but is weakened. The largest positive radial bias in this simulation is near the outer edges of the domain throughout the column. Similarly to the 10,000 leaves case, the azimuthal wind bias in the 100,000 leaves case is weakly negative throughout the domain (Fig. 4.5h), with a near-surface minimum at a radius of 100 m. The retrieved vertical winds show considerable negative bias throughout the domain (Fig. 4.5i), indicating significant underestimation of the strength of the tornado's central updraft. Furthermore, Fig. 4.5c shows a downdraft outside of the 200–250 m radius, where the truth winds in Fig. 4.5f still show weak upward motion.

Finally, retrieved velocities from a simulation with 1,000,000 leaves—small debris at a high concentration—are shown in Fig. 4.6. In general, the simulations with 100,000 leaves and 1,000,000 leaves (shown in Figs. 4.5 and 4.6, respectively) demonstrate the same patterns in both the retrieved winds and the bias, but with greater severity for the high concentration. The realistic case radial winds show strong positive bias

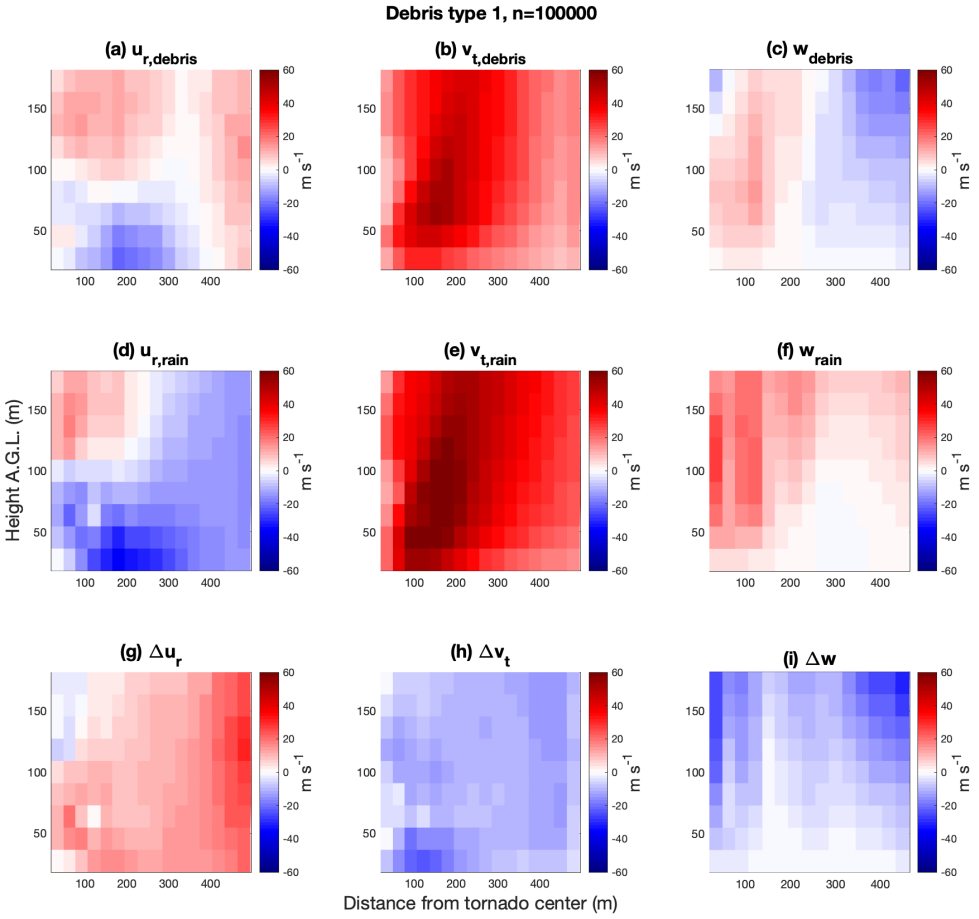

Figure 4.5: As in Fig. 4.4, but for 100,000 leaves.

through the outer half of the domain (Fig. 4.6g), with radial velocity errors reaching 60 m s^{-1} in magnitude near radii between 400–500 m.

Meanwhile, both the azimuthal and vertical winds show considerable negative bias throughout most of the domain (Fig. 4.6h–i). The largest bias in both azimuthal and vertical winds occurs in the outer portion of the domain, past the RMW, with azimuthal wind underestimations of roughly 30 m s^{-1} and vertical wind underestimations approaching 40–50 m s^{-1}. In the realistic case azimuthal winds (Fig. 4.6b), the velocities in the outer annulus are extremely low, even approaching 0 m s^{-1} at radii beyond 400 m from the vortex center. In the vertical winds, the intensity of the central updraft is severely underestimated, while a strong erroneous downdraft is retrieved beyond 200 m from the vortex center (Fig. 4.6c)—a location where there should be weakly positive vertical motion according to the truth wind field.

As in the Δv analyses, we use leaves to represent small debris and wood boards to represent larger debris in order to evaluate the influence of debris size on velocity bias, though only the smaller wood boards (debris type 3) are included in the GBVTD analyses for simplicity. Fig. 4.7 shows the GBVTD winds for a simulation with 10,000 wood boards. From these plots, it can be seen that small concentrations of larger debris create large bias in all three axisymmetric velocity components. In the lowest levels at heights below 100 m, the radial inflow shows considerable positive bias, with Fig. 4.7a showing no inflow at all within 200 m of the tornado center—this is consistent with radar observations of near-surface radial divergence where inflow is expected. The azimuthal velocities are also significantly weakened near the surface and within 200 m of the vortex core (Fig. 4.7b,h), with azimuthal bias approaching –50 m s^{-1}. Finally, while the truth vertical velocity shows pure updraft within the vortex core (Fig. 4.7f), the realistic case vertical velocity retrieval indicates a narrow axial downdraft

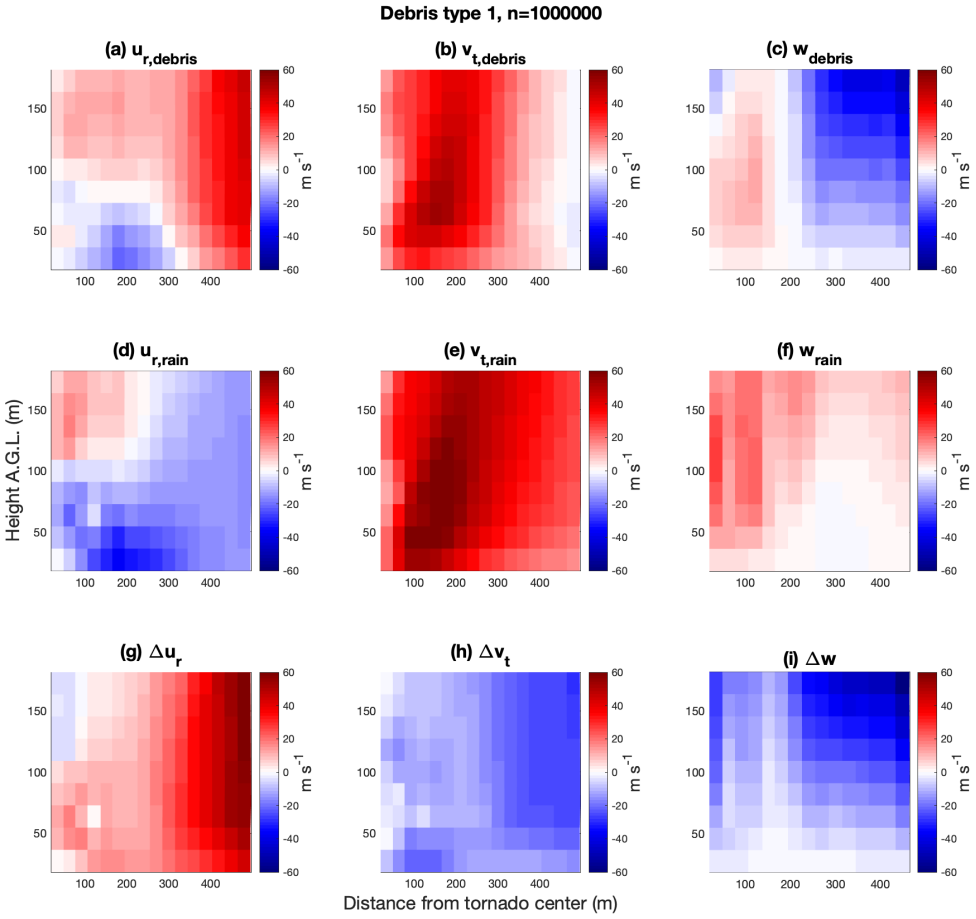

Figure 4.6: As in Fig. 4.4, but for 1,000,000 leaves.

beginning to develop above 100 m (Fig. 4.7c). This is a consequence of the deviant outward motion produced by strong centrifuging within the tornado's core.

Continuing with intercomparisons across varying concentrations of debris, Fig. 4.8 shows the GBVTD winds for a simulation containing a medium concentration of 100,000 wood boards. Here, the errors in the retrieved velocities start to become quite large. Nearly no radial inflow at all is shown in Fig. 4.8a; instead, weak outflow is present throughout the majority of the domain. As in the 10,000 wood board case, the positive radial bias is strongest below 100 m (Fig. 4.8g). The azimuthal velocities are weakened considerably, with large azimuthal bias throughout almost the entire domain (Fig. 4.8h), especially within 300 m of the tornado core and at heights below 100 m. The region of largest azimuthal bias is roughly collocated with the RMW in the truth azimuthal winds (Fig. 4.8e). The weak impinging axial downdraft seen in Fig. 4.7c is both stronger and wider with the increased debris concentration (Fig. 4.8c), with little upward motion within the domain.

Finally, the highest concentration of large debris is represented in Fig. 4.9, which shows the GBVTD winds for a simulation with 1,000,000 wood boards. The errors in the retrievals for this case are extremely large throughout almost the entire domain in all three velocity components. The retrieved radial winds in Fig. 4.9a show relatively strong outflow across most of the domain (approximately 30 m s^{-1}), with the exception of zero near-surface radial velocity close to the tornado core. Meanwhile, the azimuthal velocities are severely weakened, with wind speeds below 20 m s^{-1} throughout the entirety of the domain (Fig. 4.9b) and the most severe azimuthal bias collocated with the RMW in the truth retrieval (Fig. 4.9e,h) similarly to the 100,000 wood board case. Finally, the vertical velocity retrieval shows strong downdraft and no updraft at all throughout the entire domain (Fig. 4.9c).

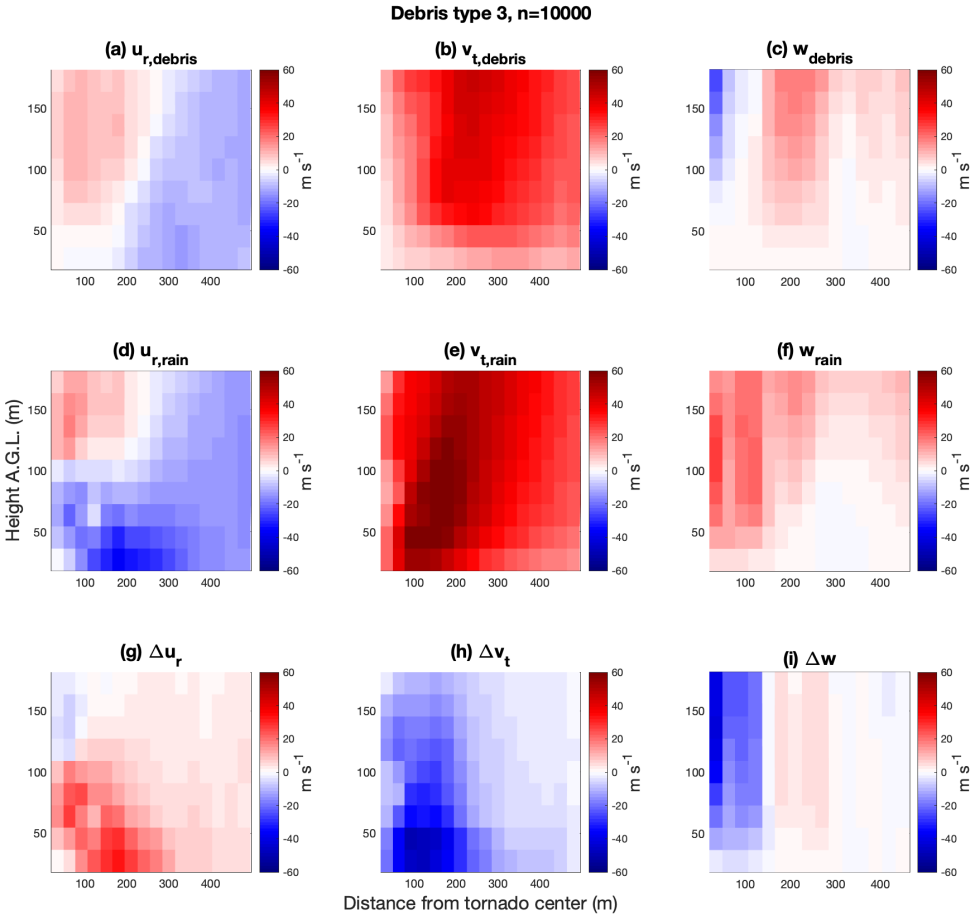

Figure 4.7: As in Fig. 4.4, but for 10,000 wood boards.

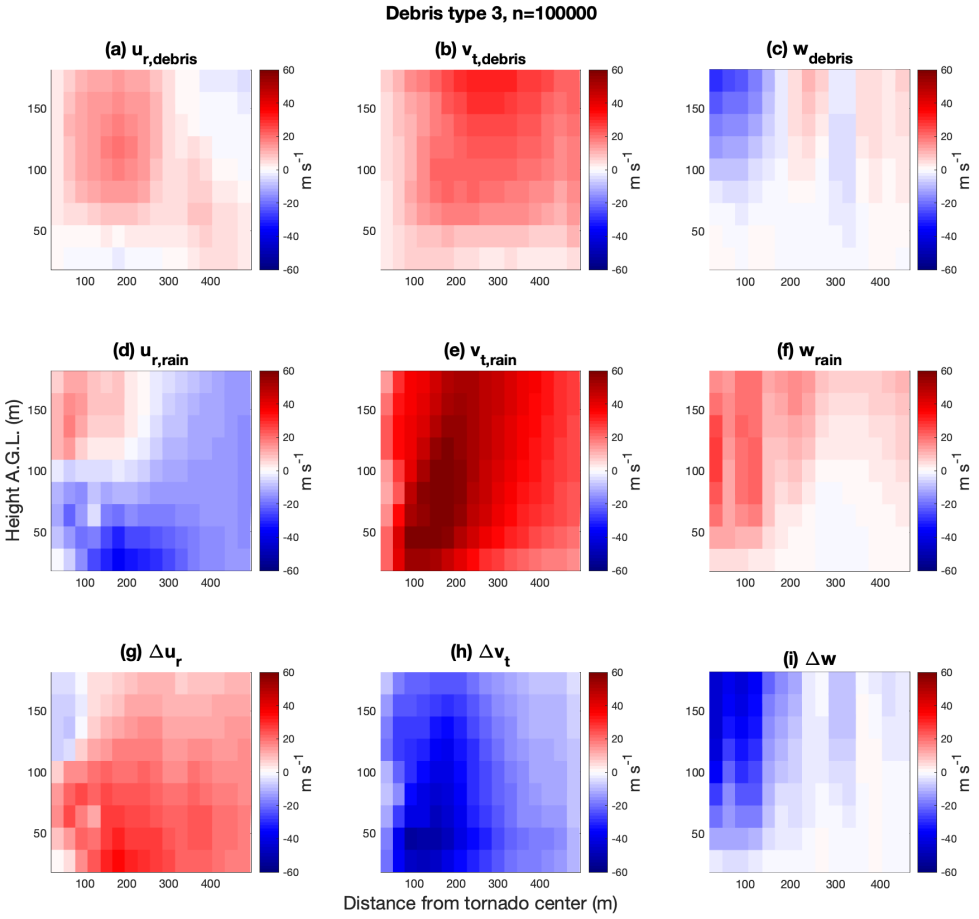

Figure 4.8: As in Fig. 4.4, but for 100,000 wood boards.

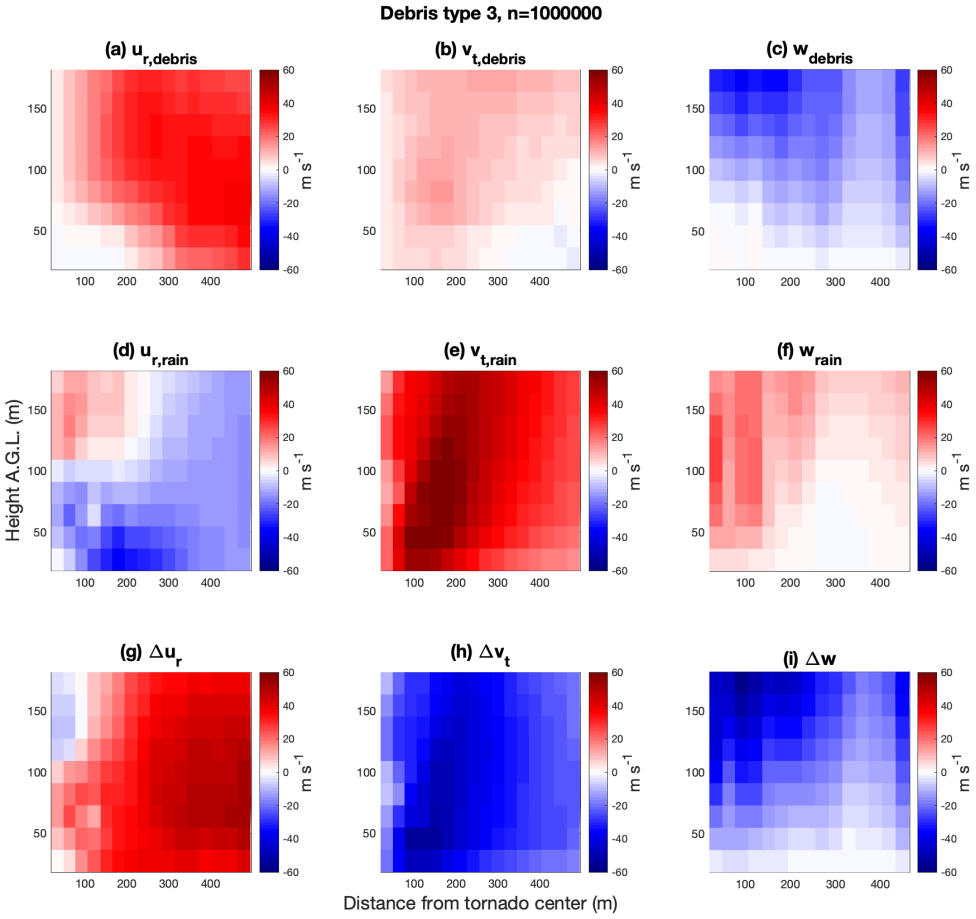

Figure 4.9: As in Fig. 4.4, but for 1,000,000 wood boards.

The GBVTD retrievals for both leaves and wood boards illustrate clearly a relationship between debris concentration and velocity bias magnitude. As the concentration of a given debris type increases, the magnitude of velocity errors increases as well in all three retrieved velocity components. In an extension of conclusions drawn by Dowell et al. (2005) and Nolan (2013) to address the impacts of varying debris concentration, these results show that *increases in debris concentration are associated with weakened low-level radial inflow and anomalous outflow, substantially weakened low-level and maximum azimuthal velocities, and erroneous axial downdraft production.* It is important to note that a concentration of 1,000,000 debris pieces may be physically unrealistic and unlikely to occur in a real tornado, although it is also important to note that only a small subset of the total debris are ultimately lofted to the height of the radar beam in SimRadar. However, for the purposes of illustrating the positive correlation between debris concentration and velocity bias severity, we felt it useful to evaluate the velocity errors associated with a potentially extreme concentration of debris to support the conclusions drawn from more physically realistic concentrations.

In comparing the leaf simulations shown in Figs. 4.4–4.6 to the wood board simulations in Figs. 4.7–4.9, we can also discern a clear correlation between debris size and velocity bias magnitude. At a given concentration, the GBVTD velocity biases seen in the wood board simulations are more severe than the biases in the leaf simulations—the low-level radial inflow is retained in the leaf simulations even as debris concentration increases, but this feature is lost completely in the wood board simulations. The wood board simulations also display greater slowing of the azimuthal winds and a more prominent false axial downdraft in the vertical winds, even at the lowest concentration. Moreover, low-level velocity bias appears to become more significant with increased debris size—that is, larger debris has a stronger effect on low-level velocity

retrievals than smaller debris. This same behavior was observed in the Δv analyses earlier in this chapter.

An additional facet to the GBVTD analyses that is not present in the Δv analyses is the integration of errors associated with velocity retrieval. The 10,000 and 100,000 wood board simulations in Figs. 4.7–4.8 indicate the presence of an axial downdraft at the core of the tornado in the retrieved vertical winds. Without knowledge of the true, unbiased vertical wind field, this pattern would suggest that the tornado is experiencing vortex breakdown and taking on a two-celled structure. However, the true vertical wind field is one-celled, consisting purely of updraft including at the vortex core. The retrieval of an axial downdraft is likely related to the integration of centrifuging errors in the retrieved radial velocities. The vertical wind retrieval in this analysis is computed via upward integration of radial mass flux—since the low-level convergent inflow is weakened or even reversed in the wood board simulation retrievals, the vertical integration responds to the anomalous outward radial mass flux by calculating an erroneous downdraft along the axis of the tornado. Therefore, inferences about tornado structure from radar-derived wind retrievals may be rendered incorrect by debris-induced Doppler velocity bias.

4.3 Moment-Based Velocity Bias Estimation

4.3.1 Relationship to Polarimetric Variables

While understanding the relationships between the physical properties of debris and the resulting induced velocity measurement errors is scientifically valuable, the characteristics of the debris field are unknown in a real situation. Therefore, these relationships are further evaluated in a more operationally relevant manner using observable polarimetric characteristics to predict debris-related velocity bias. We ultimately seek to

quantify these relationships such that polarimetric radar observations can be utilized to answer the following questions: is a given Doppler velocity measurement biased, and to what degree? Because the presence of lofted debris causes distinct polarimetric signatures and velocity errors simultaneously, and because the relative strength of those signatures is modulated by the physical characteristics of debris, we hypothesize that as the values of Z_H, Z_{DR}, and ρ_{HV} become more characteristic of TDSs (e.g., as Z_H increases, or as Z_{DR} or ρ_{HV} decreases), the corresponding velocity errors should increase in magnitude proportionally.

In keeping with this chapter's theme of evaluating the influence of debris size, we first examine the correlations between velocity bias and Z_H, Z_{DR}, and ρ_{HV} for varying concentrations of leaves in Fig. 4.10. All three relationships are complex and nonlinear, but there are still discernible patterns in each relationship that roughly match *a priori* expectations. The correlation between Z_H and velocity bias is somewhat weak, as the distribution of bias magnitudes is centered around 0 m s^{-1} across the full range of Z_H values—except for at the highest concentration of 1,000,000 leaves. However, the *spread* of velocity bias magnitudes increases with increasing Z_H until approximately $Z_H = 50$ dBZ, which does indicate that higher values of Z_H are associated with larger velocity bias. Paradoxically, velocity bias actually decreases with increasing Z_H for values greater than approximately 50 dBZ for the highest concentration.

The polarimetric variables also show complex relationships with velocity bias. Z_{DR} shows a slightly better correlation with velocity bias magnitude than Z_H. For approximately $Z_{DR} > -1$ dB, the distribution of velocity bias values is centered at 0 m s^{-1}, with the spread of bias magnitudes increasing as Z_{DR} decreases—this fits with observations of negative Z_{DR} associated with debris in TDSs. Below $Z_{DR} = -1$ dB, the velocity bias distribution begins to decenter from 0 m s^{-1}, indicating that low

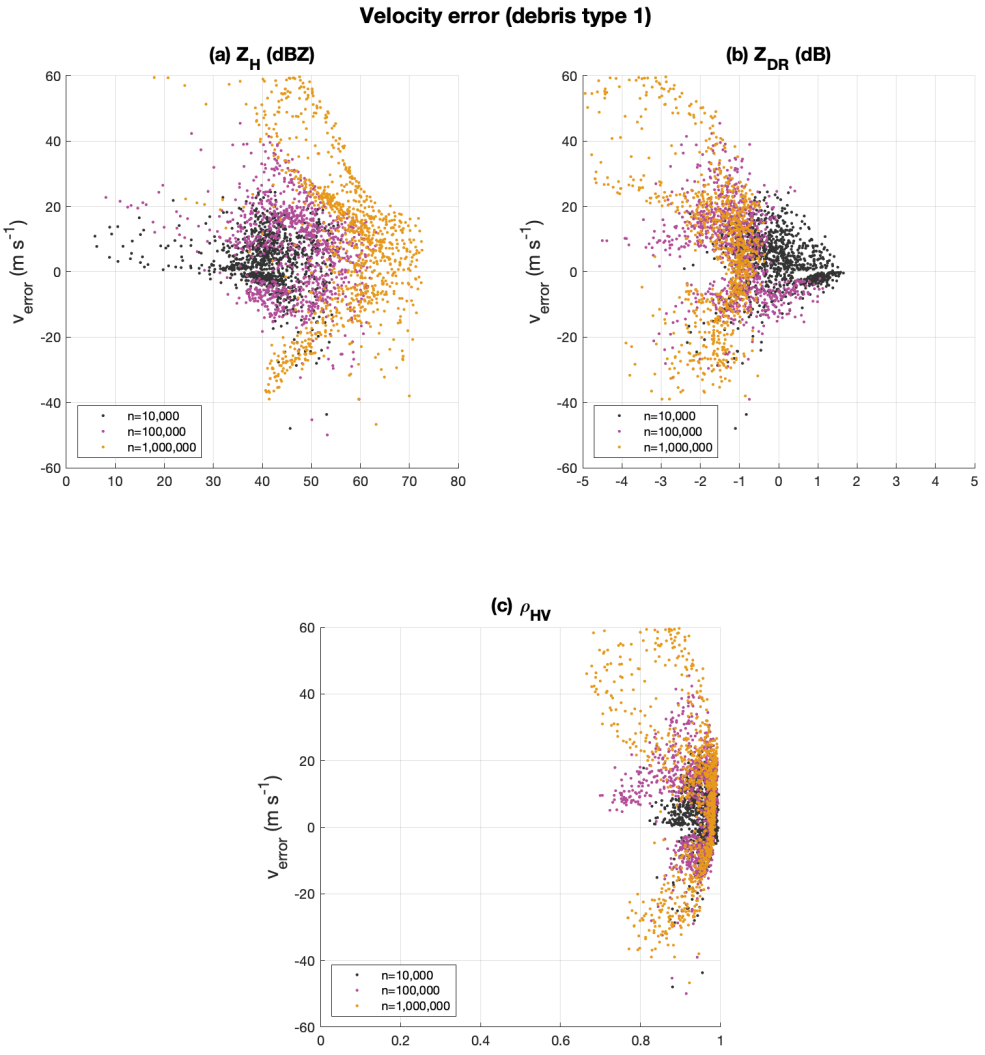

Figure 4.10: Scatter plots of Doppler velocity errors as a function of bulk polarimetric variables (a) Z_H, (b) Z_{DR}, and (c) ρ_{HV} for SimRadar simulations with leaves at concentrations of 10,000 (black), 100,000 (purple), and 1,000,000 (yellow).

and negative values of Z_{DR} are associated with non-zero velocity bias. Velocity bias magnitude and spread continue increasing as Z_{DR} continues to decrease. Finally, the correlation between ρ_{HV} and velocity bias is complicated by the fact that these leaf models have overall large values of ρ_{HV}, as the full range of ρ_{HV} values remains above 0.7. However, the overall trend is similar to that of Z_{DR}, where as ρ_{HV} decreases, the magnitudes and spread of velocity bias both increase.

The relationships between velocity bias and Z_H, Z_{DR}, and ρ_{HV} are considerably different for the wood board debris types, which are significantly larger than the leaves. The relationships with all three polarimetric variables are nearly the same for both the smaller and larger wood boards, shown in Figs. 4.11 and 4.12. Like the leaves, the distribution of velocity bias magnitudes remains approximately centered at 0 m s^{-1} across the full range of Z_H values, but the spread of bias magnitudes increases significantly as Z_H increases above a value of approximately 40 dBZ. Unlike the leaves, however, the bias distribution does remain roughly centered near 0 m s^{-1} across the range of Z_{DR} and ρ_{HV} values. For Z_{DR}, the spread of bias magnitude is also large across the full range of Z_{DR} values. More expectedly, the spread of velocity bias magnitude generally increases as ρ_{HV} decreases—except for the largest concentration of debris, wherein the spread of bias magnitudes is wide and approximately constant across the range of ρ_{HV} values, which are much lower for wood boards compared to leaves. Similar to behaviors discussed earlier in the context of the Δv analyses, there appears to be a debris saturation effect in bulk ρ_{HV}, wherein once the signal is substantially dominated by debris, ρ_{HV} and velocity bias both cease to have a significant response to debris size or concentration.

In all debris types, the relationships between velocity bias and Z_H, Z_{DR}, and ρ_{HV} are highly dependent on debris concentration. Low debris concentrations are associated

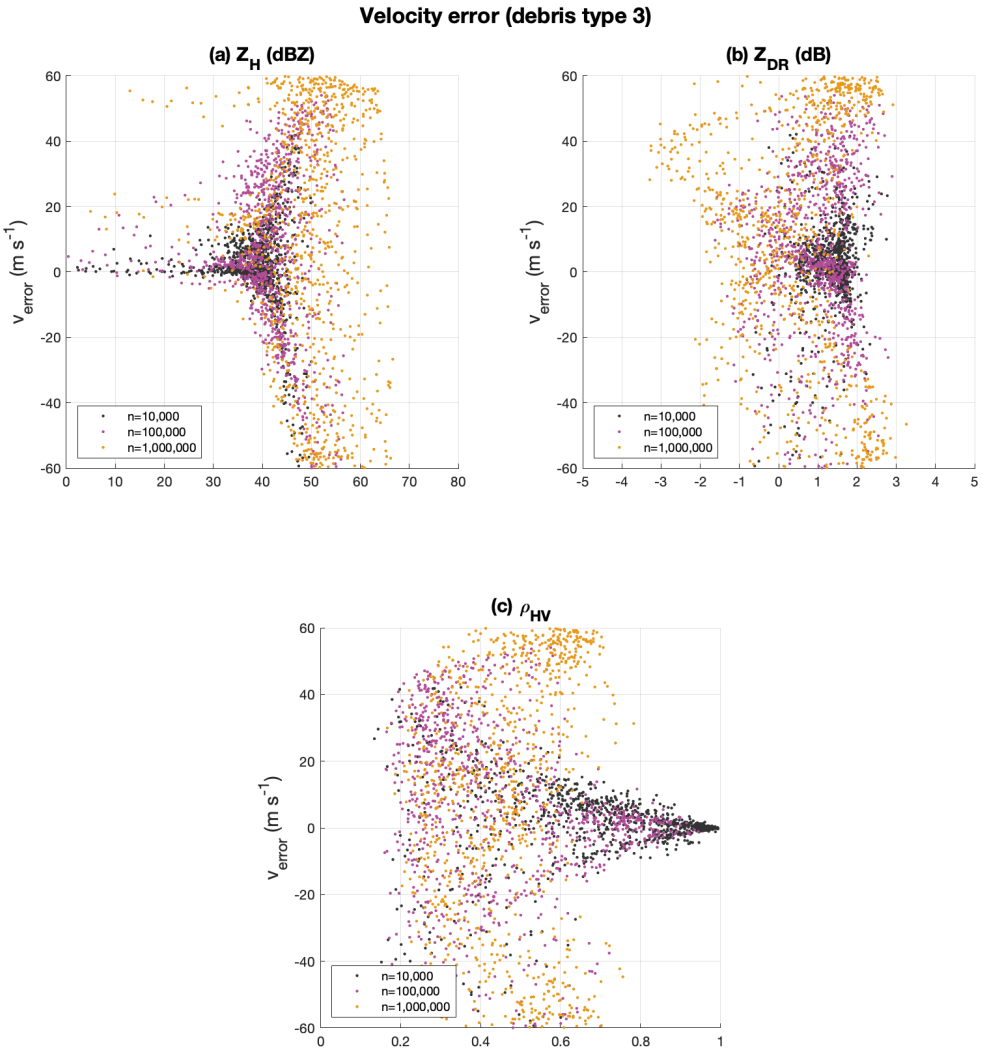

Figure 4.11: As in Fig. 4.10, but for small wood boards (debris type 3).

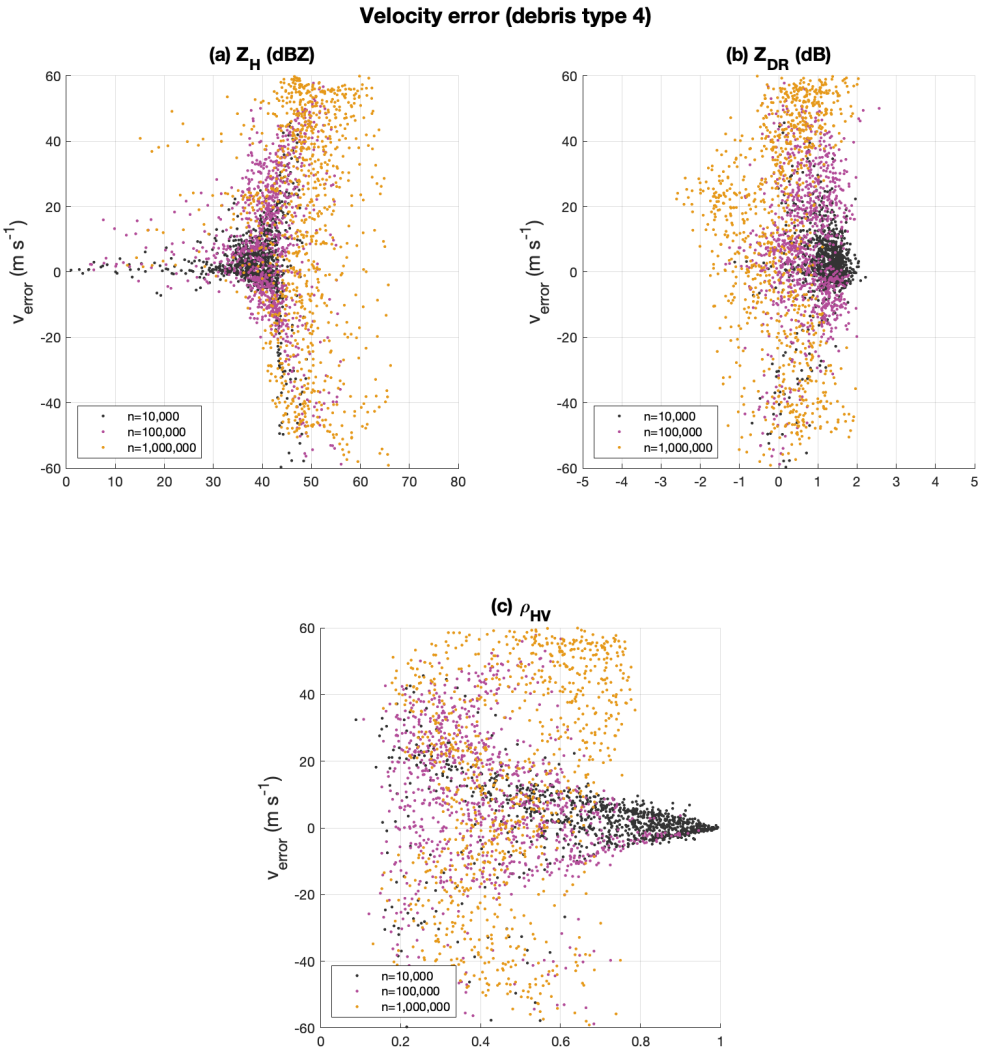

Figure 4.12: As in Fig. 4.10, but for larger wood boards (debris type 4).

with lower magnitude and spread of velocity bias, as well as lower Z_H (< 50 dBZ), higher Z_{DR} (> -1 dB), and higher ρ_{HV}; and vice versa for high debris concentrations. While the range of Z_H and Z_{DR} values is similar between the leaves and the wood boards, the range of ρ_{HV} values varies dramatically between different debris sizes, as ρ_{HV} tends to be quite high for leaves even at high concentrations (Fig. 4.10c), while it reaches much lower values for wood boards (Figs. 4.11c, 4.12c).

Because these relationships are so complex and nonlinear, precise quantitative relationships between velocity bias and polarimetric variables will be difficult to determine. However, a simpler option for using polarimetric variables to estimate velocity bias could be to empirically define threshold values for Z_H, Z_{DR}, and ρ_{HV} based on the range of values for which there is high probability of large velocity bias. Based on the patterns in Figs. 4.10–4.12, potential threshold values for determining the likelihood of large velocity bias at a given radar gate could be: $Z_H > 40$ dBZ, $Z_{DR} < 1$ dB, and $\rho_{HV} < 0.7$–0.8, although as previously discussed, these relationships are complicated by their relatively strong dependence on debris type and concentration.

4.3.2 Relationship to Differential Velocity

Correlating velocity bias with v_D also has attractive potential as a method for estimating Doppler velocity bias from bulk radar measurements (Snyder and Bluestein, 2014). As discussed previously, the relationships between velocity bias and Z_H, Z_{DR}, and ρ_{HV} are highly nonlinear with confounding dependencies on both debris size and concentration, reducing their operational applicability for estimating Doppler velocity bias. Therefore, based on the suggestion by Snyder and Bluestein (2014) that the magnitude of v_D may be related to debris abundance and associated ρ_{HV} values, we sought to determine whether a simpler relationship—more linear, and with less dependence on debris characteristics—might be found between velocity bias and v_D.

To provide both a qualitative and quantitative understanding of this potential relationship, Figs. 4.13–4.15 show scatter plots of Doppler velocity errors as a function of v_D for SimRadar simulations containing varying concentrations of leaves, small wood boards, and larger wood boards, respectively, at an elevation angle of 2.0°. As in Figs. 4.10–4.12, all three simulated debris concentrations are combined in each plot to facilitate easy discernment of any confounding concentration dependence in the main relationship between velocity bias with v_D.

A major qualitative difference between these v_D relationships and the polarimetric relationships discussed previously is that the correlations between velocity bias and v_D are much more linear in nature for all three debris types. Furthermore, there does not appear to be any strong dependence on debris concentration in these relationships other than its influence on the range of bias magnitudes. However, the overall utility of these relationships is low, as there is little variation in v_D across the full range of bias magnitudes. Especially for the wood board simulations in Figs. 4.14 and 4.15, there is no apparent one-to-one correlation between the magnitudes of v_D and velocity bias.

Because these relationships, although weak, are approximately linear in nature, least-squares linear regressions were performed to obtain expressions for velocity bias as a function of v_D for each debris type. The best-fit linear equation for each debris type is annotated on the corresponding figure. Interestingly, the leaf simulations produced the largest values and widest spread of v_D, while the larger wood board simulations produced the narrowest spread and small values of v_D, which is opposite to what one would expect based on prior knowledge about debris scattering and the effects of low ρ_{HV} on signal statistics.

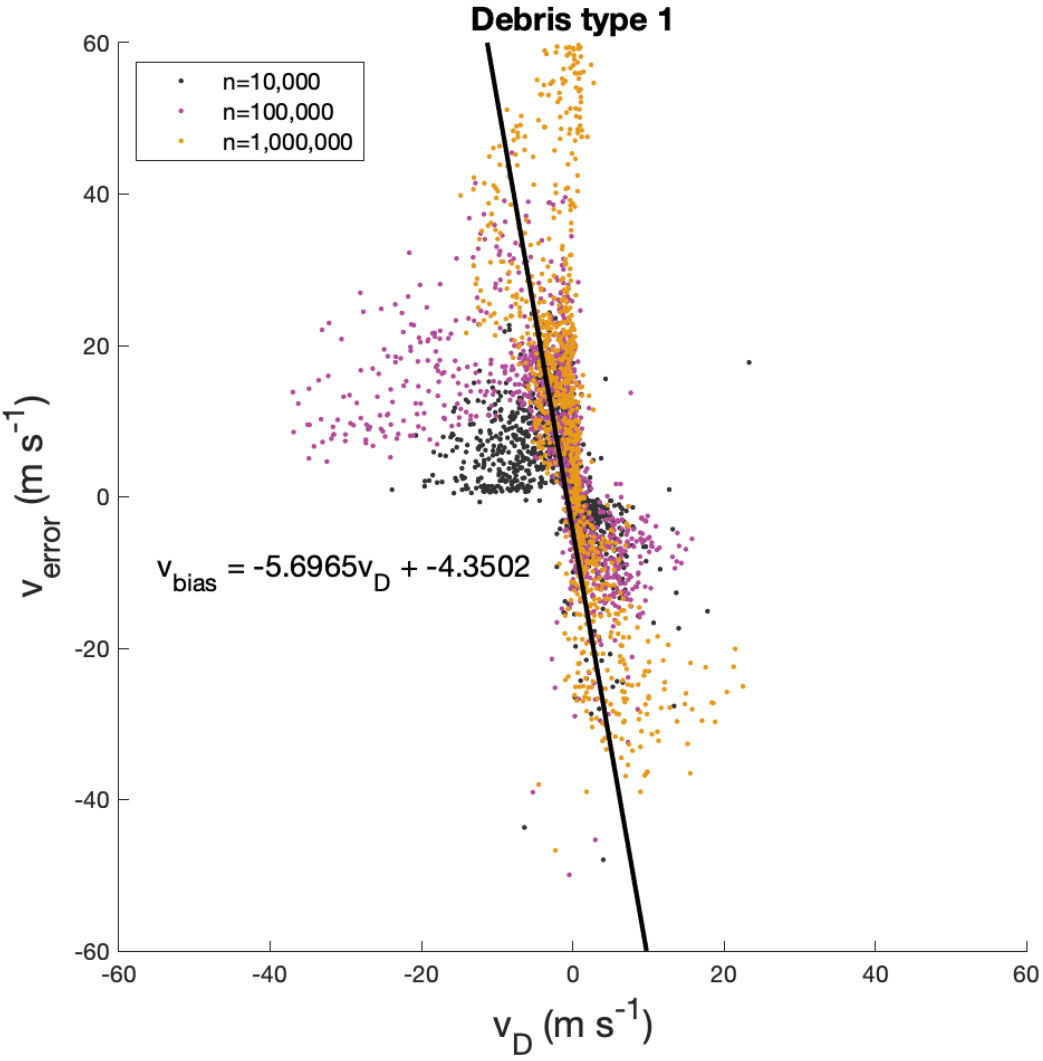

Figure 4.13: Scatter plot of Doppler velocity error as a function of differential velocity v_D for simulations with leaves at concentrations of 10,000 (black), 100,000 (purple), and 1,000,000 (yellow). Overlaid is the least-squares regression line (solid black) quantifying the relationship between velocity bias and v_D.

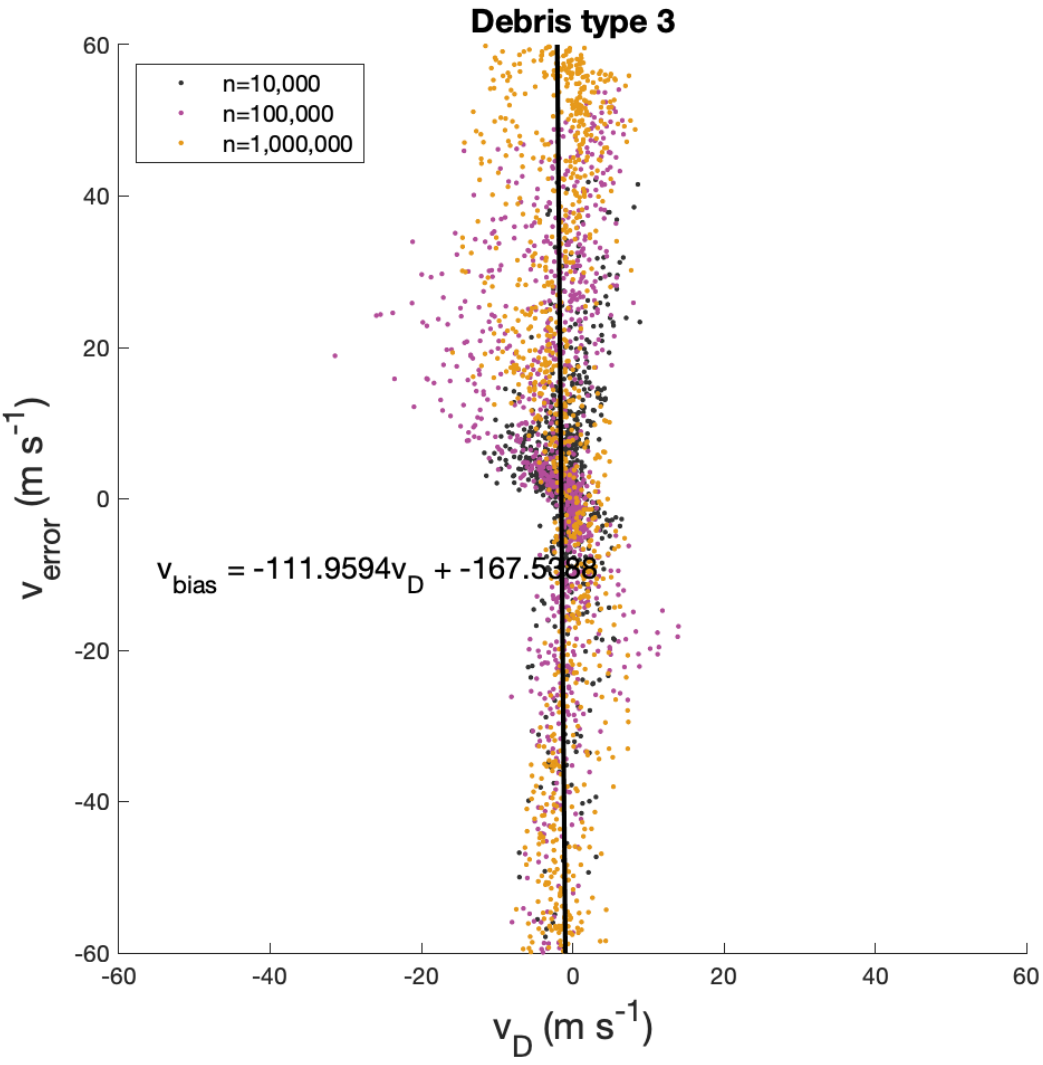

Figure 4.14: As in Fig. 4.13, but for wood boards (debris type 3).

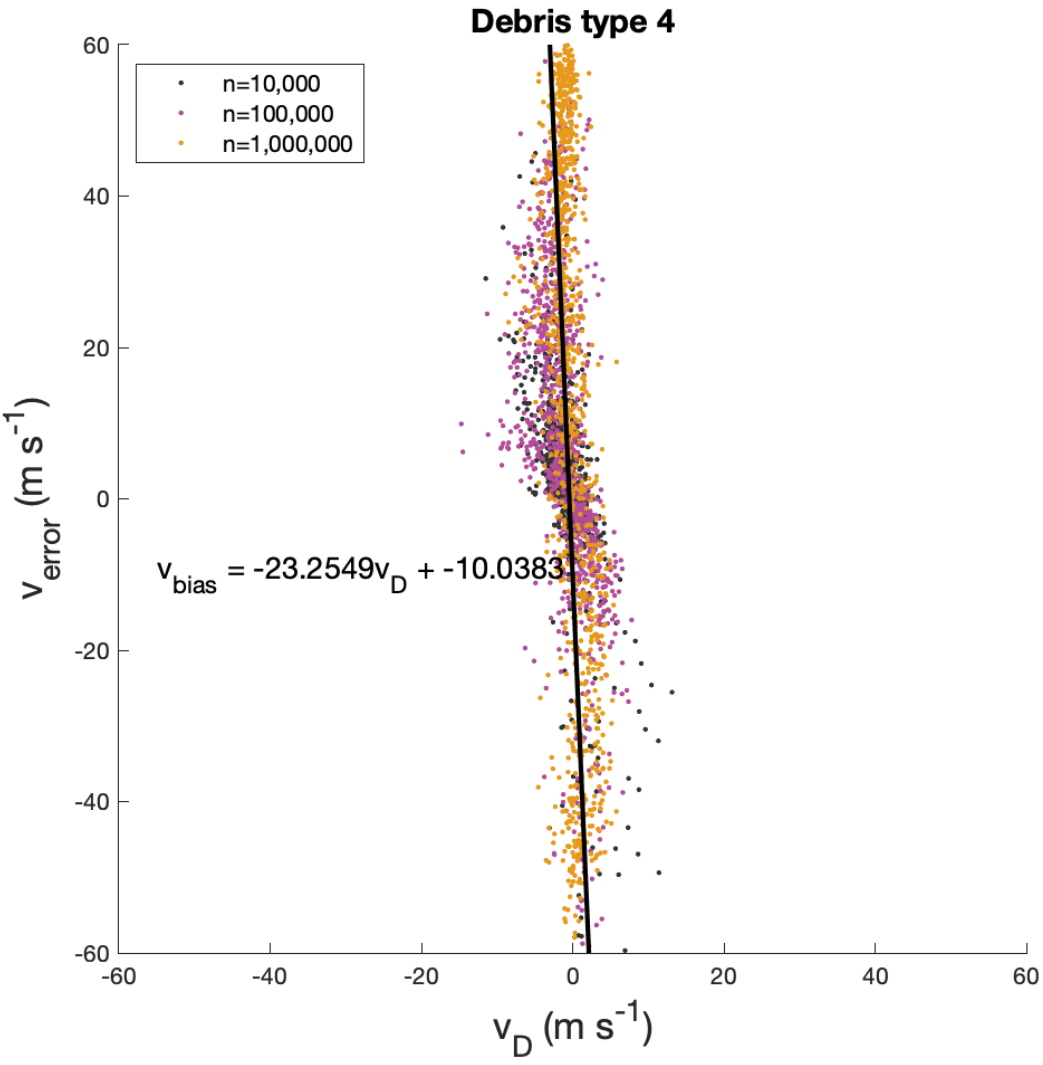

Figure 4.15: As in Fig. 4.13, but for wood boards (debris type 4).

The best-fit slopes generated through linear regression were significantly different between debris types. For the leaf, small wood board, and large wood board simulations, the slopes defining bias as a function of v_D were –6, –112, and –23, respectively, suggesting that there is no discernible dependence of these relationships on debris size. The fact that linear regression produced such vastly different best-fit lines means that these relationships are not robust—i.e., v_D is a poor predictor of velocity bias. Ultimately, these results indicate both qualitatively and quantitatively that there is little to no correlation between Doppler velocity bias and differential velocity, leaving the polarimetric radar quantities Z_H, Z_{DR}, and ρ_{HV} as the more viable potential predictors of velocity bias magnitude.

Chapter 5

Spectral Correction of Velocity Bias

While the moment-based approach to Doppler velocity bias correction discussed in Chapter 4.3 shows some potential for rough estimation of velocity error severity, our objective is to develop a method for more precise correction of these velocity errors. As discussed in Chapter 3.2, radar observations of debris are associated with both Doppler velocity bias and unique polarimetric signatures—therefore, DPSDs present an attractive method for correcting biased Doppler velocity measurements using polarimetric spectral analysis rather than bulk moment-based correlation.

5.1 Evaluation of DPSD Characteristics

To design an algorithm for debris identification based on DPSD estimates, we first characterize $s\hat{Z}_{DR}$ and $s\hat{\rho}_{HV}$ for rain and debris by comparing the magnitudes and statistical properties of several sample DPSDs for each case. The most significant DPSD properties for spectrally discriminating debris from rain are determined based on both qualitative and quantitative evaluations and comparisons of rain and debris DPSDs from SimRadar simulations. While only one representative DPSD example is shown for each case in this thesis, a large number of sample spectra for both cases were examined to identify the strongest potential spectral discriminators between rain and debris and subsequently determine optimal threshold values for each discriminating quantity. The results from this analysis are used to design a scatterer identification

algorithm to isolate rain- and debris-dominated velocities within a Doppler spectrum based on the spectral polarimetric characteristics of the signal.

We evaluate the respective characteristics of rain- and debris-dominated by comparing representative example spectra from each of these cases, then examining whether spectra from a realistic case display a combination of these characteristics. For reference, Table 5.1 gives a summary of the bulk polarimetric and moment characteristics of the following example spectra from the three cases. Fig. 5.1 shows an example of $s\hat{Z}_{DR}$ and $s\hat{\rho}_{HV}$ estimates from a rain simulation, along with the corresponding PSD estimate from the same resolution volume. The PSD is nearly symmetric and quasi-Gaussian, and the highest magnitude peak is near –20 m s^{-1}, indicating the dominant average Doppler velocity of rain drops within the resolution volume. Throughout the distribution, $s\hat{Z}_{DR}$ (Fig. 5.1a) has a mean value of approximately 1–2 dB with values ranging between 0 and 5 dB, while $s\hat{\rho}_{HV}$ (Fig. 5.1b) has a mean value close to 1.0, with values largely remaining above 0.9; as hypothesized in Chapter 3.2, these spectral patterns align with the expected bulk polarimetric characteristics of rain for Z_{DR} and ρ_{HV}. Additionally, both $s\hat{Z}_{DR}$ and $s\hat{\rho}_{HV}$ display extremely low variance, especially near the spectral peak between –40 and 0 m s^{-1} where most of the signal power is concentrated. The spectral signal variance is slightly larger in regions of low power toward the outer edges of the distribution, which is related to the increased statistical variability of a signal with reduced signal-to-noise ratio (SNR).

For comparison, Fig. 5.2 shows an example of $s\hat{Z}_{DR}$, $s\hat{\rho}_{HV}$, and corresponding PSD estimates from a debris simulation, but taken from the same resolution volume and time step as the spectra in Fig. 5.1 to facilitate meaningful comparison. In contrast with the rain signal, the PSD of the debris simulation has a much larger spectrum width than that of the rain simulation, and is strongly non-Gaussian and asymmetric.

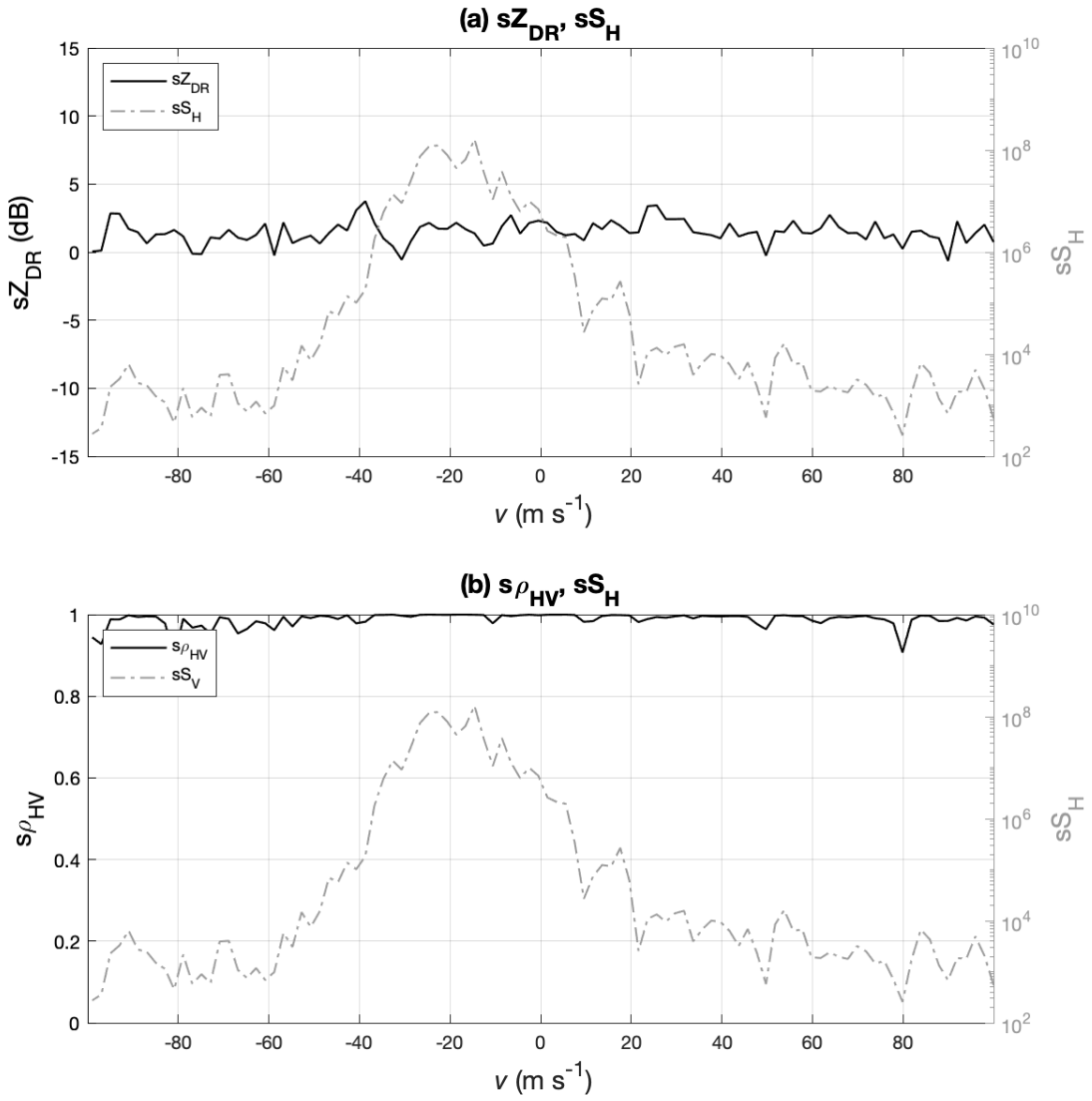

Figure 5.1: (a) $s\hat{Z}_{DR}$ and (b) $s\hat{\rho}_{HV}$ with corresponding $s\hat{S}_H$ for a rain signal.

The spectral peak is centered near a velocity of 30 m s^{-1}, which indicates that the predominant debris motion is in the opposite direction of the dominant rain motion within the same resolution volume. This difference in the position of the peak validates the hypothesis that *debris and rain presence within a PSD manifests as spectral peaks located at different velocities due to the differences in their trajectories.* Overall, the mean values of $s\hat{Z}_{DR}$ and $s\hat{\rho}_{HV}$ are much lower than those from the rain simulation, with $s\hat{Z}_{DR}$ primarily centered around negative values and $s\hat{\rho}_{HV}$ centered at values well below 1.0. In considering mean DPSD values only, these results again align with the hypothesis that the bulk and spectral polarimetric properties of debris should be similar—however, a major difference between the hypothesized DPSD characteristics and the actual DPSD estimates for the debris simulations in particular is the spectral variance of the estimates.

Both $s\hat{Z}_{DR}$ and $s\hat{\rho}_{HV}$ for the debris simulation display significantly larger variance throughout the entire spectrum than the DPSDs from the rain simulation. $s\hat{Z}_{DR}$ values range from 5 dB to below –15 dB, and $s\hat{\rho}_{HV}$ values fall across the entire range of possible correlation magnitudes, from 0.0 to nearly 1.0. While this behavior was not considered or accounted for in our original hypotheses about the polarimetric spectral characteristics of debris, a possible physical explanation is that the statistical properties of a polarimetric signal are partially dependent on its bulk ρ_{HV}. Low ρ_{HV} indicates weak correlation between the H and V channels, which introduces statistical variability and noise into the dual-polarized signal and thus degrades the quality of derived measurements (Bringi and Chandrasekar, 2001). The lower the magnitude of ρ_{HV}, the more the polarimetric signal is affected by decorrelation and quality degradation. Therefore, we hypothesize that the high spectral noise in DPSD estimates from debris

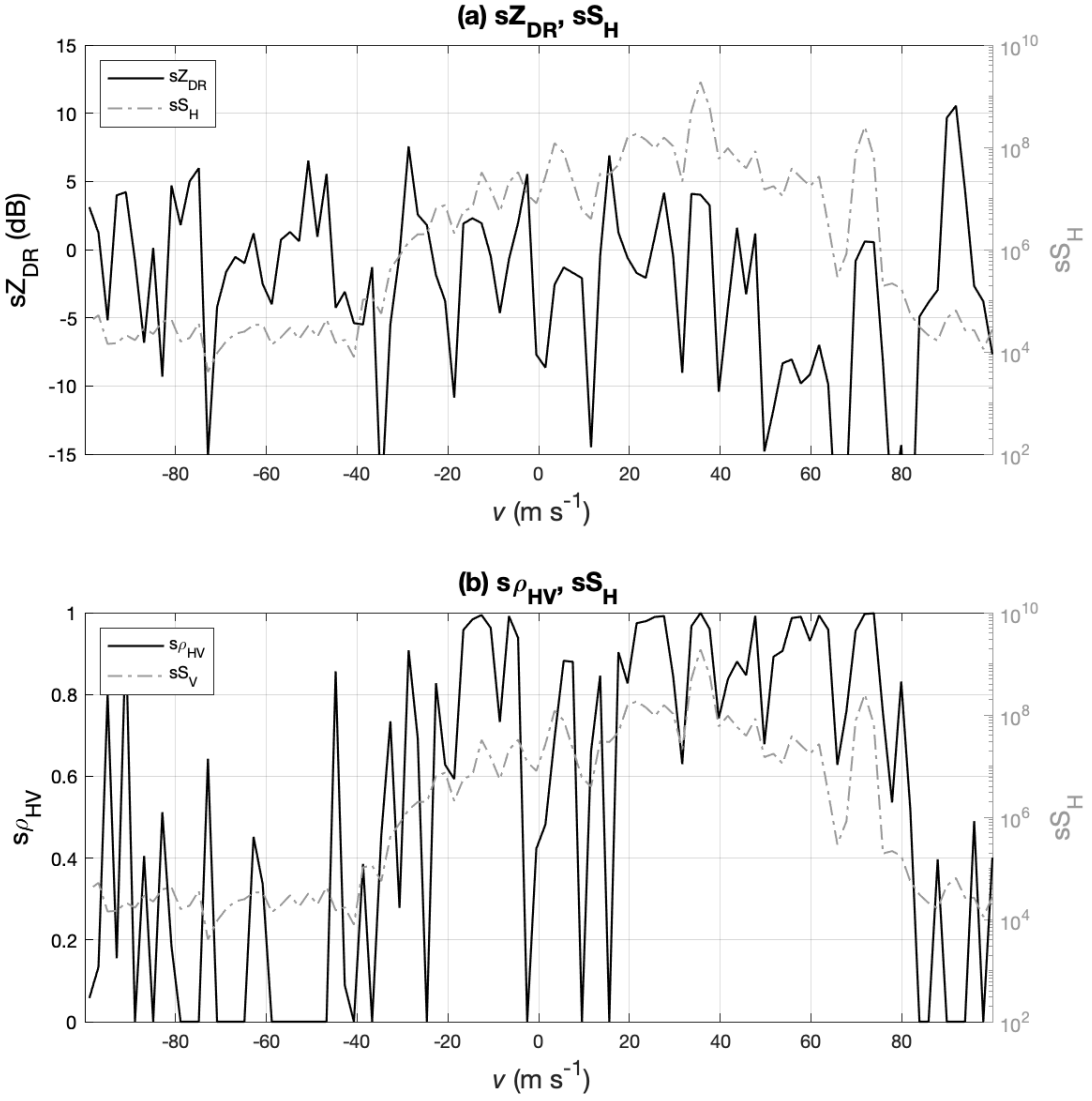

Figure 5.2: As in Fig. 5.1, but for a debris signal.

signals can be attributed, at least in part, to the statistical impacts of the low ρ_{HV} values associated with debris.

The DPSD characteristics described above for both rain and debris signals are consistent across varying tornado-relative radar gate positions, elevation angles, and debris types and concentrations—particularly the differences in variability between rain and debris DPSDs. Additionally, these characteristic differences between rain and debris are also present in DPSDs calculated using idealized I/Q data from the Yu et al. (2012) emulator. The example input and output DPSDs in Fig. 3.7 show that where the input spectra for sZ_{DR} and $s\rho_{HV}$ are assigned values typical of debris, the resulting output DPSD estimates for both $s\hat{Z}_{DR}$ and $s\hat{\rho}_{HV}$ have much higher variance compared to where the assigned values are more typical of rain. This pattern is replicated in DPSD estimates from a realistic simulation, again taken from the same resolution volume as the previous rain and debris spectra. Fig. 5.3 shows a bimodal PSD that approximately represents the superposition of the rain PSD from Fig. 5.1 and the debris PSD from Fig. 5.2; as such, the left peak of the PSD is taken as the rain-dominated peak while the right peak of the PSD is taken as the debris-dominated peak. At velocities corresponding to the rain peak, both DPSDs have low variance, with $s\hat{Z}_{DR} \approx 2$ dB and $s\hat{\rho}_{HV} \approx 1.0$. In contrast, $s\hat{Z}_{DR}$ and $s\hat{\rho}_{HV}$ have much higher variance and lower magnitudes near the debris peak, with $s\hat{Z}_{DR} < 0$ dB and $s\hat{\rho}_{HV} \ll 1.0$ on average at these velocities.

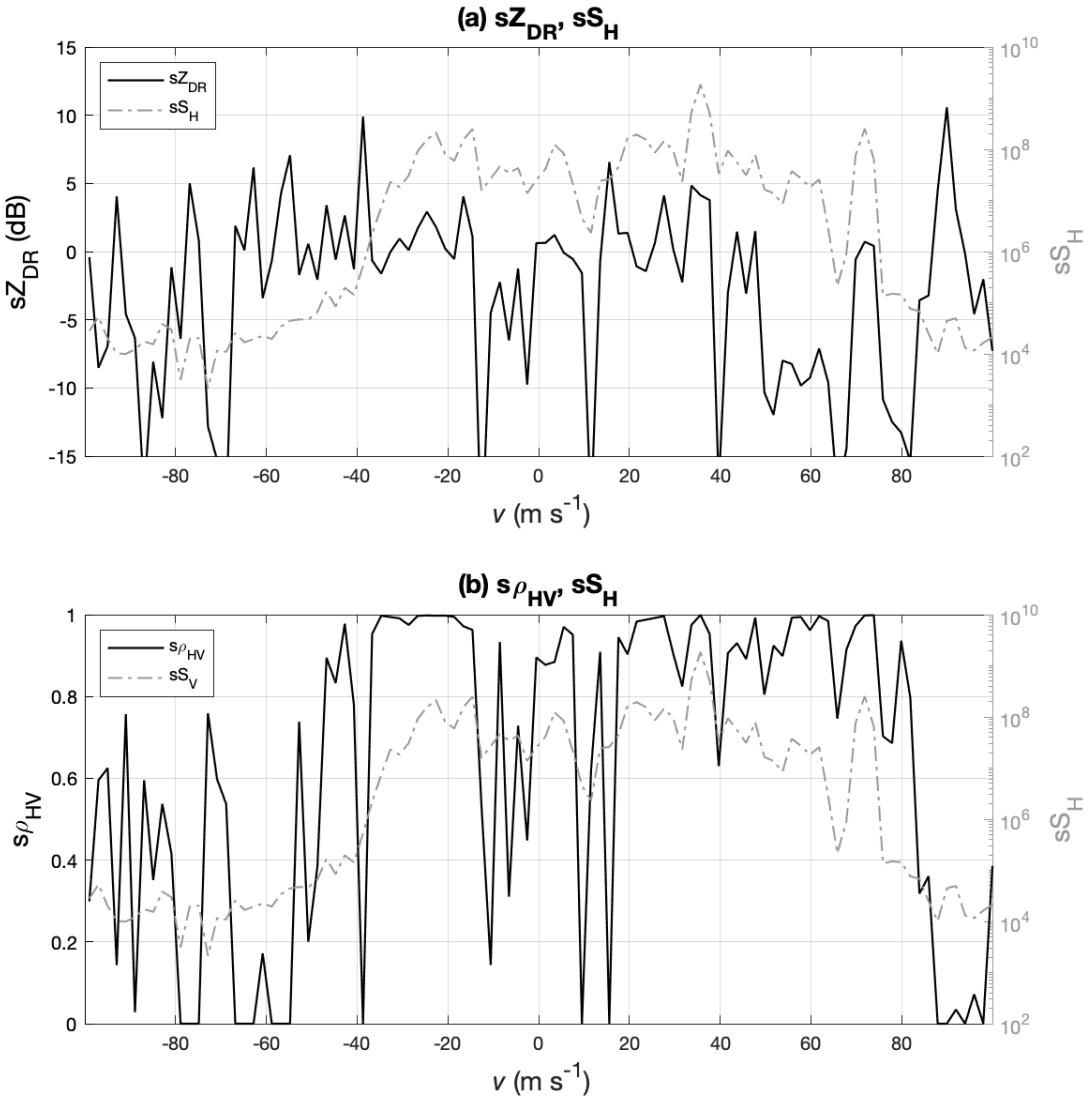

Figure 5.3: As in Fig. 5.1, but for a realistic signal.

Table 5.1: Bulk radar moment and polarimetric quantities for the sample spectra in Figs. 5.1–5.3.

	Rain	Debris	Realistic
Z_H (dBZ)	41	47	48
v_r (m s^{-1})	-17	35	26
Z_{DR} (dB)	1.8	1.2	1.3
ρ_{HV}	0.99	0.76	0.41

5.2 Debris Classification Algorithm

Given the significant differences in both the magnitudes and variances of $s\hat{Z}_{DR}$ and $s\hat{\rho}_{HV}$ between rain- and debris-dominated cases, we designate these quantities as the most effective spectral discriminators between debris and rain. Based on the uncertainty and vagueness inherent in radar observations, it was decided that the identification of debris and rain within a spectrum would be best-suited for a fuzzy logic debris classification algorithm (DCA). Fuzzy logic is a system of logic based on fuzzy set theory, in which there is similarity between sets, and the elements of a given set have degrees of membership to that set. As opposed to classical Boolean logic, where the truth value of a variable is either 0 (false) or 1 (true), fuzzy logic is designed to account for uncertainty, partial truth, and incomplete information—when the boundaries between sets are "fuzzy", or vague. Truth values in fuzzy logic can fall anywhere within the range of real numbers from 0 to 1, and are represented by membership functions, which quantify the degree to which a variable or element is a member of a given set. The same variable can have varying degrees of membership to multiple different sets, or classes. In applications where deterministic classification of elements using Boolean logic is not possible, fuzzy logic becomes useful for identifying the most likely classification of each element.

Fuzzy logic classification has three steps: fuzzification, aggregation, and defuzzification. During the fuzzification process, the membership functions $P^{(i)}(X_j)$ are created to represent a normalized distribution of values of a variable X_j for the ith class. These membership functions are empirically determined using the statistics of known observations, and are often represented as continuous trapezoidal functions with a maximum value of 1 and a minimum value of 0. Each membership function is defined by a range of threshold values X_1–X_4. Outside of this range, the membership function $P^{(i)}(X_j)$

is set to 0 for that class—in other words, the probability of a member of the ith class having a value outside of the range X_1–X_4 is 0. In applications, the thresholds X_1–X_4 are chosen based on the statistics of observed variable distributions. X_1 is chosen at the 0.5th percentile, X_2 at the 20th percentile, X_3 at the 80th percentile, and X_4 at the 99.5th percentile (Zhang, 2019).

Once membership functions have been generated, the second step in fuzzy logic classification is aggregation. During aggregation, the membership values for a given set of observations are calculated and summed to obtain the aggregation parameter for each class. The aggregation parameter for the ith class is given by

$$A_i = \frac{\sum_{j=1}^{N} W_{ij} P^{(i)}(X_j)}{\sum_{j=1}^{N} W_{ij}}, \tag{5.1}$$

where N is the total number of variables X_j, and W is a weighting value controlling the significance of each variable X_j in the summation based on its robustness as a discriminator between classes. The aggregation parameter for each class is a measure of the relative likelihood that the given input observations correspond to that class—i.e., the fuzzy truth value for that set. The fuzzy logic classification process ends with defuzzification, wherein the aggregation parameters for each class are compared. The classification of an input observation is determined by the class with the largest aggregation value and thus the highest relative likelihood of producing the given input observation. In this manner, the fuzzy truth values are converted into classical Boolean truth values, as the resulting membership of an observation becomes 1 (true) for the class with the largest aggregation value and 0 (false)

The most common application of fuzzy logic in radar meteorology is the hydrometeor classification algorithm (HCA). Most operational HCAs take three input radar measurements—Z_H, Z_{DR}, and ρ_{HV}—to classify radar returns as one of ten defined

scatterer classes: ground clutter or abnormal propagation, biological scatterers, dry aggregated snow, wet snow, ice crystals, graupel, big drops, light to moderate rain, heavy rain, or mixed rain and hail (Vivekanandan et al., 1999; Straka et al., 2000). Fuzzy logic is the optimal method for performing these classifications for a multitude of reasons. The predominant reason for using fuzzy logic in radar meteorology is that many of these hydrometeor classes can have overlapping polarimetric characteristics, making it difficult to discern deterministically whether a radar return is characterized by one scatterer type of another. Furthermore, radar measurements contain calibration error that can mask the true signal, and multiple scatterer types can be present within a single resolution volume.

The DCA designed for this work is different from an operational HCA—first, rather than having ten membership classes, the DCA has only two classes: debris and rain. More significantly, the DCA is an algorithm designed for spectral scatterer classification rather than bulk classification, making it a novel application of fuzzy logic in radar meteorology. Based on the characteristic properties of rain and debris DPSDs identified in Section 5.1, we chose to use the magnitudes of $s\hat{Z}_{DR}$ and $s\hat{\rho}_{HV}$ as well as the 9-point moving block variance of $s\hat{\rho}_{HV}$, or $\sigma^2_{s\rho_{HV}}$, as the input observations for the DCA.

The membership functions for each variable were empirically determined by approximating the number distributions of these three spectral variables for both rain and debris by compiling values from multiple SimRadar simulations. The debris DPSD distributions contain data from 12 total simulations of debris types 1 and 3 (leaves and wood boards) with concentrations of 10,000, 100,000, and 1,000,000 and elevation angles of 1.0° and 2.0°. The rain DPSD distributions contain data from 10 total rain simulations at elevation angles ranging from 0.5° to 5.0° in half-degree increments. Histograms showing the total number distributions of $s\hat{Z}_{DR}$, $s\hat{\rho}_{HV}$, and $\sigma^2_{s\rho_{HV}}$ obtained

from these simulations are shown in Fig. 5.4, along with the resulting trapezoidal membership functions that roughly represent each distribution.

Qualitatively, the distributions of $s\hat{Z}_{DR}$ and $s\hat{\rho}_{HV}$ values are consistent with *a priori* knowledge of characteristic bulk polarimetric values for both debris and rain. As in nature, $s\hat{Z}_{DR,debris}$ takes on a wide range of values both positive and negative, with a mean value of $\mu = -0.8$ dB and an approximate range of -20–20 dB, as well as slight negative skewness. These statistics match with observations that debris tends to generate near-zero values of bulk Z_{DR}, but can be highly variable in many cases due to hypothesized processes such as common alignment (e.g., Umeyama et al., 2018), resonance scattering (e.g., Ryzhkov et al., 2005), or large positive or negative intrinsic Z_{DR} of individual debris pieces (e.g., Bodine et al., 2014). In comparison, the distribution of $s\hat{Z}_{DR,rain}$ is much narrower, with a mean value of $\mu = 1.5$ dB and an approximate range of 0–4 dB. This distribution is again consistent with existing observations of bulk Z_{DR} for rain, which can vary from 0 dB for the smallest rain drops to around 4–5 dB for large drops, but are most often near 1–2 dB in a typical rain environment.

The number distributions of $s\hat{\rho}_{HV,debris}$ and $s\hat{\rho}_{HV,rain}$ are similarly consistent with prior observations of bulk ρ_{HV} for debris and rain. In particular, the distribution of $s\hat{\rho}_{HV,rain}$ is almost entirely concentrated within the 0.95–1.0 range, while $s\hat{\rho}_{HV,debris}$ has a distribution with a long "tail" due to the low values of ρ_{HV} that can be generated by debris. Interestingly, however, the overall shapes of the debris and rain distributions are similar, with the mode of both distributions located at the 0.95–1.0 bin, rather than $s\hat{\rho}_{HV,debris}$ having a lower-valued peak than $s\hat{\rho}_{HV,rain}$ as was expected. This is likely related to our earlier qualitative observations that debris-dominated signals produce DPSDs with high variance rather than characteristic polarimetric values uniformly throughout the spectrum. Therefore, since $s\hat{\rho}_{HV,debris}$ tends to fluctuate drastically

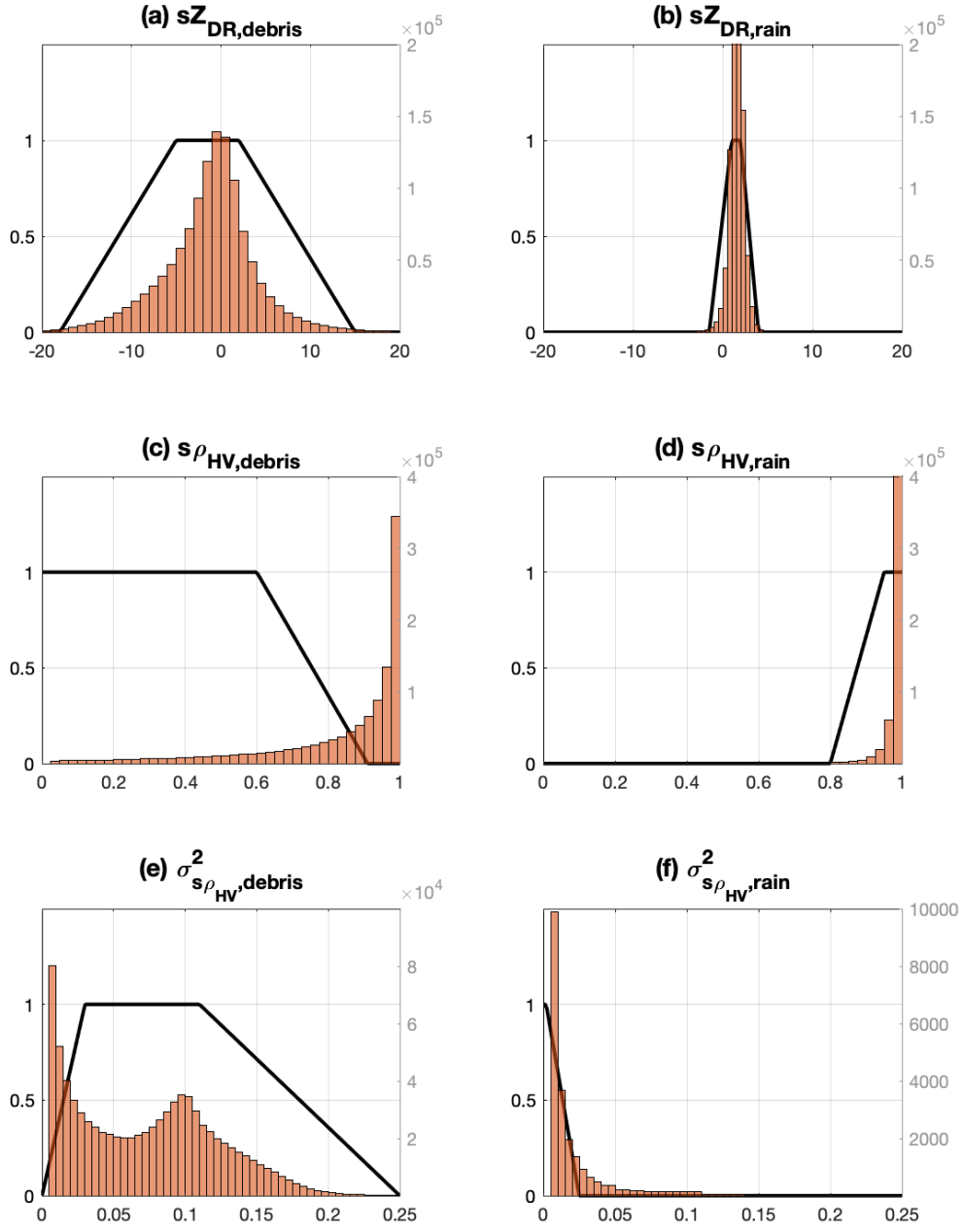

Figure 5.4: Histograms showing the number distributions of (top)–(bottom) $s\hat{Z}_{DR}$, $s\hat{\rho}_{HV}$, and $\sigma^2_{s\rho_{HV}}$ for debris (left) and rain (right). Derived rain and debris membership functions for each variable are overlaid (solid black).

between high and low values, it follows that debris signals would show an accumulation of high $s\hat{\rho}_{HV}$ values with a long "tail" of lower values due to the fluctuation between extremes.

The distributions of $\sigma^2_{s\rho_{HV}}$ for rain and debris show differences that are consistent with our observations about DPSD variance in the previous section. While both distributions show a primary peak at extremely low variances near 0, $\sigma^2_{s\rho_{HV,debris}}$ has a secondary peak near $\sigma^2_{s\rho_{HV}} = 0.1$ that is not present in the distribution of $\sigma^2_{s\rho_{HV,rain}}$. This secondary peak in the $\sigma^2_{s\rho_{HV,debris}}$ distribution reflects the higher variance observed qualitatively in the debris-dominated DPSDs, while the low-variance peak is possibly a product of the statistical spectral variability associated with low bulk ρ_{HV}.

Table 5.2 shows the threshold values X_1–X_4 for each membership function. While most of the chosen values follow the 0.5–20–80–99.5 percentile convention used in operational HCAs, there are four chosen thresholds that deviate from that convention because of the unique characteristics and behavior of DPSDs. First, X_2 for $s\hat{\rho}_{HV,rain}$ uses the 5th percentile value of 0.95 instead of the 20th percentile value of 0.99, which we felt would be too restrictive of a threshold. The 0.5th and 20th percentile value of $s\hat{\rho}_{HV,debris}$ are shifted from X_1 to X_2 and X_2 to X_3, respectively, to reflect the fact that only debris produces $s\hat{Z}_{DR}$ values within this range, while X_4 uses the 50th percentile value of 0.91 instead of the 80th percentile value of 0.98 because only 20% of the $s\hat{\rho}_{HV,debris}$ distribution falls above 0.98, while more than 80% of the $s\hat{\rho}_{HV,rain}$ distribution lies above 0.98. Therefore, we felt that using the 80th and 99.5th percentiles for $s\hat{\rho}_{HV,debris}$ would not be strict enough to prevent rain from being misidentified as debris. X_2 for $\sigma^2_{s\rho_{HV,debris}}$ uses the 50th percentile value of 0.03 instead of the 20th percentile value of 0.0014 for the same reason: to increase the strictness of the debris membership function to prevent underclassification of rain. Finally, X_3 for $\sigma^2_{s\rho_{HV,rain}}$

Table 5.2: Rain and debris membership function thresholds for (top)–(bottom) $s\hat{Z}_{DR}$, $s\hat{\rho}_{HV}$, and $\sigma^2_{s\rho_{HV}}$. Unless marked with a *, the membership thresholds are the (left)–(right) 0.5th, 20th, 80th, and 99.5th percentiles of the corresponding distribution. (*5th percentile; **50th percentile; ***95th percentile)

Membership		X_1	X_2	X_3	X_4
$s\hat{Z}_{DR}$	Rain	-1.5	1	2	4
	Debris	-18	-5	2	15
$s\hat{\rho}_{HV}$	Rain	0.8	0.95	1.0	–
	Debris	–	0	0.6	0.91
$\sigma^2_{s\rho_{HV}}$	Rain	–	0	0.002	0.025
	Debris	0	0.03	0.11	0.25

uses the 95th percentile value of 0.002 rather than the 80th percentile value of 2×10^{-4} because we felt that the 80th percentile would be too restrictive for rain membership.

Fig. 5.5 shows an example $s\hat{Z}_{DR}$ spectrum with its associated membership functions for rain and debris. The rain membership function shows a primary peak approximately between –55 and –30 m s^{-1}, with a narrower secondary peak approximately between 45 and 50 m s^{-1}, suggesting that the identification of rain within a spectrum using $s\hat{Z}_{DR}$ should be fairly straightforward. However, the debris membership function shows high degrees of membership throughout the entirety of the spectrum, including the regions where the rain membership function is large—at the peaks where the rain membership function is close to 1, the debris membership function shows values close to 1 as well. The significant overlap between the rain and debris membership functions therefore makes it highly difficult to discern between rain and debris using $s\hat{Z}_{DR}$ alone due to the wide range of values in the $s\hat{Z}_{DR}$ number distribution seen in Fig. 5.4a, which will lead to the masking of rain-dominated spectral components. Because the membership for $s\hat{Z}_{DR}$ is so easily saturated and masked by debris, it is a poor discriminator between rain and debris and will thus receive much lower weight in the aggregation step of the DCA to minimize the masking of rain by debris.

Fig. 5.6 shows an example of $s\hat{\rho}_{HV}$ with its associated rain and debris membership functions for the same time series as in Fig. 5.5. The rain membership function shows three primary peaks—one between –50 and –35 m s^{-1}, another between 5 and 20 m s^{-1}, and a third weaker peak between approximately 45 and 65 m s^{-1}—which align with regions where $s\hat{\rho}_{HV} \approx 1$. Unlike $s\hat{Z}_{DR}$, however, the debris membership function for $s\hat{\rho}_{HV}$ shows local minima in the regions where rain membership shows local maxima, meaning that rain is much less likely to be masked and misidentified as debris when using $s\hat{\rho}_{HV}$. However, there is a considerable amount of variability in

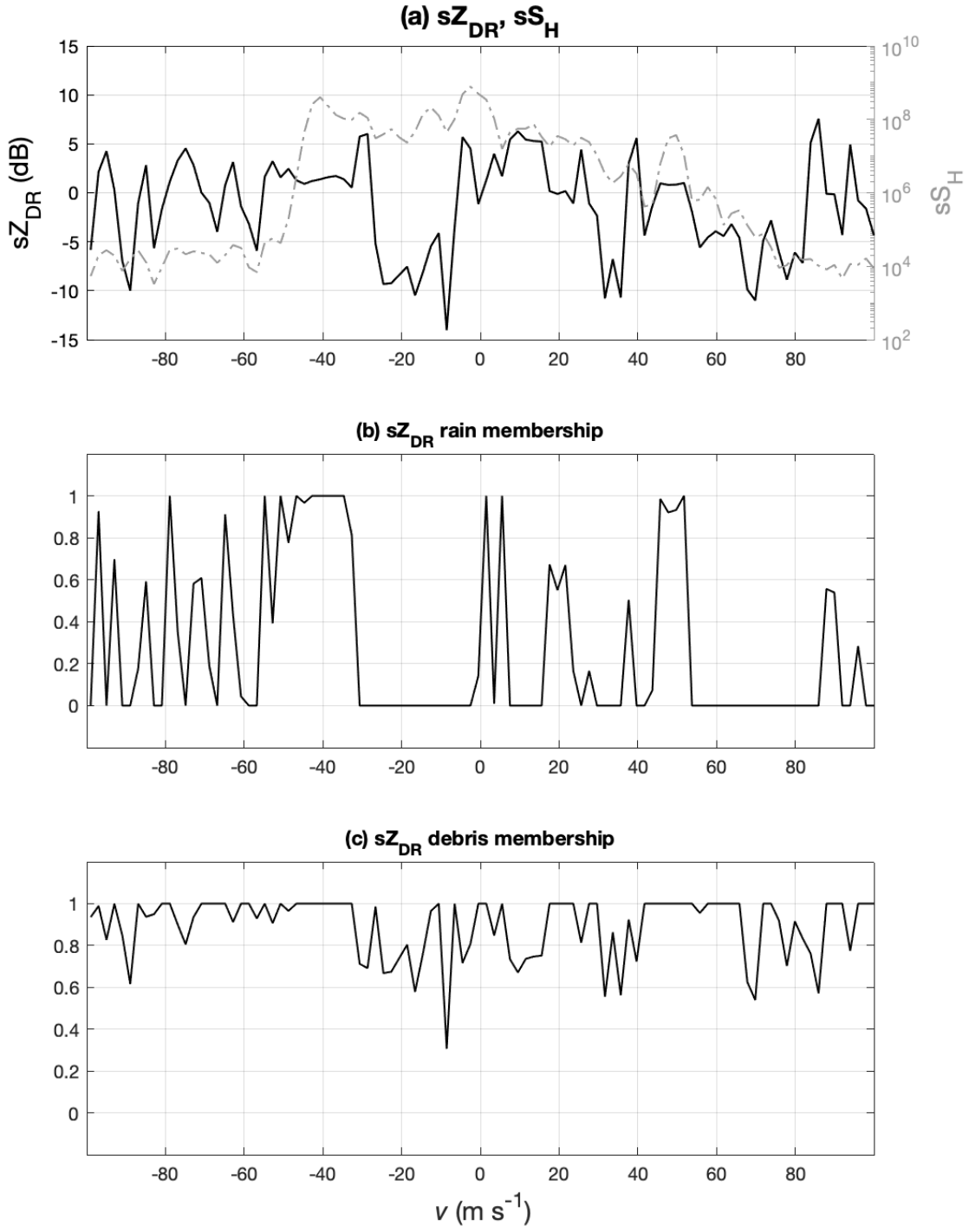

Figure 5.5: (a) $s\hat{Z}_{DR}$ and $s\hat{S}_H$, and membership functions for (b) rain and (c) debris.

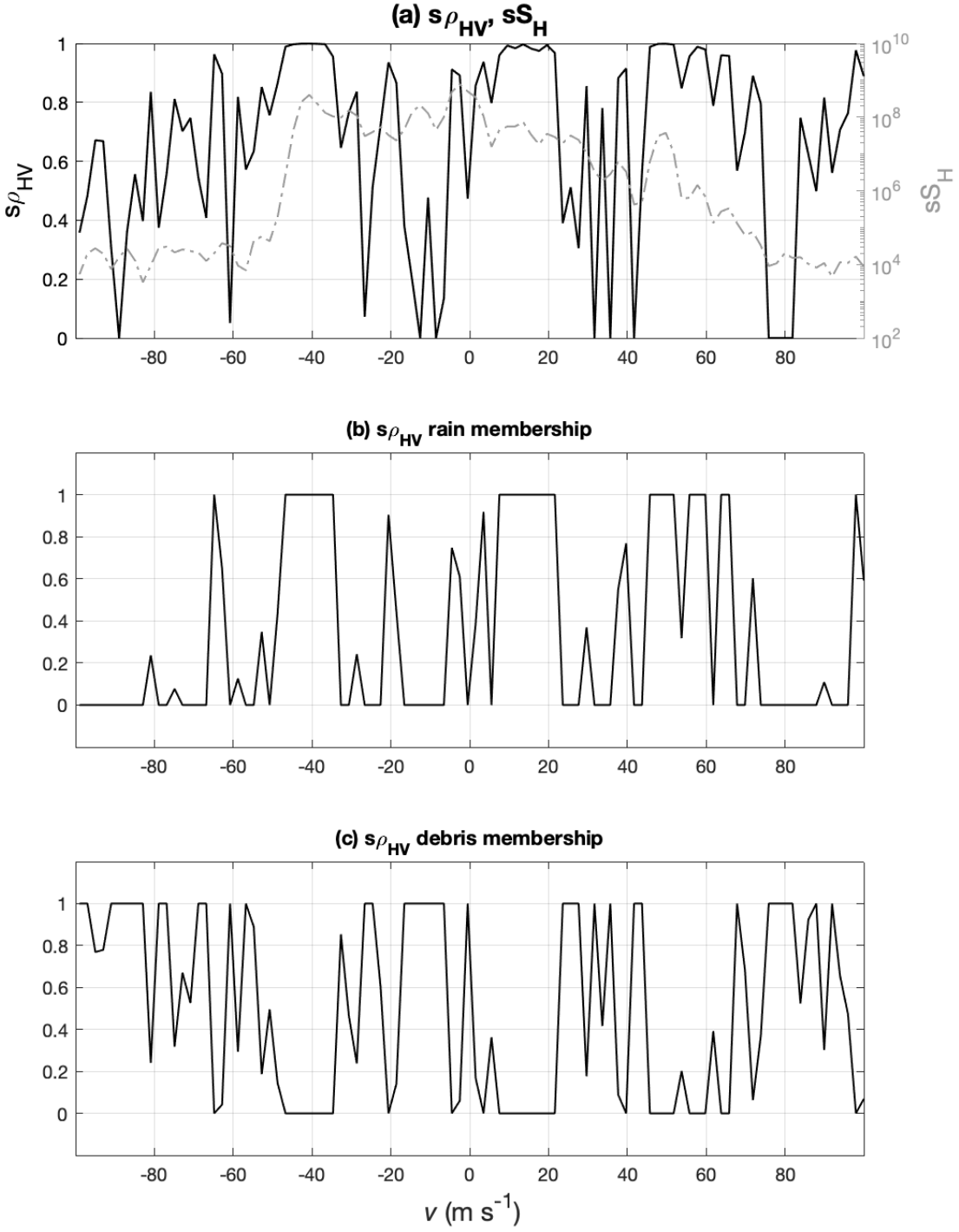

Figure 5.6: As in Fig. 5.5, but for $s\hat{\rho}_{HV}$.

both membership functions, which could still result in some amount of masking of the true scatterer type. Despite this possibility, $s\hat{\rho}_{HV}$ is still a much better discriminator between rain and debris and will therefore receive more weight in the aggregation step of the DCA.

Fig. 5.7 shows $\sigma^2_{s\rho_{HV}}$ and its corresponding membership functions for rain and debris for the same time series as the previous two figures. Similarly to $s\hat{\rho}_{HV}$ and its membership functions in Fig. 5.6, the rain membership function for $\sigma^2_{s\rho_{HV}}$ shows three clear peaks—one between –50 and –35 m s^{-1}, one between 5 and 15 m s^{-1}, and one between 50 and 65 m s^{-1}. Also similarly, the debris membership function shows clear local minima at these same locations, meaning that $\sigma^2_{s\rho_{HV}}$ is also a good discriminator between rain and debris. Unlike $s\hat{\rho}_{HV}$, however, there is much lower variability in the membership functions for $\sigma^2_{s\rho_{HV}}$, especially in the rain membership functions, which show peaks with membership values near 1 and values of 0 everywhere else. Therefore, we feel that $\sigma^2_{s\rho_{HV}}$ is an effective discriminator between rain and debris, and will thus receive the highest weight in the aggregation step of the DCA.

The aggregation parameters for debris and rain at each velocity are calculated using weighted membership functions, given by

$$A_i = 0.2P^{(i)}(s\hat{Z}_{DR}) + 0.3P^{(i)}(s\hat{\rho}_{HV}) + 0.5P^{(i)}(\sigma^2_{s\rho_{HV}}), \tag{5.2}$$

such that the maximum possible value of either aggregation parameter is 1, and $\sigma^2_{s\rho_{HV}}$ receives the most weight while $s\hat{Z}_{DR}$ receives the least weight for the reasons discussed previously. A weight coefficient of 0.2 is assigned to $s\hat{Z}_{DR}$ because although the rain membership function effectively identified the same regions of rain as the other input DPSD variables, there was significant overclassification of debris. Therefore, rather

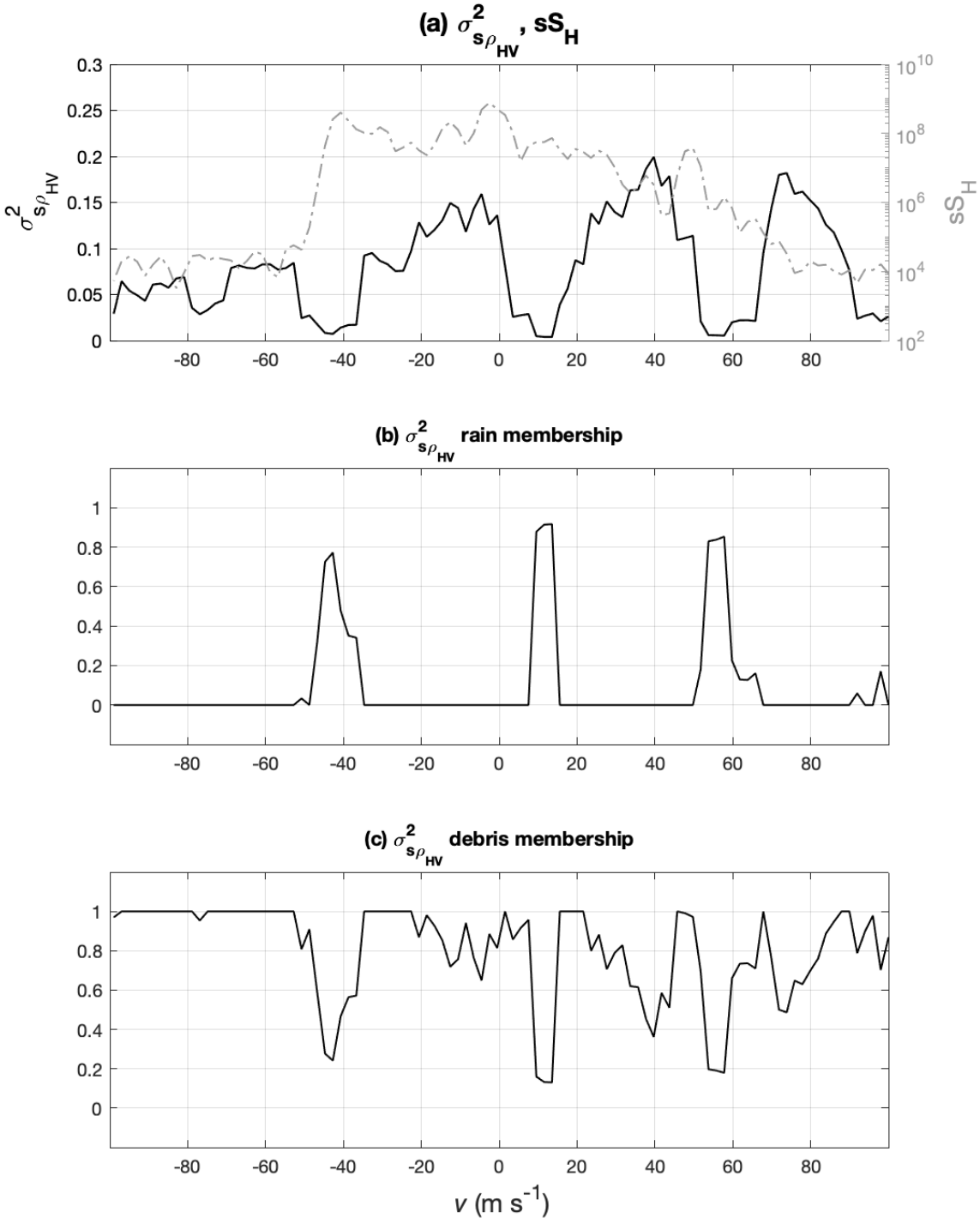

Figure 5.7: As in Fig. 5.5, but for $\sigma^2_{s\rho_{HV}}$.

than removing $s\hat{Z}_{DR}$ from the DCA entirely, we chose to assign it a low weight coefficient in order to take advantage of its effectiveness in identifying rain without allowing the aggregation parameters to be dominated by the debris saturation seen in Fig. 5.5c. $s\hat{\rho}_{HV}$ and $\sigma^2_{s\rho_{HV}}$ were thus assigned weight coefficients of 0.3 and 0.5, respectively, to reflect the observation that both are more effective discriminators between rain and debris than $s\hat{Z}_{DR}$, but that $\sigma^2_{s\rho_{HV}}$ was determined to be the most robust discriminator compared to $s\hat{\rho}_{HV}$ and so should be assigned a higher weight than $s\hat{\rho}_{HV}$. With this aggregation weighting scheme, therefore, the resulting scatterer classification output for the example PSD in Figs. 5.5–5.7 is shown in Fig. 5.8, along with the associated DPSDs $s\hat{Z}_{DR}$ and $s\hat{\rho}_{HV}$.

An important characteristic to note about the output scatterer classification is that spectral components are classified as debris by the DCA unless they are associated with a clear rain peak. In particular, spectral regions with low SNR—which, in reality, should be dominated by neither rain nor debris, but random noise—are all classified as debris. As discussed earlier in this chapter with respect to low bulk ρ_{HV}, this classification of low-SNR regions as debris is likely related to the increased statistical variability inherent to low-SNR signals (Bringi and Chandrasekar, 2001). This enhanced statistical variability will thus be present in the low-SNR regions of corresponding DPSD estimates as well. The significance of this behavior is that because $\sigma^2_{s\rho_{HV}}$ is given such high weight in the aggregation step of the DCA, these low-SNR, high-variability regions will largely be classified as debris. As will be discussed in the following section, this overclassification of debris in low-SNR regions may have implications for the accuracy and robustness of velocity recalculations based on the DCA output.

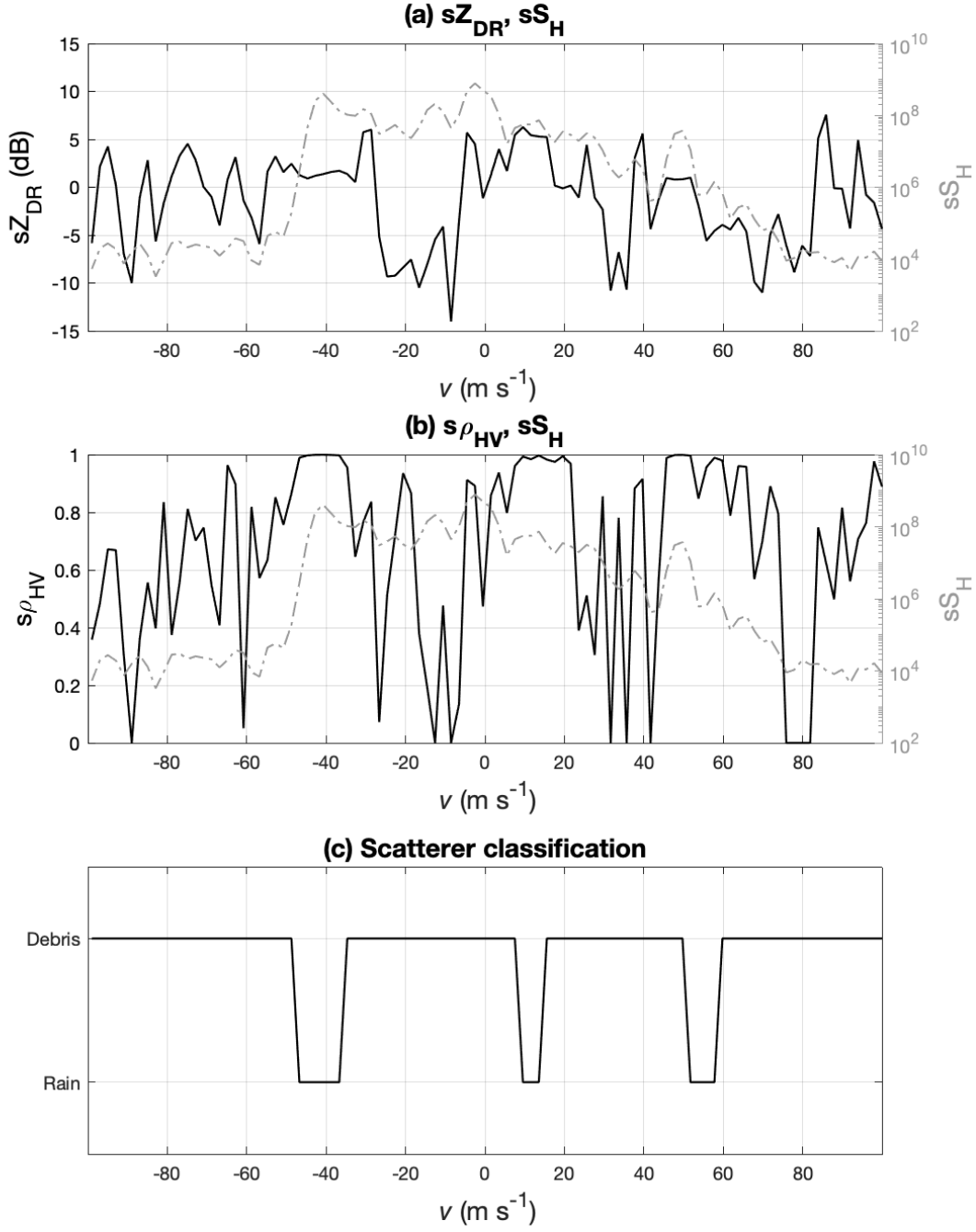

Figure 5.8: (a) $s\hat{Z}_{DR}$, (b) $s\hat{\rho}_{HV}$, and (c) the resulting DCA classifications for an example spectrum.

5.3 Velocity Bias Correction

5.3.1 Spectral Filtering Methods

Ultimately, the output classifications from the DCA are used to filter debris-dominated contributions from the original PSD so that only rain-dominated contributions remain. At velocities that have been classified as debris, the signal power is set to 0, while at velocities classified as rain, the signal power remains the same. This process should result in a filtered PSD in which only the rain-dominated signal power contributions are preserved from the original PSD. After spectral debris contamination is removed, the Doppler velocity is recalculated directly from the filtered PSD as

$$\hat{v} = -\frac{\lambda}{2M}\left\{\frac{k_m}{T_s} + \frac{1}{\hat{P}T_s}\sum_{k_m-M/2}^{k_m+M/2}(k-k_m)\hat{S}[mod_M(k)]\right\}, \tag{5.3}$$

from Doviak and Zrnić (1993), where k is the spectral index and k_m is the spectral index of the strongest Fourier coefficient in the PSD (i.e., the approximate mean return frequency of the signal), M is the number of samples in the time series signal, T_s is the PRT of the radar, $\hat{P}$ is the total power in the periodogram $\hat{S}$, λ is the radar wavelength, and $\mathrm{mod}_M(k)$ is the modulo function representing the remainder from dividing k by M, which is included to eliminate bias due to frequency aliasing. Ideally, the removal of debris-dominated components from the PSD should result in a new velocity estimation free of debris-induced bias using this method. An example of this DCA-based velocity correction method is shown in Fig. 5.9.

The recalculated velocity using the filtered Doppler spectrum shows significant improvement from the original velocity estimate, with a reduction of bias from 25.6 m s^{-1} to 8.1 m s^{-1} in this example. However, as noted in the previous section, the DCA

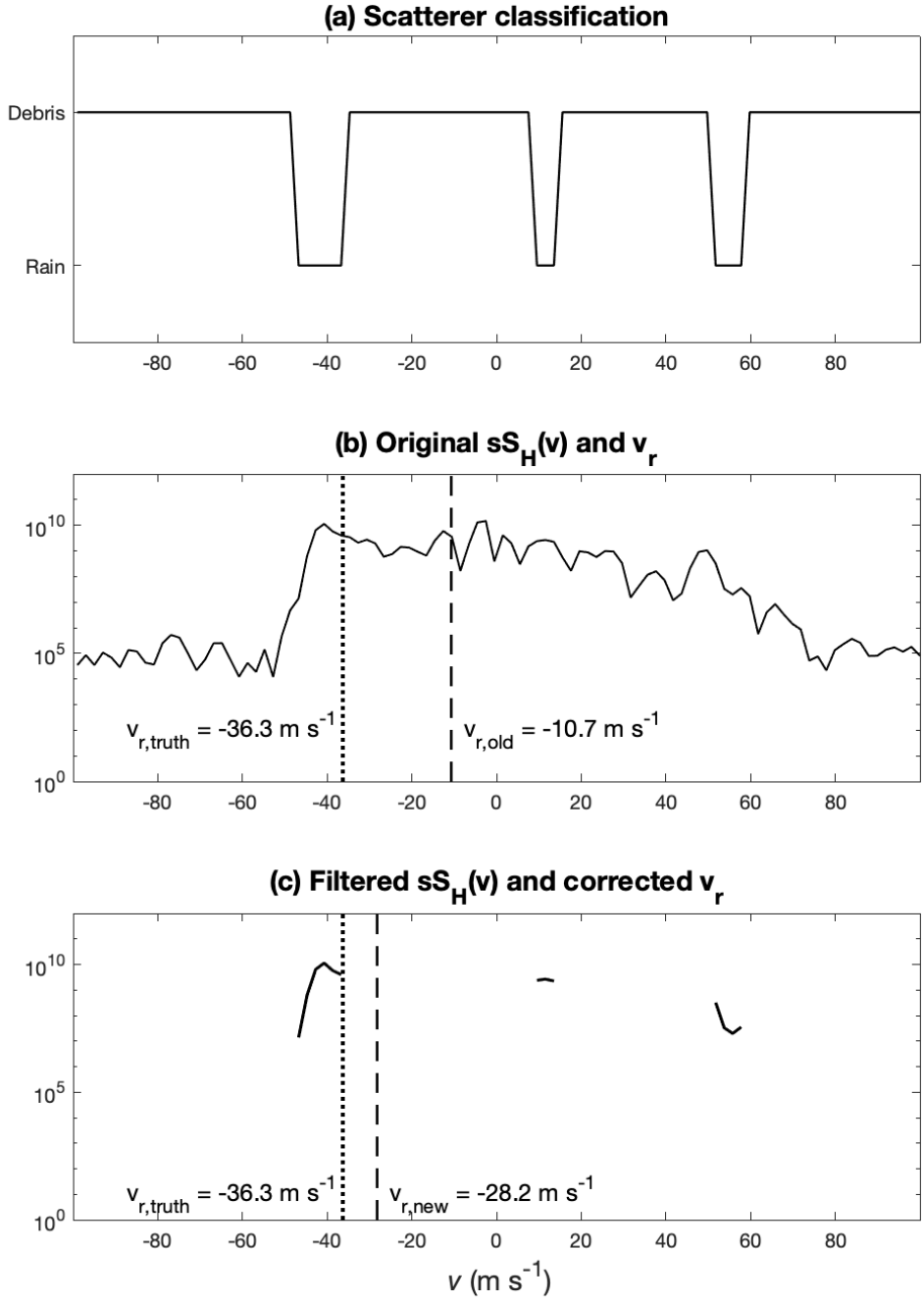

Figure 5.9: (a) DCA output, (b) original PSD and v_r, and (c) filtered PSD and resulting v_r using Eq. 5.3.

tends to overclassify debris presence in a spectrum, particularly in low-SNR regions of the PSD. The result of this DCA behavior in velocity re-estimation is illustrated clearly in Fig. 5.9c. Ultimately, the DCA-based filtering of the PSD preserves little of the original signal with which to estimate the Doppler velocity.

Additionally, the time series from which this example was generated (as well as the examples in Figs. 5.5–5.7) is from a simulation at a tilt of 0.5° with 10,000 wood boards—the low concentration—meaning that spectra from signals with a higher debris concentration will likely be even more saturated by debris contamination, especially at low tilts. As a result, there exists a non-negligible possibility that, in events with high concentrations of debris, there may not be enough remaining spectral components after applying the DCA filter to recalculate a robust, accurate velocity. Another possible outcome of such debris saturation and overclassification is that the preservation of rain signal components may be driven more by random statistical variability in the signal and DPSD estimates than by any actual dominance of a rain signal—i.e., a "false positive" for rain from the DCA. Because of the considerable spectral overlap between rain and debris, binary classification may not yield the best results.

To mitigate these potential issues with removing debris-identified velocities from the Doppler spectrum, we also explored the idea of reconstructing a filtered PSD by applying a simple weighting function to the original PSD rather than removing the debris-dominated coefficients entirely. One potential weighting function uses DPSD variance, such that spectral components with low $\sigma^2_{s\rho HV}$ receive higher weight than spectral components with high $\sigma^2_{s\rho HV}$. This method can be approximately represented by

$$sS_{H,new}(v) = \left[1 - \frac{\sigma^2_{s\rho_{HV}}(v)}{max(\sigma^2_{s\rho_{HV}})}\right]^b sS_{H,old}(v), \tag{5.4}$$

where b is a scaling parameter to determine the aggressiveness of the weighting—a higher value of b results in more aggressive suppression of high-$\sigma^2_{s\rho HV}$ spectral components in the original PSD. Since debris-dominated DPSDs show significantly higher $\sigma^2_{s\rho HV}$ than rain-dominated DPSDs, this variance-based weighting function should serve to suppress the debris signal while preserving the rain signal. For this recalculation method, we chose a scaling parameter of $b = 6$. An example of variance-weighted velocity recalculation is shown in Fig. 5.10.

The choice to use $\sigma^2_{s\rho HV}$ as the sole basis of this weighting method was driven by its strength as a discriminator between rain and debris. In this example, the variance-weighted signal reconstruction shows poor performance, as the recalculated velocity still has a bias of 21 m s^{-1}—meaning that variance-based weighting improved the original velocity bias by less than 5 m s^{-1}. Visually, there is little difference between the original and reconstructed Doppler spectra shown in Fig. 5.10b–c. A potential solution to this particular observation could be to increase the scaling parameter b used to re-weight the PSD using Eq. 5.4. However, the effectiveness of this solution may be minimal due to the overall low values of $\sigma^2_{s\rho HV}$ for both rain and debris—the 99.5th percentile $\sigma^2_{s\rho HV}$ for debris (Table 5.2) is only 0.25, and almost the entire $\sigma^2_{s\rho HV}$ spectrum in Fig. 5.10a is below 0.2. Therefore, the PSD weighting scheme in Eq. 5.4 will not result in a significant reduction in the magnitude of debris-dominated signal power contributions unless extremely high scaling parameters are used, which in turn could potentially affect the representativeness of the reconstructed Doppler spectrum. Therefore, despite the demonstrated effectiveness of $\sigma^2_{s\rho HV}$ as a discriminator between rain and debris, its poor performance in this example suggests that its utility as a discriminator is far greater when used in conjunction with other discriminating variables such as $s\hat{\rho}_{HV}$ and $s\hat{Z}_{DR}$ to aid in debris and rain identification.

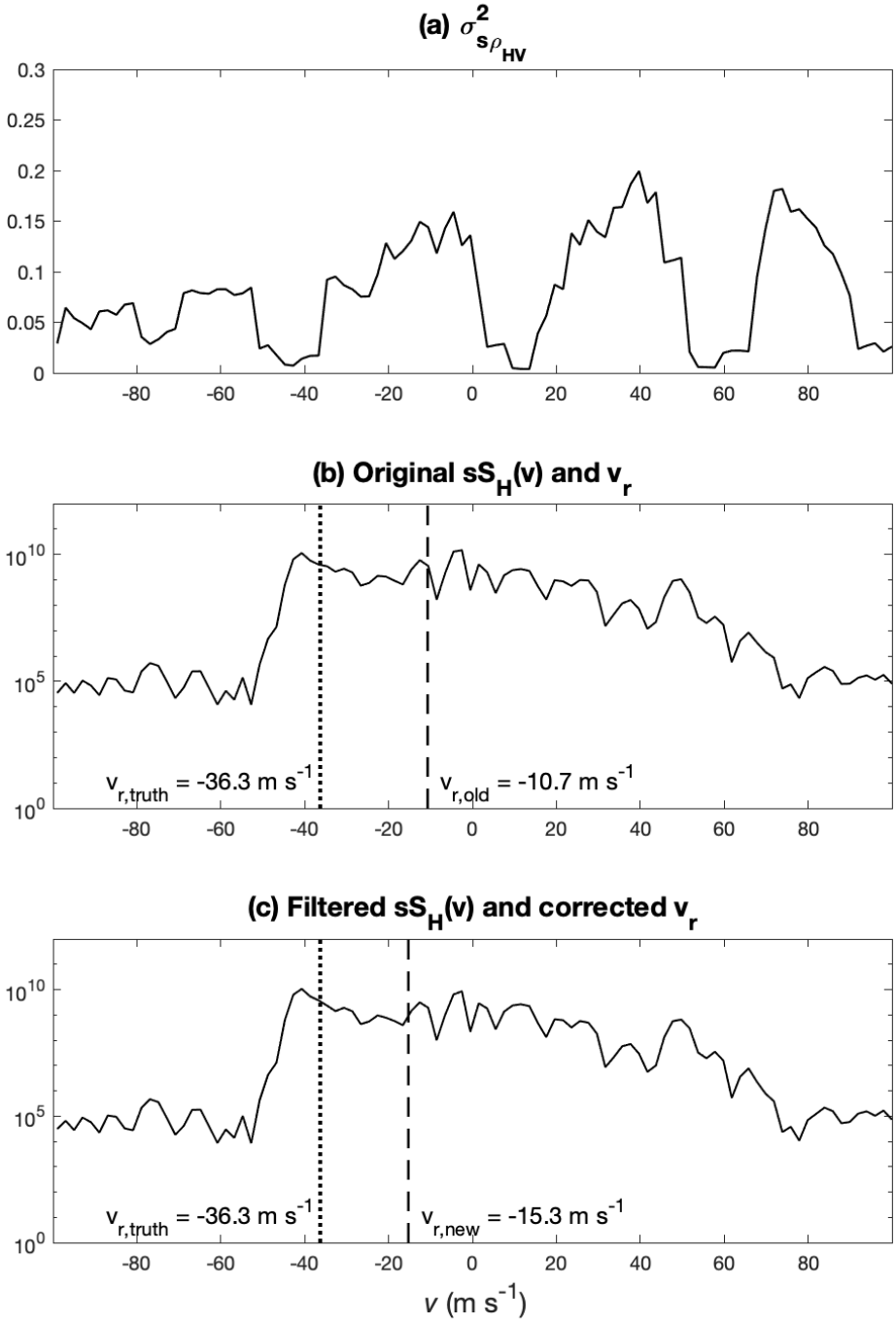

Figure 5.10: (a) $\sigma^2_{s\rho_{HV}}$, (b) original PSD and v_r, and (c) filtered PSD and resulting v_r using Eq. 5.4.

The other potential weighting method we chose to explore utilizes the rain aggregation parameter from the DCA, such that spectral components with high rain probability are weighted more strongly than spectral components with low rain probability. This method can be represented by

$$sS_{H,new}(v) = [A_{rain}(v)]^b sS_{H,old}(v), \tag{5.5}$$

where, as in Eq. 5.4, b is a scaling parameter defining the aggressiveness of the filter. Since the aggregation parameters in this analysis are calculated with weighting coefficients such that the maximum aggregation value for either class is $A_i = 1$, the aggregation values for a spectrum can be utilized directly as a weighting function to suppress debris-dominated signal components in a similar manner as the variance-based weighting scheme. For the aggregation weighting scheme, we chose a scaling parameter of $b = 4$. An example of aggregation-weighted velocity recalculation is shown in Fig. 5.11.

The use of the rain aggregation parameter to reconstruct the Doppler spectrum results in considerable improvement of the velocity bias. The aggregation-based velocity recalculation has a bias of 7.5 m s^{-1}, compared to the original signal velocity bias of 25.6 m s^{-1}. The performance of this method is approximately on par with the performance of the DCA-based correction method in Fig. 5.9, as these two methods result in similar recalculated Doppler velocity estimates. The performance of the rain aggregation parameter in this method provides further support to the previously posited idea that while $\sigma^2_{s\rho HV}$ is the best discriminator between rain and debris out of the three DPSD variables analyzed, its utility is far greater as a partial contributor to the DCA to more robustly identify debris and rain in conjunction with the other DPSD variables. Since the DCA-based and aggregation-based methods both use the

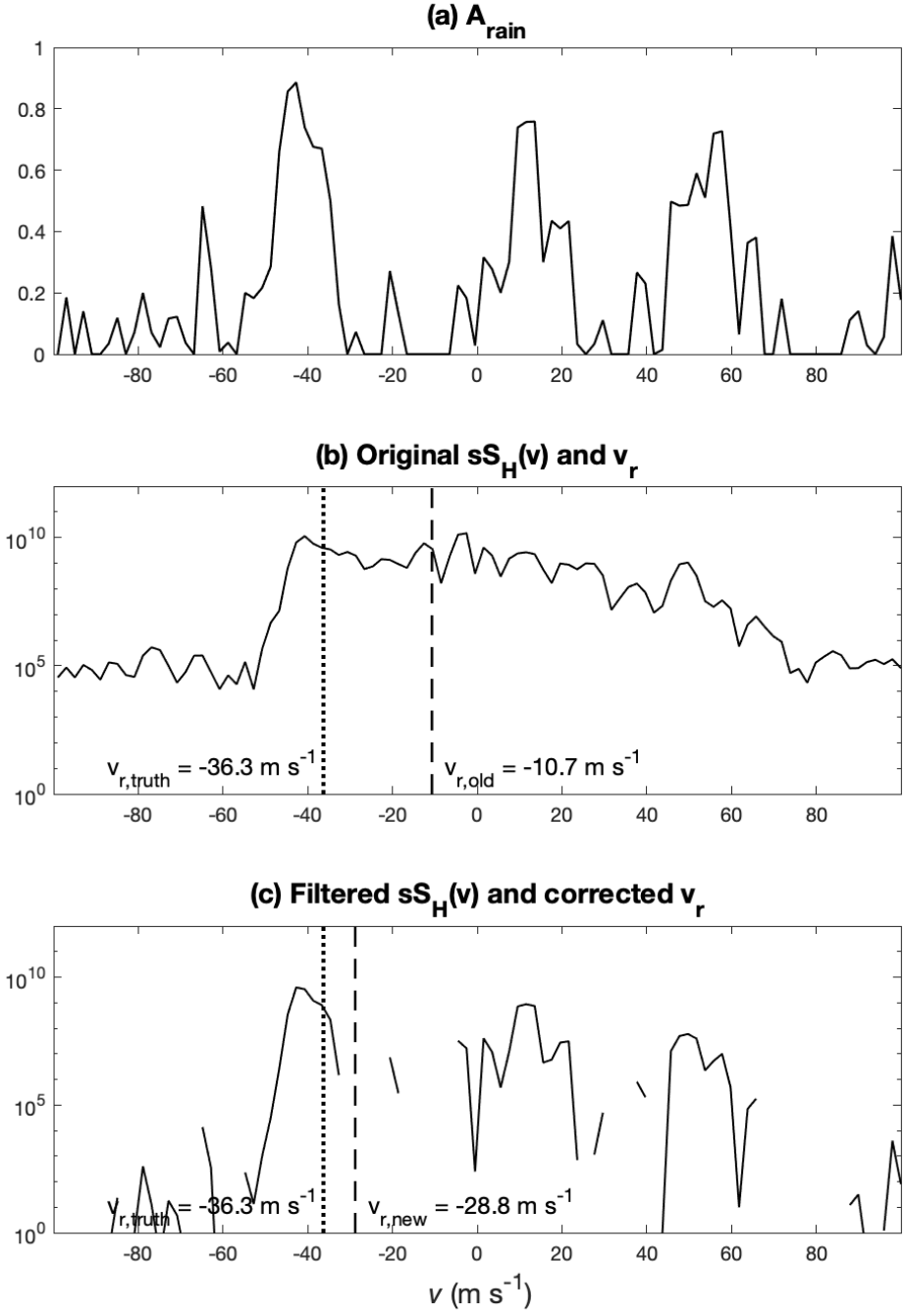

Figure 5.11: (a) A_{rain}, (b) original PSD and v_r, and (c) filtered PSD and resulting v_r using Eq. 5.5.

outputs of the DCA to modify the original PSD while the variance-weighting method uses only $\sigma^2_{s\rho HV}$, the much stronger performance of these two methods justifies the use of fuzzy logic for spectral debris identification and suppression over simpler methods like the variance-weighting method.

5.3.2 Discussion of Velocity Correction Performance

In conjunction with the themes in Chapter 4 of relating velocity bias to debris characteristics, we examine the performance of velocity recalculations for simulations containing varying debris sizes and concentrations to determine if any of these characteristics influence the degree to which the Doppler velocity can be corrected using the DCA. Another variable that may affect the correctability of Doppler velocity is elevation angle, as debris tends to have the highest concentration near the surface, and thus it is likely that the lowest tilts suffer greater velocity bias and spectral debris saturation due to the higher physical concentrations of debris.

To first study the effects of debris concentration on velocity corrections, Fig. 5.12 shows a comparison of the recalculated velocities from each of the three spectral debris suppression techniques for an example spectrum, taken from a simulation with 100,000 wood boards at an elevation angle of 0.5°. The velocity corrections show markedly different behavior between low (10,000) and high (100,000) debris concentrations. While the 10,000 wood board simulation shows improvement in velocity estimates from all three correction methods (Figs. 5.9–5.11), the 100,000 wood board simulation shows little to no improvement from any of the three methods.

Additionally, Fig. 5.12a shows that after applying the DCA filter to remove debris contributions, only a small number of samples remain with which the recalculate the Doppler velocity—perhaps only 5 or 6 data points—illustrating the detrimental

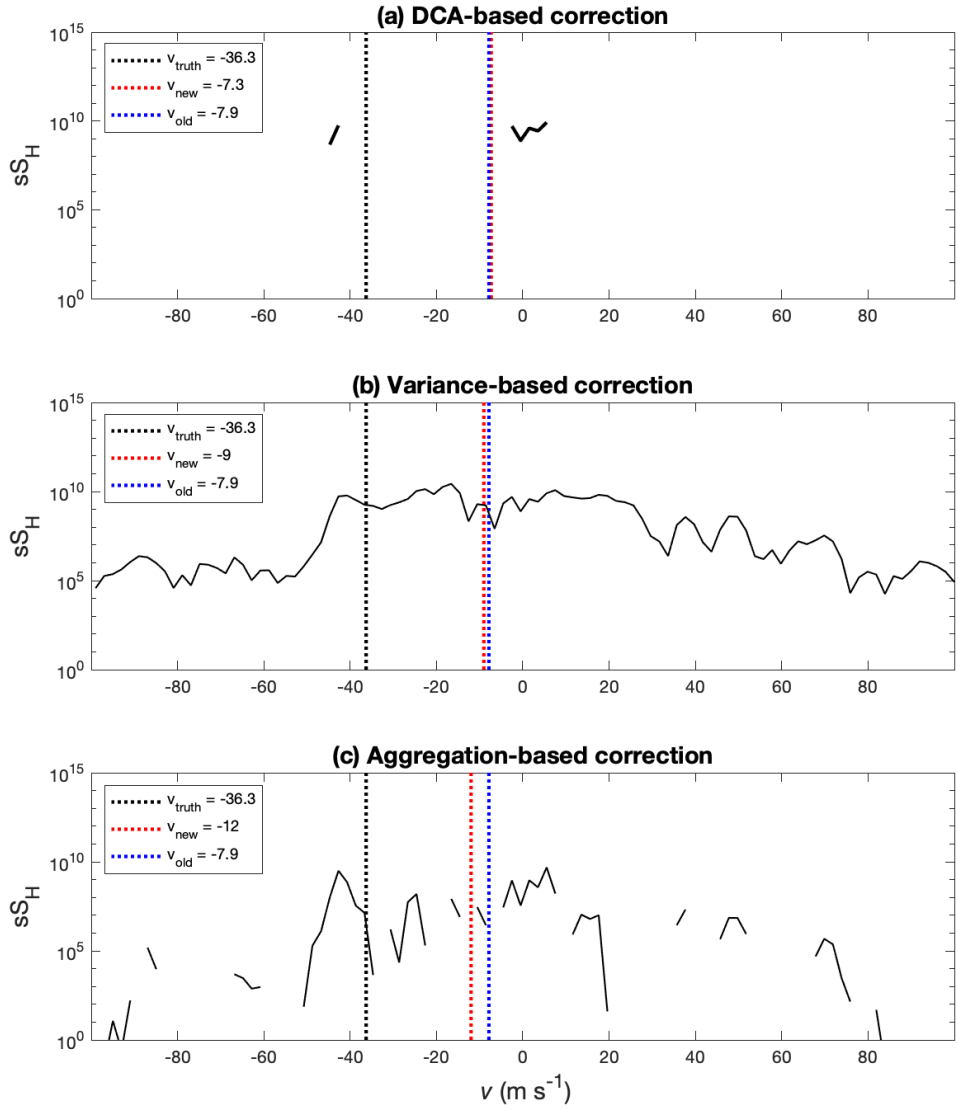

Figure 5.12: Filtered PSDs (solid black) with v_{old}, v_{new}, and v_{truth} with 100,000 wood boards at 0.5°.

impacts of spectral debris saturation. Whereas the DCA is able to identify the true rain peak well enough to improve velocity estimation at low debris concentrations, debris dominates the signal throughout the Doppler spectrum for high concentrations, which results in the rain signal being masked too strongly to be discerned by the DCA. This phenomenon of spectral debris saturation is likely driven by the concentration of debris within a given radar volume—when more debris particles are present within a volume, they are likely to exhibit a wider range of velocities due to the complexity of debris motion and trajectories. Therefore, at high concentrations of debris, it is likely that the rain-dominated signal will be overlapped and masked by higher-signal power debris contributions at the same velocities. Ultimately, the behavior of the velocity corrections for the low-tilt 100,000 wood board simulation demonstrate the detrimental impacts of high debris concentration on the effectiveness of debris suppression and velocity correction by any method, highlighting a major caveat to the use of these algorithms.

To examine the influence of debris size on velocity correction performance, we compare the simulation of 100,000 wood boards to a simulation of 100,000 leaves, both at an elevation angle of 0.5°. In contrast to the poor velocity re-estimations shown for the 100,000 wood boards simulation (Fig. 5.12), Fig. 5.13 at first glance shows excellent performance from not only all three velocity correction methods, but from the original, unfiltered velocity estimate as well. Even at high concentrations, small debris such as leaves induce little velocity bias as demonstrated by this example, wherein the original Doppler velocity estimate was –37.6 m s^{-1} for a true velocity of –36.3 m s^{-1}. The velocity errors associated with small debris are thus much smaller in magnitude than errors induced by larger debris, even before correction methods are applied.

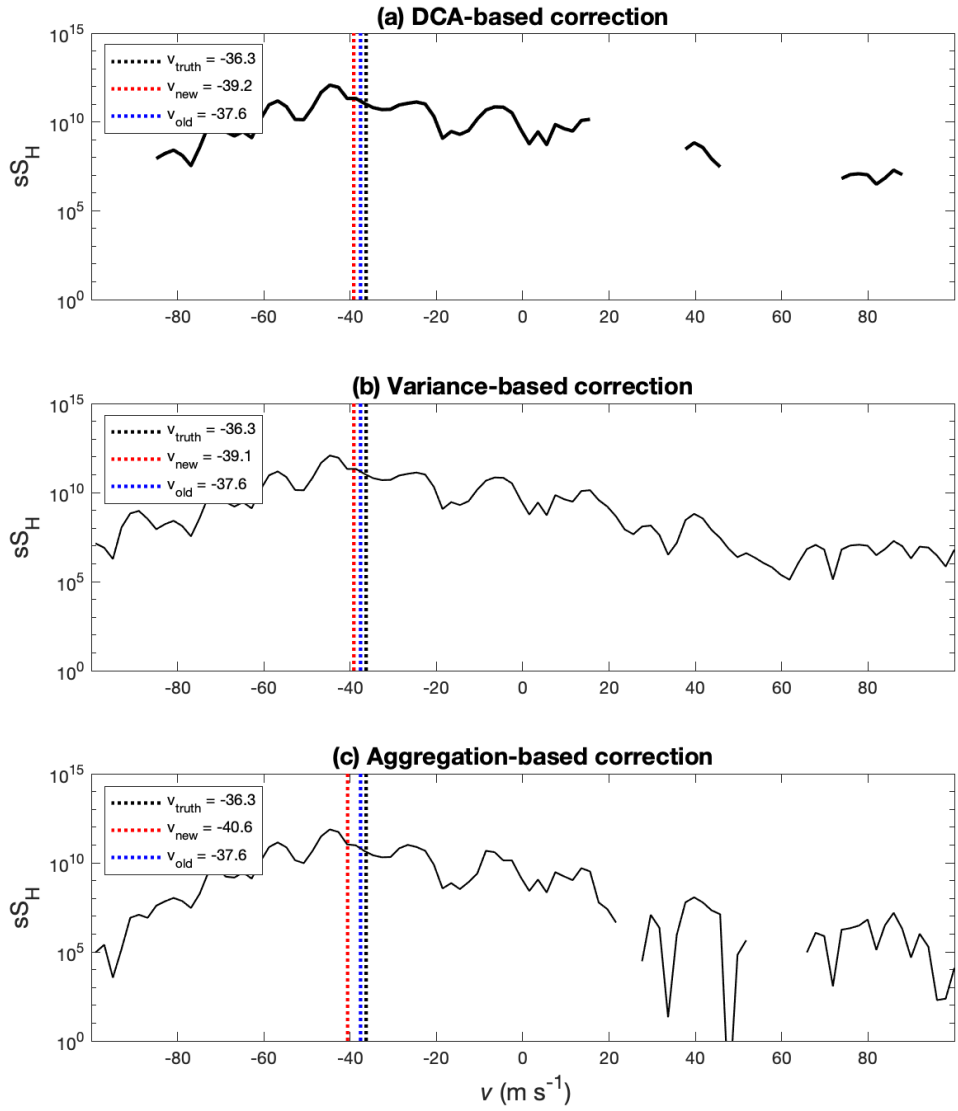

Figure 5.13: As in Fig. 5.12, but for 100,000 leaves at an elevation angle of 0.5°.

Because the uncorrected velocity bias is already relatively low for the leaf case even before correction methods are applied, little improvement is seen in the corrected velocity estimates. The degree to which Doppler velocities are corrected is roughly equivalent for both the 100,000 leaf and 100,000 wood board cases (Figs. 5.13 and 5.12, respectively), suggesting that the overall correctability of Doppler velocity bias is driven primarily by the underlying debris concentration. The dilemma of this behavior is that correction is most urgently needed for large velocity errors, but velocity correction techniques are less effective under the conditions that tend to produce larger velocity errors—i.e., situations with high concentrations of large debris. This bias correctability dilemma and its implications will be explored in greater detail later on in this section.

To study the influence of elevation angle on the performance of velocity corrections, we compare the same simulation with 100,000 wood boards at an elevation angle of 0.5° (Fig. 5.12) to a simulation with the same debris concentration of 100,000 wood boards, but at a higher elevation angle of 2.0° (Fig. 5.14). Ultimately, looking at velocity bias as a function of elevation angle is another way of studying the influence of debris concentration because debris tends to have the highest concentrations in the low levels, falling out of the tornado before reaching higher tilts. Therefore, we posit that the velocity corrections should display better performance at higher tilts with total number of wood boards held constant. In fact, Fig. 5.14 shows general improvement of the velocity estimate after the DCA- and aggregation-based correction methods are applied, with the aggregation-based correction performing the best with a reduction of bias from 29.7 m s^{-1} to 1.7 m s^{-1}. Consistent with the previous examples, the variance-weighted correction method showed the least improvement of the velocity estimate.

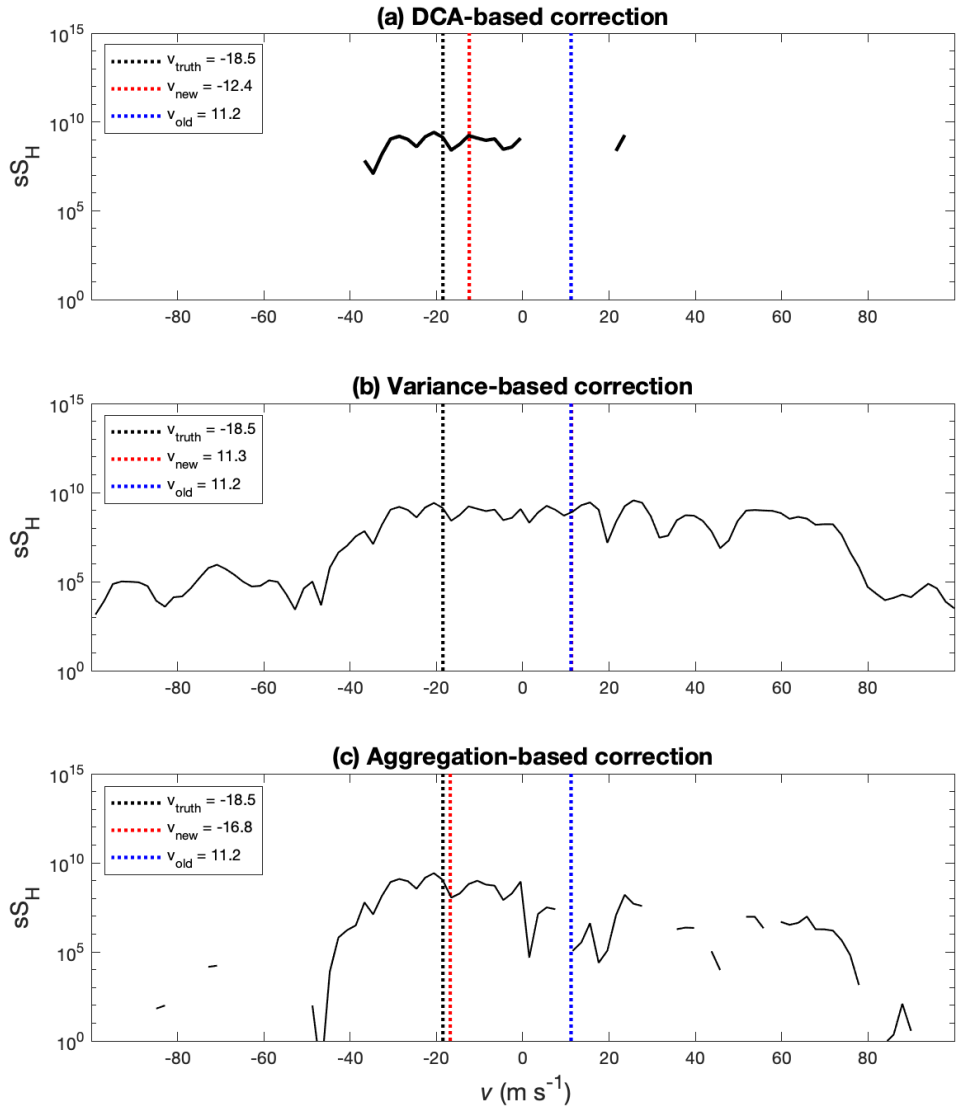

Figure 5.14: As in Fig. 5.12, but for 100,000 wood boards at an elevation angle of 2.0°.

The quality of velocity corrections for simulations both containing 100,000 wood boards is markedly different at 0.5° versus 2.0°. For 100,000 wood boards at 2.0°, the performance of all three correction methods is similar to the performance seen with the 10,000 wood board simulation at 0.5° in that the DCA- and aggregation-based methods perform extremely well, while the variance-based method is ineffective. This behavior provides further support to the hypothesis that debris concentration is a significant driver of the quality and accuracy of velocity estimates, as well as the conclusion that velocity bias associated with low debris concentrations is more easily correctable than bias associated with high debris concentrations due to the effects of spectral saturation as previously discussed.

While examining individual spectra is useful for comparing the performance of velocity correction methods as well as discerning underlying conditions and debris characteristics that can affect the quality of velocity corrections, we can also study and quantify the overall performance of velocity corrections across an entire scan to gain a more comprehensive idea of the effectiveness of these methods under varying conditions. Therefore, the next four figures show analyses of sweep-wide post-correction velocity bias statistics, including the mean post-correction velocity bias (μ) and the interquartile range (IQR), from simulations with 10,000 wood boards at 0.5° (Fig. 5.15), 100,000 wood boards at 0.5° (Fig. 5.16), 100,000 leaves at 0.5° (Fig. 5.17), and 100,000 wood boards at 2.0° (Fig. 5.18).

Overall, based on the post-correction velocity bias statistics shown in the histogram plots in Figs. 5.15–5.18, these sweep-wide analyses display the same patterns as discussed above:

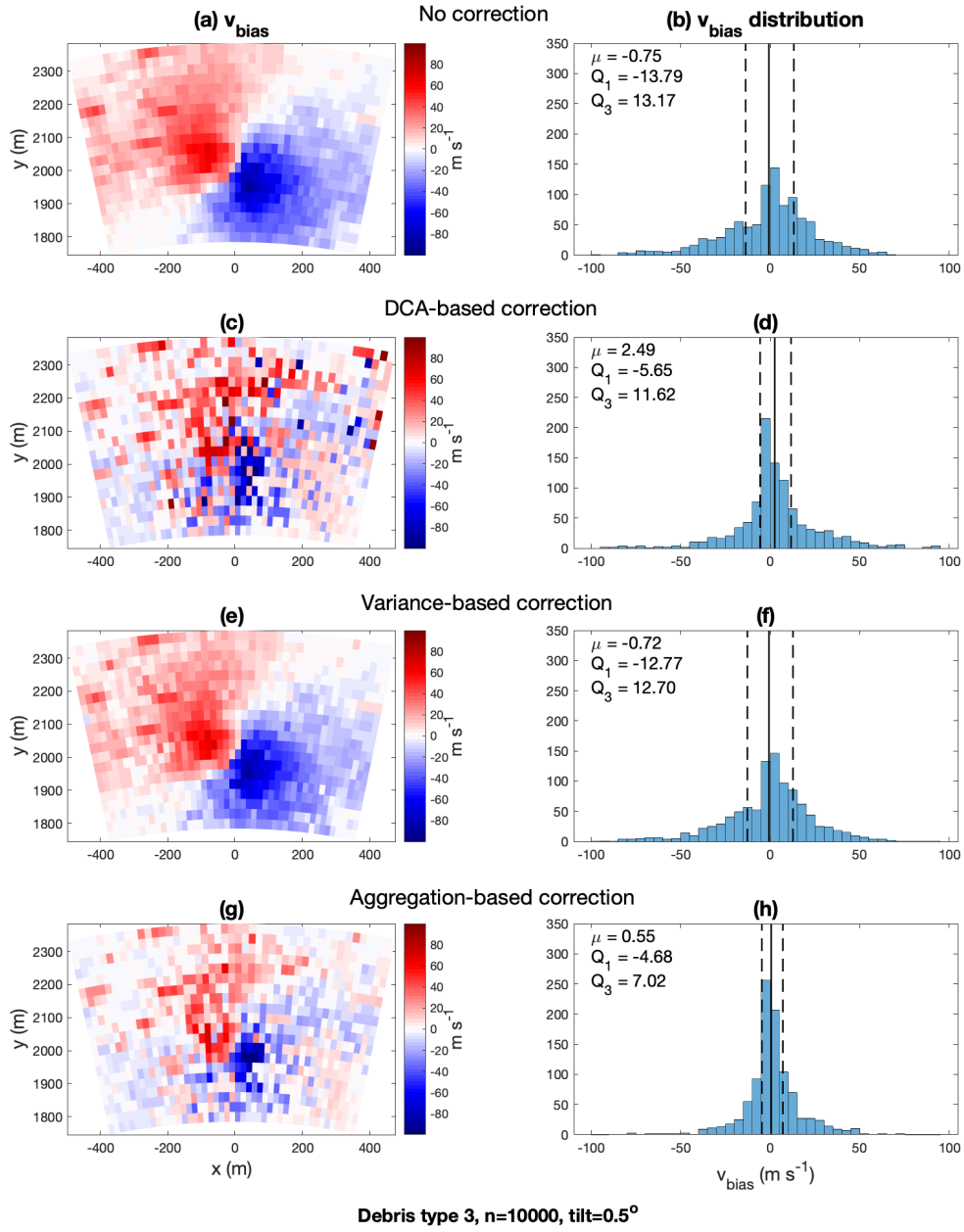

Figure 5.15: (Left)–(right) PPI plots and corresponding histogram number distributions of velocity bias from the (top)–(bottom) uncorrected, DCA-based, variance-based, and aggregation-based velocity estimation methods for a simulation with 10,000 wood boards at an elevation angle of 0.5°. Additionally, the histogram plots are annotated with μ and IQR of the velocity bias distribution.

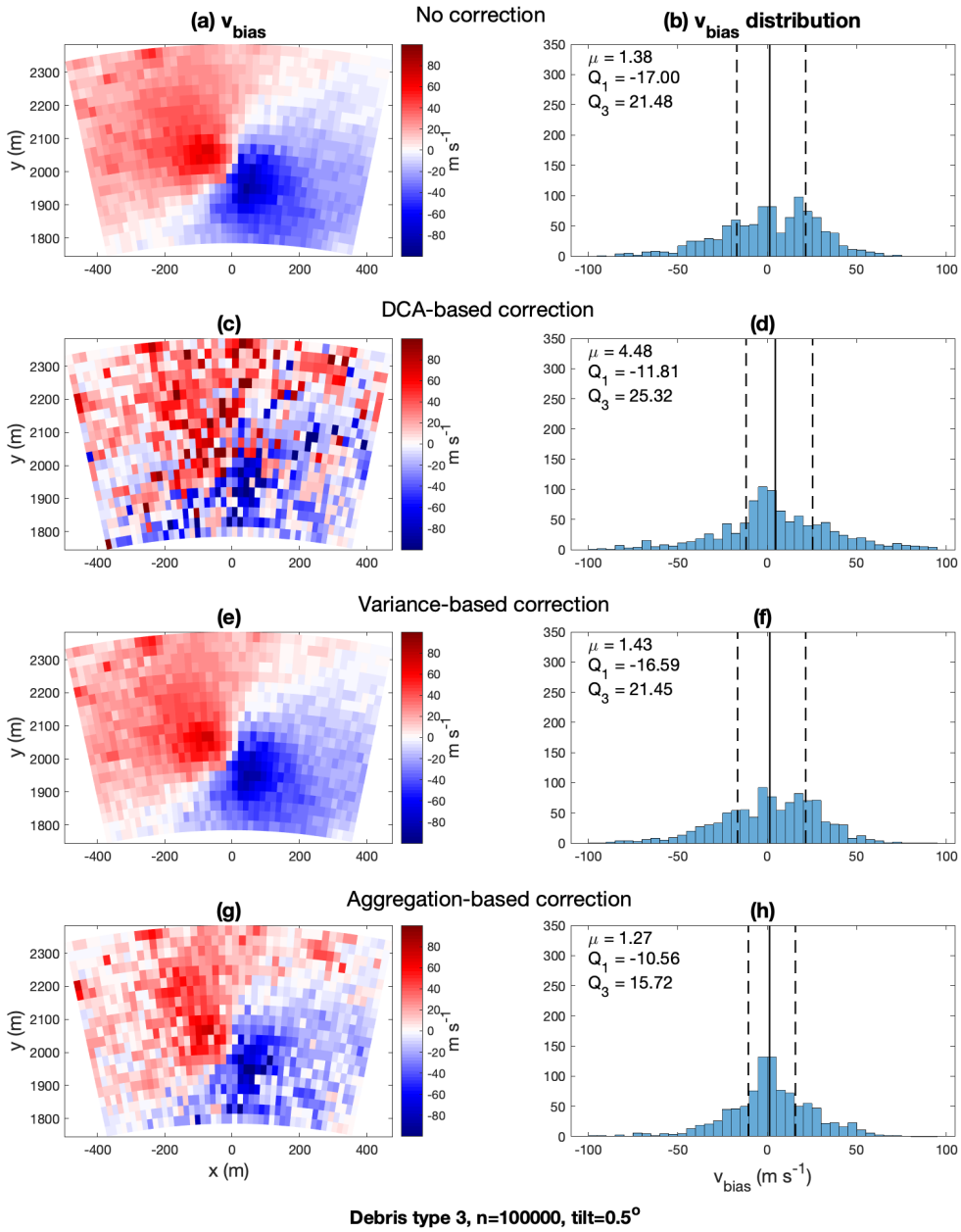

Figure 5.16: As in Fig. 5.15, but for a simulation with 100,000 wood boards at 0.5°.

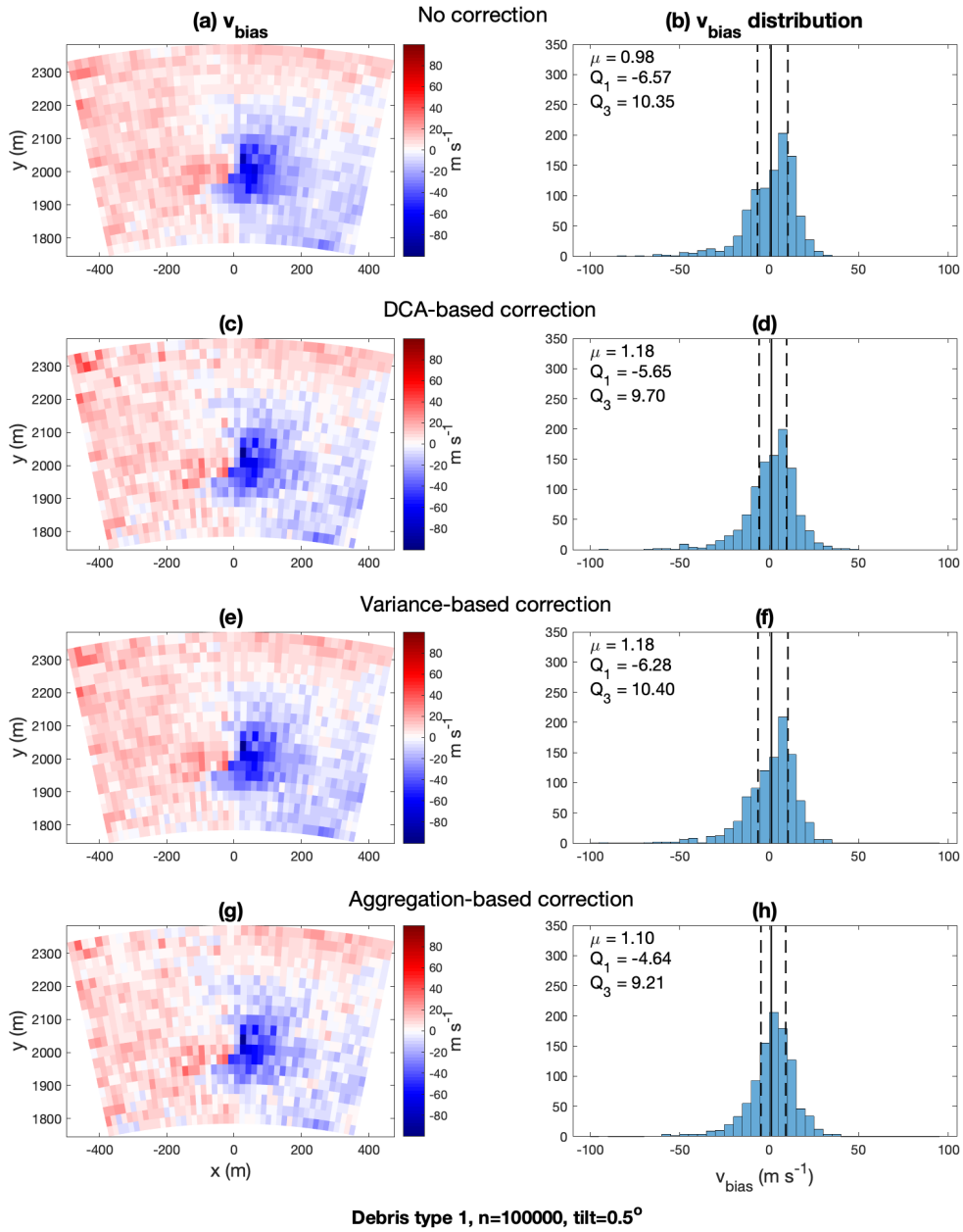

Figure 5.17: As in Fig. 5.15, but for a simulation with 100,000 leaves at 0.5°.

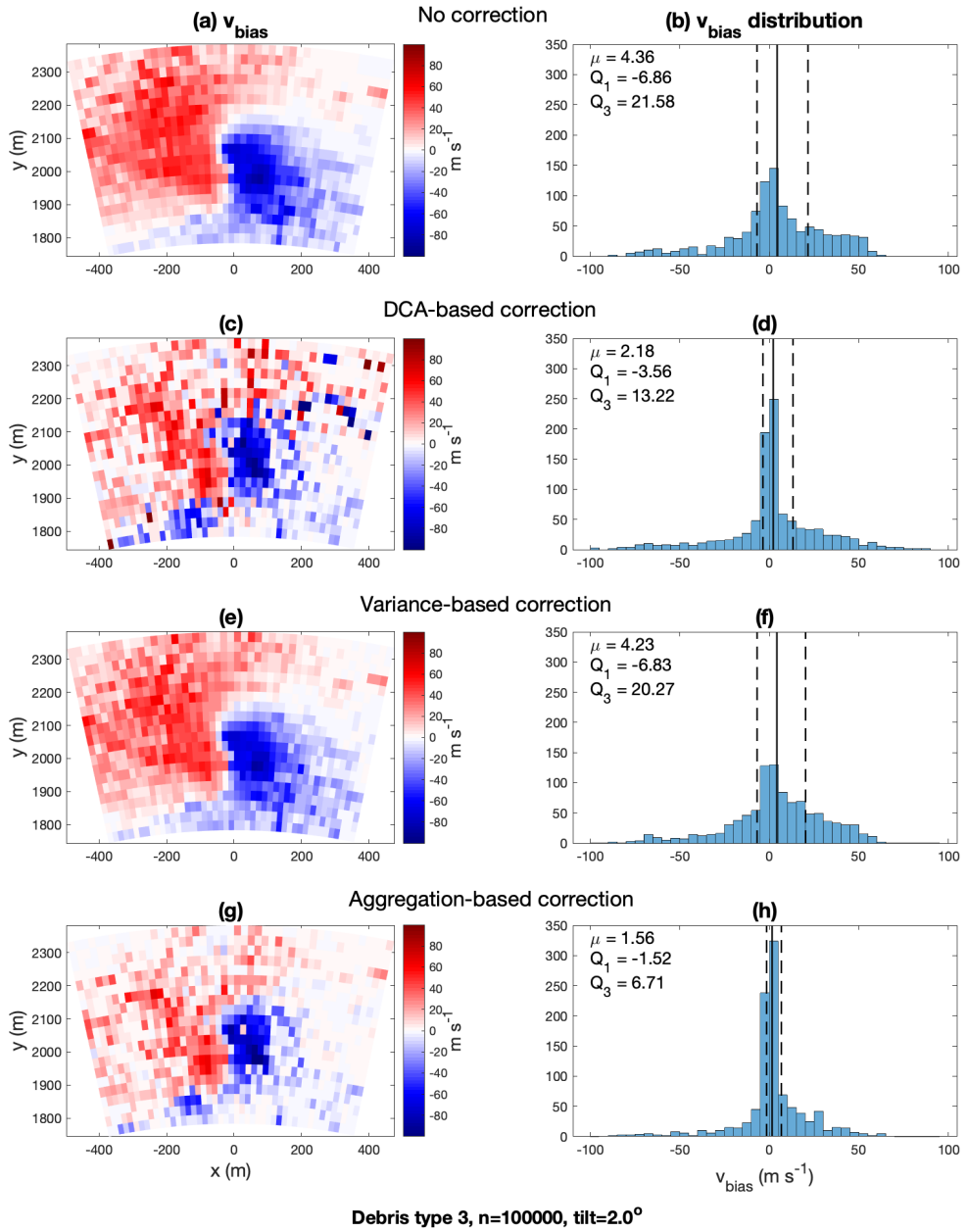

Figure 5.18: As in Fig. 5.15, but for a simulation with 100,000 wood boards at 2.0°.

- Variance-weighted corrections generally perform the worst (i.e., widest IQR), while aggregation-weighted corrections tend to perform the best (i.e., narrowest IQR).

- All velocity correction methods tend to perform better overall for lower debris concentrations, whether that be due to higher tilt or overall lower debris amounts.

- Correction methods for smaller debris (e.g., leaves) result in little improvement of velocity bias to mitigate the already-low bias of the original uncorrected velocity estimate.

In particular, the histograms for the 100,000 wood board and 100,000 leaf simulations at 0.5° (Figs. 5.16 and 5.17, respectively) show similar patterns in velocity bias, with little difference between the distributions of pre-correction and post-correction velocity bias, further illustrating our conclusion that high debris concentration substantially reduces the correctability of Doppler velocity bias, mostly regardless of debris size. Contrarily, the 10,000 wood board simulations at 0.5° and the 100,000 wood board simulation at 2.0° (Figs. 5.15 and 5.18, respectively) show much more significant improvement between the pre- and post-correction velocity bias distributions, indicating that velocity corrections are considerably more effective for lower concentrations of debris.

An important feature in the number distributions of velocity bias is that the mean bias tends to be positive for all three correction methods, a pattern which is present in all four simulations, but is especially severe in the high-concentration wood board simulations. While the mean velocity bias values are relatively small for the 10,000 wood board and 100,000 leaf simulations, they range from 1.3–4.5 m s^{-1} for the 100,000 wood board simulations at 0.5° (Fig. 5.16) and at 2.0° (Fig. 5.18)—simulations for which both velocity bias and debris saturation within the Doppler and polarimetric spectra should be relatively severe. A likely reason for this behavior is that the moving block

variance of $s\hat{\rho}_{HV}$ is calculated starting from the left side of the spectrum, where velocities are negative, with the block moving to the right toward positive velocities. Therefore, spectral transitions from debris to rain will be biased toward debris characteristics as the block moves from high-variance debris-dominated velocities to low-variance rain-dominated velocities—that is, the moving block variance has an "adjustment period" where it lags, in a spectral sense, behind the true variance characteristics, meaning that there will be a rightward bias in the DCA's classification of the rain peak. This is likely a contributing factor to the mean positive bias in post-correction velocities, and the severity of this behavior is likely correlated to the strength of debris saturation; hence, the mean positive bias is more extreme in the 100,000 wood board simulations.

It is important to consider not just the statistical characteristics of velocity corrections, but their spatial characteristics as well. In particular, the spatial distribution of velocity bias in the PPI plots for the leaf and wood board cases are markedly different. In the 100,000 leaf simulation (Fig. 5.17), the post-correction bias is relatively low across the extent of the PPI (except for moderate negative bias near the center of the domain), whereas in the wood board simulations (specifically the low-tilt 10,000 and high-tilt 100,000 wood board cases, shown in Figs. 5.15 and 5.18, respectively), the bias is extremely low around the outer edges of the scan, but remains large near the center of the domain. This can also be seen in the velocity bias histograms in the same figures, where the number distributions of velocity bias for the wood board simulations have longer "tails" than the bias distributions for the 100,000 leaf simulation. Thus, another likely controlling factor of velocity correction quality is radial distance from the tornado.

All four simulations show, to some degree, the largest post-correction velocity bias around the center of the scan domain, near the strongest region of the tornadic core circulation. In a physical tornado, this is not only where the strongest azimuthal wind

speeds are, but also where the majority of debris is lofted, and where the centrifuging of debris is the most severe. The most significant conclusion from these observations and knowledge is that *the strongest winds in a tornado suffer the greatest measurement bias, but are also the most difficult to correct.* This dilemma creates a significant obstacle to radar-based tornado intensity estimation even if velocity correction techniques are implemented, as the true maximum wind speed will likely be masked to a large degree by debris motion.

Additionally, we have found that *the spectral effects of debris are most severe in the lowest levels of the tornado*, where debris tends to have the highest concentration and debris sizes tend to be larger than those aloft. This introduces yet another obstacle to estimating low-level and near-surface tornadic wind speeds, which are already the least-observed winds in a tornado and are vital to studying tornadic structures such as the corner flow region. This work has further demonstrated that *these detrimental effects worsen with larger debris size and concentration.* In a real tornado, the application of these observations leads to the conclusion that velocity bias will likely be more severe and poorly correctable in populated areas, where accurate velocity measurements are the most vital due to the increased human impacts.

Chapter 6

Conclusions

Tornadic debris processes like centrifuging and fallout have significant impacts on Doppler radar observations of tornado wind speeds. While this phenomenon has been previously demonstrated using direct simulations of particle trajectories (e.g., Dowell et al., 2005; Nolan, 2013), there are several novel aspects to this work that have enabled us to study this behavior in greater depth, validate conclusions from these prior studies, and extend them to more fully address the complexity of debris motion and its effects on velocity measurements. This thesis represents the first modeling study to use a radar simulator that incorporates electromagnetic scattering to simulate realistic returns from different particle types. The incorporation of scattering calculations also allows us to easily modify the debris field in order to assess the influence of various debris characteristics, such as size and number concentration, on the simulated radar returns.

In comparing simulated radar measurements of debris and rain in Chapter 4, we have shown that lofted debris is associated with reductions in Δv, a common metric for tornado intensity. Three-dimensional GBVTD winds retrieved from Doppler velocity data also suffer errors related to debris presence—tornado-relative radial velocities are positively biased, azimuthal velocities are underestimated, and vertical velocities are negatively biased. These systematic velocity biases result in overall underestimations of tornadic intensity based on Δv and retrieved azimuthal winds, limiting the value of relating observed tornado damage and EF-scale ratings to measured Doppler velocities.

They also result in erroneous inferences of tornadic structure via the radial and vertical winds, which can show anomalous low-level outflow and axial downdraft as a result of error integration.

The Δv and GBVTD analyses presented in Chapter 4 illustrate how the severity of velocity bias is related to the physical characteristics of the debris field. *The magnitude of systematic velocity bias due to debris centrifuging is positively correlated with both debris size and concentration*, with debris concentration in particular having substantial influence on Doppler velocity bias. In the presence of low concentrations of debris, rain has relatively large influence within the radar signal, resulting in low Doppler velocity bias; as debris concentration rises, so does its relative influence in the radar signal, leading to greater velocity bias. Another common feature of the Δv and GBVTD analyses in Chapter 4 is that *velocity bias is largest in the low levels*. This pattern is ultimately a manifestation of the correlation between velocity bias magnitude and debris concentration—since debris has the highest concentration close to the surface, velocity bias is also largest near the surface. The overall maximization of Doppler velocity bias close to the surface means that radar-based tornado damage prediction and intensity estimation likely suffer from substantial inaccuracy.

The latter half of Chapter 4 begins to address our second overarching research objective: the estimation and correction of debris-induced Doppler velocity errors from radar measurements. In the bulk moment-based relationships discussed, velocity bias magnitude is correlated with corresponding values of Z_H, Z_{DR}, and ρ_{HV} based on the knowledge that debris has distinctive influences on both Doppler velocity and polarimetric measurements. These analyses show that in general, large velocity bias is generally associated with high Z_H, negative Z_{DR}, and low ρ_{HV}—the defining polarimetric characteristics of a TDS, as discussed in Chapter 1. As debris size and concentration

increase, the values of the polarimetric variables become more TDS-like (i.e., Z_H further increases while Z_{DR} and ρ_{HV} further decrease), and the associated velocity errors increase in both magnitude and spread. Overall, these results show potentially useful relationships between polarimetric variables and velocity bias behavior.

The complexity and nonlinearity of the relationships between polarimetric variables, debris characteristics, and velocity bias makes it difficult to envision a moment-based bias estimation technique with enough precision to be robust. However, rough estimates of bias from polarimetric variables may still be possible. These relationships could be used to establish measurement errors in wind statistics from tornadoes and determine error bars on plots of velocity measurements and statistics. They could also be useful in making qualitative inferences about the physical characteristics of the debris field. With more detailed quantification and analysis of the relationships between velocity bias, debris size and concentration, and polarimetric variables, these results could be used operationally to infer relative velocity bias severity, and potentially damage severity using corrected velocity measurements, based on the polarimetric characteristics of TDSs. Presently, no methods exist to estimate the degree of debris-related bias except those based on Rayleigh scattering (e.g., Wakimoto et al., 2012).

Chapter 5 presents an alternative, more precise spectral method for Doppler velocity bias correction using DPSD estimation and spectral scatterer classification. Since debris and rain move at different velocities and have unique polarimetric characteristics, we sought to develop an algorithm to identify spectral variations in the polarimetric characteristics of signals in order to identify and filter debris motion from Doppler spectra. Debris identification and filtering is accomplished by developing a debris classification algorithm (DCA), which classifies velocities in a spectrum as either debris or rain motion based on the associated DPSD characteristics. Using the

resulting classifications, debris motion is filtered from the spectrum or suppressed using a spectral weighting function, and the Doppler velocity is recalculated from the modified spectra. Three different PSD filtering techniques for Doppler velocity recalculation were developed and evaluated: a DCA classification-based filter, a $s\hat{\rho}_{HV}$ variance-based weighting filter, and an aggregation parameter-based weighting filter. Of these three techniques, the DCA- and aggregation-based methods show the overall best performance in Doppler velocity bias mitigation, justifying the use of multiple predictor variables and fuzzy logic classification over simpler methods.

Overall, the spectral techniques for velocity bias correction show promising performance, especially at lower debris concentrations, higher elevation angles, and around the outer circulation of the tornado. When the DCA is able to detect the rain signal, the post-correction velocity bias is consistently almost entirely eliminated (as shown by the enhanced peaks at 0 m s^{-1} in the histograms in Figs. 5.15–5.18). However, these methods also all displayed similar shortcomings associated with the complex behavior of debris. Velocity correction was least effective where the tornadic circulation was strongest and in the low levels. This behavior is representative of yet another manifestation of the relationship between Doppler velocity bias and debris concentration. As discussed in Chapter 3.1, the amount of debris lofted in SimRadar is proportional to the horizontal wind speed. As a result, and because debris is the most highly concentrated near the surface, the locations where velocity correction is least effective are the locations where debris concentration is the highest (i.e., where velocity bias magnitude is the largest), though it is unclear what the realistic upper bound is for the maximum number of debris in a tornado. Even so, we can conclude that *the most biased velocity measurements are also the most difficult to correct.*

The substantial influence of debris concentration on the accuracy and quality of both velocity estimates and corrections can be attributed to the phenomenon of "spectral saturation" or "debris saturation." As larger amounts of debris are lofted into a tornado, the motions observed by radar become more variable due to the irregularity of debris size and shape, causing increased overlap between rain- and debris-dominated spectral peaks. Significant spectral overlap between rain and debris leads to masking of the rain signal by debris—i.e., the spectrum is "saturated" with debris-dominated contributions. This masking and spectral saturation by debris then causes the DCA to fail as it becomes unable to separate the rain signal from the overlapping debris signal, leading to the misclassification of the true rain peak as debris. The effects of spectral saturation from debris are particularly severe in these results, as S-band wavelengths suffer greater contamination by debris motion than shorter wavelengths (Bodine et al., 2016a). Therefore, this technique may be more robust at shorter wavelengths such as X-band, where the signal contributions of debris are relatively weaker even at high concentrations. However, radar sampling factors such as low PRT used to mitigate second-trip echoes could make it more difficult to mitigate the effects of spectral saturation via the reduction of the Nyquist velocity, thereby increasing the degree of velocity aliasing within the spectra.

Future work on these topics will likely have some focus on improving these spectral Doppler velocity correction techniques. One potential route to accomplish this is by modifying and optimizing the existing DCA and PSD filtering algorithms. First, the current DCA membership function thresholds were determined using percentiles, but this method may not result in the most optimal threshold values. Some membership thresholds—particularly the ones that have already been chosen to deviate from the standard 0.5–20–80–99.5 percentile threshold pattern—may perform better with empirically determined values due to the unique behavior of DPSD distributions.

We have also considered including additional predictor variables to the DCA: $\sigma^2_{sZ_{DR}}$, or the moving block variance of $s\hat{Z}_{DR}$, and spectral SNR. $\sigma^2_{sZ_{DR}}$ shows similar behavior to $\sigma^2_{s\rho_{HV}}$ in that rain is associated with extremely low spectral variance while debris is associated with large spectral variance, so the addition of $\sigma^2_{sZ_{DR}}$ as a predictor variable in the DCA could further improve differentiation between rain and debris. SNR as a predictor variable, on the other hand, would be used to differentiate between signal and noise power such that noise-dominated power would be classified as rain instead of debris. This would not directly improve the DCA classification of spectral peaks, but would instead improve the robustness of the DCA-based PSD filter by increasing the number of points retained from the original PSD without detrimentally influencing the velocity re-estimate. The other two velocity recalculation methods—the variance- and aggregation-based weighting filters—could be improved by testing the sensitivity of the velocity correction to the value of the scaling parameter b and determining the optimal value for robust velocity bias correction.

None of the above improvements, however, will be able to effectively mitigate the vulnerability of the DCA to spectral debris saturation. This vulnerability to spectral overlap between rain and debris is inherent to the use of DPSDs. A potential, less conventional way to overcome this limitation would be to use linear or circular depolarization. Debris should induce a large linear depolarization ratio (LDR), while raindrops would be associated with significantly lower LDR. Taking a cross-channel LDR difference may make it possible to separate overlapping rain and debris velocities. Meanwhile, a property of circularly polarized waves is that when they encounter a scatterer, they reflect back to the source with components polarized in both channels. The exception to this behavior is rain drops, which are roughly spherical scatterers with approximately uniform water composition. If circular wave encounters a rain drop, it will return to the radar with a component in only in the opposite channel

from the original transmitted wave, rather than in both channels. The major advantage thus offered by circular or linear depolarization is *the ability to separate the power contributions of debris and rain even if their velocities overlap*, thereby overcoming the limitations associated with spectral saturation from debris in DPSDs.

Our biggest focus in continuing to develop and improve these algorithms will be to test them with observational radar data. While the simulations used throughout this thesis are physically realistic, they are still inherently approximations of reality, and there may be unanticipated differences between the DPSD estimates from SimRadar simulations and real DPSD estimates from observational data, especially given that the simulations were performed using an S-band wavelength while research radars tend to operate at shorter wavelengths. Therefore, we intend to apply the algorithms discussed throughout this thesis to existing high-resolution radar observations of tornadoes, such as those from the Rapid-Scanning X-band Polarimetric mobile radar (RaXPol; Pazmany et al., 2013), the University of Oklahoma PX-1000 mobile radar, and the KOUN fixed Doppler radar. Phased-array radars—such as the upcoming Polarimetric Atmospheric Imaging Radar (PAIR; Salazar et al., 2019) or Horus (Fulton et al., 2020)—would also be well-suited to testing these techniques because they can collect extremely rapid volumetric observations, and can easily switch between polarization modes for testing a future linear or circular depolarization-based method.

Testing the velocity correction algorithms on observational data could help us identify the extent to which spectral debris saturation is an issue, as well as the extent to which spectral polarimetric behavior and velocity correction effectiveness vary across different wavelengths. Based on the performance of the velocity correction algorithms on observational data sets, the ideal outcome of this work would be the development of an operational Doppler velocity correction algorithm. Due to the nature of tornado observations, such a product would be primarily applicable to mobile research

radar systems. Robust correction of debris-induced bias in mobile radar velocity measurements would not only provide the necessary foundation for accurate estimation of tornado intensity and damage potential, but would also serve to improve the accuracy and certainty of scientific understanding of tornadoes from radar observations. The radial and vertical winds of tornadoes are highly uncertain velocity components—with debris centrifuging correction, the measurements of these components, along with our conceptual models of the structure and vertical profile of azimuthal winds in a tornado, could be immensely improved.

Reference List

Bachmann, S., and D. S. Zrnić, 2007: Spectral density of polarimetric variables separating biological scatterers in the VAD display. *J. Atmos. Oceanic Technol.*, **24**, 1186–1198, doi:10.1175/JTECH2043.1.

Batt, R. G., M. P. Petach, S. A. Peabody II, and R. R. Batt, 1999: Boundary layer entrainment of sand-sized particles at high speed. *J. Fluid Mech.*, **392**, 335–360, doi:10.1017/S0022112099005510.

Bluestein, H. B., 2013: *Severe Convective Storms and Tornadoes: Observations and Dynamics*. Springer, 456 pp.

Bluestein, H. B., M. M. French, R. L. Tanamachi, S. Frasier, K. Hardwick, F. Junyent, and A. L. Pazmany, 2007: Close-range observations of tornadoes in supercells made with a dual-polarization, X-band, mobile Doppler radar. *Mon. Wea. Rev.*, **135**, 1522–1543, doi:10.1175/MWR3349.1.

Bluestein, H. B., W.-C. Lee, M. Bell, C. C. Weiss, and A. L. Pazmany, 2003: Mobile Doppler radar observations of a tornado in a supercell near Bassett, Nebraska, on 5 June 1999. Part II: Tornado-vortex structure. *Mon. Wea. Rev.*, **131**, 2968–2984.

Bluestein, H. B., K. J. Thiem, J. C. Snyder, and J. B. Houser, 2018: The multiple-vortex structure of the El Reno, Oklahoma, tornado on 31 May 2013. *Mon. Wea. Rev.*, **146**, 2483–2502, doi:10.1175/MWR-D-18-0073.1.

Bluestein, H. B., C. C. Weiss, and A. L. Pazmany, 2004: The vertical structure of a tornado near Happy, Texas, on 5 May 2002: High-resolution, mobile, W-band, Doppler radar observations. *Mon. Wea. Rev.*, **132**, 2325–2337.

Bodine, D. J., M. R. Kumjian, R. D. Palmer, P. L. Heinselman, and A. V. Ryzhkov, 2013: Tornado damage estimation using polarimetric radar. *Wea. Forecasting*, **28**, 139–158, doi:10.1175/WAF-D-11-00158.1.

Bodine, D. J., M. R. Kumjian, A. J. Smith, R. D. Palmer, A. V. Ryzhkov, and P. L. Heinselman, 2011: High-resolution polarimetric observations of an EF-4 tornado on 10 May 2010 from OU-PRIME. *35th Conf. on Radar Meteorology*, Amer. Meteor. Soc., Pittsburgh, PA, 4B.3, https://ams.confex.com/ams/35Radar/webprogram/Paper191661.html.

Bodine, D. J., T. Maruyama, R. D. Palmer, C. J. Fulton, H. B. Bluestein, and D. C. Lewellen, 2016a: Sensitivity of tornado dynamics to soil debris loading. *J. Atmos. Sci.*, **73**, 2783–2801, doi:10.1175/JAS-D-15-0188.1.

Bodine, D. J., R. D. Palmer, T. Maruyama, C. J. Fulton, Y. Zhu, and B. L. Cheong, 2016b: Simulated frequency dependence of radar observations of tornadoes. *J. Atmos. Oceanic Technol.*, **33**, 1825–1842, doi:10.1175/JTECH-D-15-0120.1.

Bodine, D. J., R. D. Palmer, and G. Zhang, 2014: Dual-wavelength polarimetric radar analyses of tornadic debris signatures. *J. Appl. Meteor. Climatol.*, **53**, 242–261, doi:10.1175/JAMC-D-13-0189.1.

Bringi, V. N., and V. Chandrasekar, 2001: *Polarimetric Doppler Weather Radar: Principles and Applications*. Cambridge University Press, 636 pp.

Brown, R. A., L. R. Lemon, and D. W. Burgess, 1978: Tornado detection by pulsed Doppler radar. *Mon. Wea. Rev.*, **106**, 29–38.

Changnon, S. A., 2009: Tornado losses in the United States. *Nat. Hazards Rev.*, **10**, 145–150, doi:10.1061/(ASCE)1527-6988(2009)10:4(145).

Cheong, B. L., D. J. Bodine, C. J. Fulton, S. M. Torres, T. Maruyama, and R. D. Palmer, 2017: SimRadar: A polarimetric radar time-series simulator for tornadic debris studies. *IEEE Trans. Geosci. Remote Sens.*, **55**, 2858–2870, doi:10.1109/TGRS.2017.2655363.

Cheong, B. L., R. D. Palmer, and M. Xue, 2008: A time series weather radar simulator based on high-resolution atmospheric models. *J. Atmos. Oceanic Technol.*, **25**, 230–243, doi:10.1175/2007JTECHA923.1.

Church, C., D. W. Burgess, C. A. Doswell III, and R. Davies-Jones, Eds., 1993: *The Tornado: Its Structure, Dynamics, Prediction, and Hazards*. Amer. Geophys. Union.

Church, C. R., J. T. Snow, G. L. Baker, and E. M. Agee, 1979: Characteristics of tornado-like vortices as a function of swirl ratio: A laboratory investigation. *J. Atmos. Sci.*, **36**, 1755–1776.

Davies-Jones, R., R. J. Trapp, and H. B. Bluestein, 2001: Tornadoes and tornadic storms. *Severe Convective Storms*, I. C. A. Doswell, Ed., Amer. Meteor. Soc., 167–222.

Davies-Jones, R. P., 1973: The dependence of core radius on swirl ratio in a tornado simulator. *J. Atmos. Sci.*, **30**, 1427–1430.

Doviak, R. J., V. Bringi, A. Ryzhkov, A. Zahrai, and D. S. Zrnić, 2000: Considerations for polarimetric upgrades to operational WSR-88D radars. *J. Atmos. Oceanic Technol.*, **17**, 257–278.

Doviak, R. J., and D. S. Zrnić, 1993: *Doppler Radar and Weather Observations*. 2nd ed., Dover Publications, 592 pp.

Dowell, D. C., C. R. Alexander, J. M. Wurman, and L. J. Wicker, 2005: Centrifuging of hydrometeors and debris in tornadoes: Radar-reflectivity patterns and wind-measurement errors. *Mon. Wea. Rev.*, **133**, 1501–1524, doi:10.1175/MWR2934.1.

Edwards, R., J. G. LaDue, J. T. Ferree, K. Scharfenberg, C. Maier, and W. L. Coulbourne, 2013: Tornado intensity estimation: Past, present, and future. *Bull. Amer. Meteor. Soc.*, **94**, 641–653, doi:10.1175/BAMS-D-11-00006.1.

Fujita, T. T., 1971: Proposed characterization of tornadoes and hurricanes by area and intensity. SMRP Res. Pap. 91, University of Chicago, 42 pp.

Fulton, C., R. Palmer, M. Yeary, J. Salazar, H. Sigmarsson, M. Weber, and A. Hedden, 2020: Horus: A testbed for fully digital phased array radars. *Microwave J.*, **63**, 20–36.

Gibbs, J. G., 2016: A skill assessment of techniques for real-time diagnosis and short-term prediction of tornado intensity using the WSR-88D. *J. Operational Meteor.*, **4**, 170–181, doi:10.15191/nwajom.2016.0413.

Gong, B., 2006: Large-eddy simulation of the effects of debris on tornado dynamics. Ph.D. thesis, West Virginia University, 187 pp.

Gong, B., D. C. Lewellen, and W. S. Lewellen, 2006: Effects of fine-scale debris on different tornado corner flows. *23rd Conf. on Severe Local Storms*, Amer. Meteor. Soc., St. Louis, MO, P10.3, https://ams.confex.com/ams/23SLS/techprogram/paper_115317.htm.

Griffin, C. B., D. J. Bodine, and R. D. Palmer, 2017: Kinematic and polarimetric radar observations of the 10 May 2010, Moore-Choctaw, Oklahoma, tornadic debris signature. *Mon. Wea. Rev.*, **145**, 2723–2741, doi:10.1175/MWR-D-16-0344.1.

Janssen, L., and G. Van Der Spek, 1985: The shape of Doppler spectra from precipitation. *IEEE Trans. Aerosp. Electron. Syst.*, **21**, 208–219, doi:10.1109/TAES.1985.310618.

Kingfield, D. M., and J. G. LaDue, 2015: The relationship between automated low-level velocity calculations from the WSR-88D and maximum tornado intensity determined from damage surveys. *Wea. Forecasting*, **30**, 1125–1139, doi:10.1175/WAF-D-14-00096.1.

Kosiba, K. A., R. J. Trapp, and J. M. Wurman, 2008: An analysis of the axisymmetric three-dimensional low level wind field in a tornado using mobile radar observations. *Geophys. Res. Lett.*, **35**, L05 805, doi:10.1029/2007GL031851.

Kosiba, K. A., and J. M. Wurman, 2010: The three-dimensional axisymmetric wind field structure of the Spencer, South Dakota, 1998 tornado. *J. Atmos. Sci.*, **67**, 3074–3083, doi:10.1175/2010JAS3416.1.

Kosiba, K. A., and J. M. Wurman, 2013: The three-dimensional structure and evolution of a tornado boundary layer. *Wea. Forecasting*, **28**, 1552–1561, doi: 10.1175/WAF-D-13-00070.1.

Kumjian, M. R., and A. V. Ryzhkov, 2008: Polarimetric signatures in supercell thunderstorms. *J. Appl. Meteor. Climatol.*, **47**, 1940–1961, doi:10.1175/2007JAMC1874.1.

LaDue, J. G., K. L. Ortega, B. R. Smith, G. J. Stumpf, and D. M. Kingfield, 2012: A comparison of high resolution tornado surveys to Doppler radar observed vortex parameters: 2011–2012 case studies. *26th Conf. on Severe Local Storms*, Amer. Meteor. Soc., Nashville, TN, 6.3, https://ams.confex.com/ams/26SLS/webprogram/Paper212627.html.

Lee, W.-C., B. J.-D. Jou, P.-L. Chang, and S.-M. Deng, 1999: Tropical cyclone kinematic structure retrieved from single-Doppler radar observations. Part I: Interpretation of Doppler velocity patterns and the GBVTD technique. *Mon. Wea. Rev.*, **127**, 2419–2439.

Lee, W.-C., and J. M. Wurman, 2005: Diagnosed three-dimensional axisymmetric structure of the Mulhall tornado on 3 May 1999. *J. Atmos. Sci.*, **62**, 2373–2393, doi:10.1175/JAS3489.1.

Lewellen, D. C., B. Gong, and W. S. Lewellen, 2004: Effects of debris on near-surface tornado dynamics. *22nd Conf. on Severe Local Storms*, Amer. Meteor. Soc., Hyannis, MA, 15.5, https://ams.confex.com/ams/11aram22sls/techprogram/paper_81449.htm.

Lewellen, D. C., B. Gong, and W. S. Lewellen, 2008: Effects of finescale debris on near-surface tornado dynamics. *J. Atmos. Sci.*, **65**, 3247–3262, doi:10.1175/2008JAS2686.1.

Lewellen, D. C., and W. S. Lewellen, 2007: Near-surface vortex intensification through corner flow collapse. *J. Atmos. Sci.*, **64**, 2195–2209, doi:10.1175/JAS3966.1.

Lewellen, D. C., W. S. Lewellen, and J. Xia, 2000: The influence of a local swirl ratio on tornado intensification near the surface. *J. Atmos. Sci.*, **57**, 527–544.

Lewellen, W. S., D. C. Lewellen, and R. I. Sykes, 1997: Large-eddy simulation of a tornado's interaction with the surface. *J. Atmos. Sci.*, **54**, 581–605.

Lujan, J., 2016: Radar cross section analysis of tornadic debris. M.S. thesis, School of Electrical and Computer Engineering, University of Oklahoma, 128 pp.

Magsig, M. A., and J. T. Snow, 1998: Long-distance debris transport by tornadic thunderstorms. Part I: The 7 May 1995 supercell thunderstorm. *Mon. Wea. Rev.*, **126**, 1430–1449.

Markowski, P., and Y. Richardson, 2010: *Mesoscale Meteorology in Midlatitudes*. Wiley-Blackwell, 430 pp.

Maruyama, T., 2011: Simulation of flying debris using a numerically generated tornado-like vortex. *J. Wind Eng. Ind. Aerodyn.*, **99**, 249–256, doi:10.1016/j.jweia.2011.01.016.

McKeown, K. E., M. M. French, K. S. Tuftedal, D. M. Kingfield, H. B. Bluestein, D. W. Reif, and Z. B. Wienhoff, 2020: Rapid-scan and polarimetric radar observations of the dissipation of a violent tornado on 9 May 2016 near Sulphur, Oklahoma. *Mon. Wea. Rev.*, **148**, 3951–3971, doi:10.1175/MWR-D-20-0033.1.

Moisseev, D. N., and V. Chandrasekar, 2009: Polarimetric spectral filter for adaptive clutter and noise suppression. *J. Atmos. Oceanic Technol.*, **26**, 215–228, doi:10.1175/2008JTECHA1119.1.

NCEI, 2021: U.S. tornado climatology. National Centers for Environmental Information, [Available online at https://www.ncdc.noaa.gov/climate-information/extreme-events/us-tornado-climatology].

NOAA, 2010: Thunderstorms, tornadoes, lightning...Nature's most violent storms: A preparedness guide, including tornado safety information for schools. National Weather Service Doc. NOAA/PA 201051, [Available online at https://www.weather.gov/media/owlie/ttl6-10.pdf], 18 pp.

Nolan, D. S., 2012: Three-dimensional instabilities in tornado-like vortices with secondary circulations. *J. Fluid Mech.*, **711**, 61–100.

Nolan, D. S., 2013: On the use of Doppler radar-derived wind fields to diagnose the secondary circulations of tornadoes. *J. Atmos. Sci.*, **70**, 1160–1171, doi:10.1175/JAS-D-12-0200.1.

NWS, 2019: Weather related fatality and injury statistics. National Weather Service, [Available online at https://www.weather.gov/hazstat/].

Pazmany, A. L., J. B. Mead, H. B. Bluestein, J. C. Snyder, and J. Houser, 2013: A mobile rapid-scanning X-band polarimetric (RaXPol) Doppler radar system. *J. Atmos. Oceanic Technol.*, **30**, 1398–1413, doi:10.1175/JTECH-D-12-00166.1.

Rotunno, R., 1978: A note on the stability of a cylindrical vortex sheet. *J. Fluid Mech.*, **87**, 761–771.

Rotunno, R., 1986: Tornadoes and tornadogenesis. *Mesoscale Meteorology and Forecasting*, P. Ray, Ed., Amer. Meteor. Soc., 414–436.

Rotunno, R., 2013: The fluid dynamics of tornadoes. *Annu. Rev. Fluid Mech.*, **45**, 59–84.

Ryzhkov, A. V., D. W. Burgess, D. S. Zrnić, T. Smith, and S. E. Giangrande, 2002: Polarimetric analysis of a 3 May 1999 tornado. *Preprints, 21th Conf. on Severe Local Storms*, Amer. Meteor. Soc., San Antonio, TX, 515–518.

Ryzhkov, A. V., T. J. Schuur, D. W. Burgess, and D. S. Zrnić, 2005: Polarimetric tornado detection. *J. Appl. Meteor.*, **44**, 557–570, doi:10.1175/JAM2235.1.

Saari, M. D. W., R. M. Lawton, C. J. Schultz, and L. D. Carey, 2014: Early characteristics of the polarimetric tornadic debris signature associated with the 20 May 2013 Newcastle-Moore, Oklahoma, tornado. *J. Operational Meteor.*, **2**, 110–114, doi:10.15191/nwajom.2014.0210.

Salazar, J. L., and Coauthors, 2019: An ultra-fast scan C-band polarimetric atmospheric imaging radar (PAIR). *IEEE Int. Symp. on Phased Array Systems and Technology (PAST)*, Inst. of Electrical and Electronics Engineers, Waltham, MA, https://doi.org/10.1109/PAST43306.2019.9021042.

Satrio, M. A., D. J. Bodine, A. E. Reinhart, T. Maruyama, and F. T. Lombardo, 2020: Understanding how complex terrain impacts tornado dynamics using a suite of high-resolution numerical simulations. *J. Atmos. Sci.*, **77**, 3277–3300, doi:10.1175/JAS-D-19-0321.1.

Schultz, C. J., 2014: Reflectivity vortex hole in a tornadic supercell. *J. Operational Meteor.*, **2**, 103–109, doi:10.15191/nwajom.2014.0209.

Schultz, C. J., and Coauthors, 2012a: Dual-polarization tornadic debris signatures part I: Examples and utility in an operational setting. *Electron. J. Oper. Meteor.*, **13**, 120–137.

Schultz, C. J., and Coauthors, 2012b: Dual-polarization tornadic debris signatures part II: Comparisons and caveats. *Electron. J. Oper. Meteor.*, **13**, 138–150.

Simmons, K. M., and D. Sutter, 2011: *Economic and Societal Impacts of Tornadoes*. American Meteorological Society, 282 pp.

Smagorinsky, J., 1963: General circulation experiments with the primitive equations. I: The basic experiment. *Mon. Wea. Rev.*, **91**, 99–162.

Smith, B. T., R. L. Thompson, D. A. Speheger, A. R. Dean, C. D. Karstens, and A. K. Anderson-Frey, 2020: WSR-88D tornado intensity estimates. Part I: Real-time probabilities of peak tornado wind speeds. *Wea. Forecasting*, **35**, 2479–2492, doi:10.1175/WAF-D-20-0010.1.

Snow, J. T., 1984: On the formation of particle sheaths in columnar vortices. *J. Atmos. Sci.*, **41**, 2477–2491.

Snow, J. T., A. L. Wyatt, A. K. McCarthy, and E. K. Bishop, 1995: Fallout of debris from tornadic thunderstorms: A historical perspective and two examples from VORTEX. *Bull. Amer. Meteor. Soc.*, **76**, 1777–1790.

Snyder, J. C., and H. B. Bluestein, 2014: Some considerations for the use of high-resolution mobile radar data in tornado intensity determination. *Wea. Forecasting*, **29**, 799–827, doi:10.1175/WAF-D-14-00026.1.

Straka, J. M., D. S. Zrnić, and A. V. Ryzhkov, 2000: Bulk hydrometeor classification and quantification using polarimetric radar data: Synthesis of relations. *J. Appl. Meteor.*, **39**, 1341–1372.

Tanamachi, R. L., H. B. Bluestein, W.-C. Lee, M. Bell, and A. L. Pazmany, 2007: Ground-based velocity track display (GBVTD) analysis of W-band Doppler radar data in a tornado near Stockton, Kansas on 15 May 1999. *Mon. Wea. Rev.*, **135**, 783–800.

Toth, M., R. J. Trapp, J. Wurman, and K. A. Kosiba, 2013: Comparison of mobile-radar measurements of tornado intensity with corresponding WSR-88D measurements. *Wea. Forecasting*, **28**, 418–426, doi:10.1175/WAF-D-12-00019.1.

Uchida, T., and Y. Ohya, 2003: Large-eddy simulation of turbulent airflow over complex terrain. *J. Wind Eng. Ind. Aerodyn.*, **91**, 219–229, doi:10.1016/S0167-6105(02)00347-1.

Umeyama, A. Y., 2016: Bootstrap dual polarimetric spectral density estimator. M.S. thesis, School of Electrical and Computer Engineering, University of Oklahoma, 212 pp.

Umeyama, A. Y., B. L. Cheong, S. M. Torres, and D. J. Bodine, 2018: Orientation analysis of simulated tornadic debris. *J. Atmos. Oceanic Technol.*, **35**, 993–1010, doi:10.1175/JTECH-D-17-0140.1.

Umeyama, A. Y., S. M. Torres, and B. L. Cheong, 2017: Bootstrap dual-polarimetric spectral density estimator. *IEEE Trans. Geosci. Remote Sens.*, **55**, 2299–2312, doi:10.1109/TGRS.2016.2641385.

Van Den Broeke, M. S., 2015: Polarimetric tornadic debris signature variability and debris fallout signatures. *J. Appl. Meteor. Climatol.*, **54**, 2389–2405, doi:10.1175/JAMC-D-15-0077.1.

Van Den Broeke, M. S., and S. T. Jauernic, 2014: Spatial and temporal characteristics of polarimetric tornadic debris signatures. *J. Appl. Meteor. Climatol.*, **53**, 2217–2231, doi:10.1175/JAMC-D-14-0094.1.

Vivekanandan, J., S. M. Ellis, R. Oye, D. S. Zrnić, A. V. Ryzhkov, and J. Straka, 1999: Cloud microphysics retrieval using S-band dual-polarization radar measurements. *Bull. Amer. Meteor. Soc.*, **80**, 381–388.

Wakimoto, R. M., N. T. Atkins, and J. M. Wurman, 2011: The LaGrange tornado during VORTEX2. Part I: Photogrammetric analysis of the tornado combined with single-Doppler radar data. *Mon. Wea. Rev.*, **139**, 2233–2258, doi: 10.1175/2010MWR3568.1.

Wakimoto, R. M., P. Stauffer, W.-C. Lee, N. T. Atkins, and J. M. Wurman, 2012: Finescale structure of the LaGrange, Wyoming, tornado during VORTEX2: GBVTD and photogrammetric analyses. *Mon. Wea. Rev.*, **140**, 3397–3418, doi: 10.1175/MWR-D-12-00036.1.

Wakimoto, R. M., Z. Wienhoff, H. B. Bluestein, D. J. Bodine, and J. M. Kurdzo, 2020: Mobile radar observations of the evolving debris field compared with a damage survey of the Shawnee, Oklahoma, tornado of 19 May 2013. *Mon. Wea. Rev.*, **148**, 1779–1803, doi:10.1175/MWR-D-19-0215.1.

Wienhoff, Z. B., H. B. Bluestein, D. W. Reif, R. M. Wakimoto, L. J. Wicker, and J. M. Kurdzo, 2020: Analysis of debris signature characteristics and evolution in the 24 May 2016 Dodge City, Kansas, tornadoes. *Mon. Wea. Rev.*, **148**, 5063–5086, doi:10.1175/MWR-D-20-0162.1.

WSEC, 2006: A recommendation for an enhanced Fujita scale (EF-scale). Tech. rep., Texas Tech University Wind Science and Engineering Center, 95 pp. [Available online at https://www.depts.ttu.edu/nwi/Pubs/EnhancedFujitaScale/EFScale.pdf].

Wurman, J. M., and C. R. Alexander, 2005: The 30 May 1998 Spencer, South Dakota, storm. Part II: Comparison of observed damage and radar-derived winds in the tornadoes. *Mon. Wea. Rev.*, **133**, 97–119, doi:10.1175/MWR-2856.1.

Wurman, J. M., and S. Gill, 2000: Finescale radar observations of the Dimmitt, Texas (2 June 1995), tornado. *Mon. Wea. Rev.*, **128**, 2135–2164.

Wurman, J. M., J. M. Straka, and E. N. Rasmussen, 1996: Fine-scale Doppler radar observations of tornadoes. *Science*, **272**, 1774–1777, doi:10.1126/science.272.5269.1774.

Yu, T.-Y., X. Xiao, and Y. Wang, 2012: Statistical quality of spectral polarimetric variables for weather radar. *J. Atmos. Oceanic Technol.*, **29**, 1221–1235, doi:10.1175/JTECH-D-11-00090.1.

Zhang, G., 2019: *Weather Radar Polarimetry*. 1st ed., CRC Press, 304 pp.

Zrnić, D. S., 1975: Simulation of weatherlike Doppler spectra and signals. *J. Appl. Meteor. Climatol.*, **14**, 619–620.

Zrnić, D. S., D. W. Burgess, and L. Hennington, 1985: Doppler spectra and estimated windspeed of a violent tornado. *J. Appl. Meteor. Climatol.*, **22**, 1068–1081.

Zrnić, D. S., R. J. Doviak, and D. W. Burgess, 1977: Probing tornadoes with a pulse-Doppler radar. *Quart. J. Roy. Meteor. Soc.*, **103**, 707–720.

Zrnić, D. S., and M. Istok, 1980: Wind speeds in two tornadic storms and a tornado, deduced from Doppler spectra. *J. Appl. Meteor. Climatol.*, **19**, 1405–1415.